Politecnico di Torino

Master of Science in Mechanical Engineering

Master's Degree Thesis

Improving floating wind turbine platform performance through mooring line actuation

Supervisor | **Candidate**

Stefano Marchesiello | Lorenzo Cavallo

Michael Kenneth McWilliam

A.A. 2024/2025

Abstract

In the context of the global energy transition, offshore wind energy is a key technology for large-scale decarbonisation. Floating platforms, in particular, allow the exploitation of wind potential in deep waters, where fixed foundation solutions are impractical. This exploratory and preliminary thesis aims to evaluate the effectiveness of an active control system applied to the mooring lines of a semi-submersible platform operating at a depth of 600 metres.

Using a simplified two-degree-of-freedom dynamic model developed in `MATLAB`, the effect of different state-feedback control strategies on the stability and dynamic response of the platform under realistic environmental conditions is analysed. The results indicate that active control can significantly reduce acceleration at the top of the tower, pitching during extreme gusts and fatigue damage to the mooring cables. However, the energy required for implementation remains a significant limitation. A selective control activation strategy, limited to the most critical environmental scenarios, has enabled a reduction in consumption of more than 65% while maintaining acceptable performance. Although this is a highly simplified study, it highlights the potential of active control in the design of floating platforms and lays the foundations for future developments on more complete and realistic models.

Table of Contents

List of Figures

List of Tables

Chapter 1

The Global Energy Market

1.1 The Ecological Transition and Renewables in the Global Energy Mix

The global climate crisis and the increasing and unsustainable use of fossil fuels have accelerated in the last decade the transition to a low-emission energy system. The main international institutions, such as the International Energy Agency (IEA) and the European Union, have identified in the decarbonization of the energy production sector one of the main challenges to achieve the ambitious target of climate neutrality by 2050, but still in 2024, more than 56 % of the world's energy production was made by non-renewable sources. In emerging markets and developing economies, energy-related CO2 emissions increased by 1.5% (375 Mt CO2) in 2024, driven by increasing energy demand associated with rapid economic and population growth. At the same time, in advanced economies, energy-related CO2 emissions decreased by 1.1% (120 Mt CO2) in 2024, driven by a 5.7% decline in coal emissions and a 0.5% drop in oil emissions. Natural gas emissions increased by 0.9%. This reduction reflects the continued deployment of advanced economies in low-emissions energy sources, with renewables and nuclear power accounting for over 50% of electricity generation, led by strong growth in wind and solar.

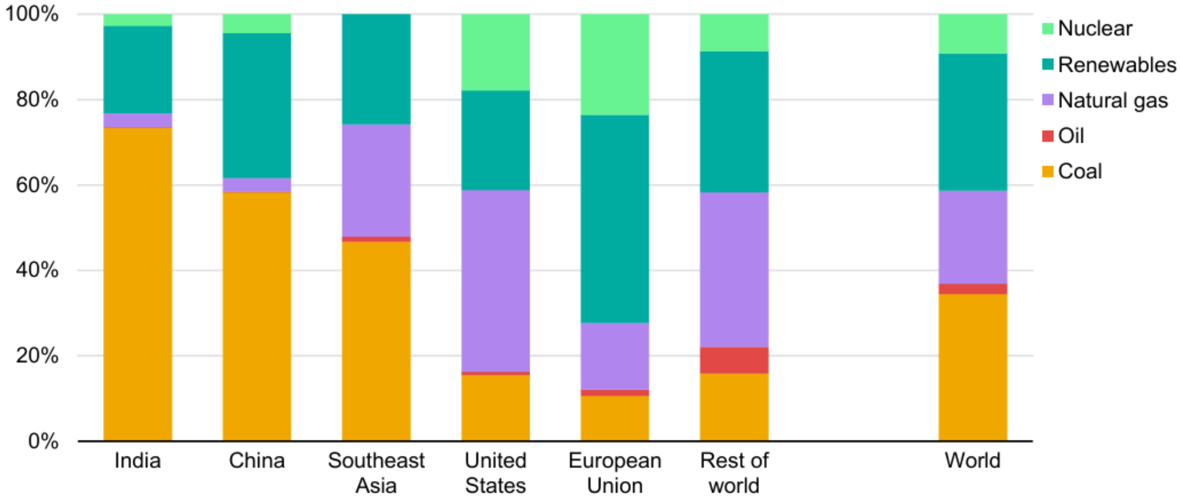

Figure 1.1: Electricity generation mix for selected regions in 2024.[1]

The main-case renewable electricity forecast is not on track to reach the IEA Net Zero Emissions by 2050 Scenario goals, which indicate that the share of renewables in global electricity generation should double, to achieve almost 60% by 2030. Thus, the main case forecast falls 14 percentage points (5 000 TWh) below Net Zero by 2050 Scenario modelling. [21]. [4].

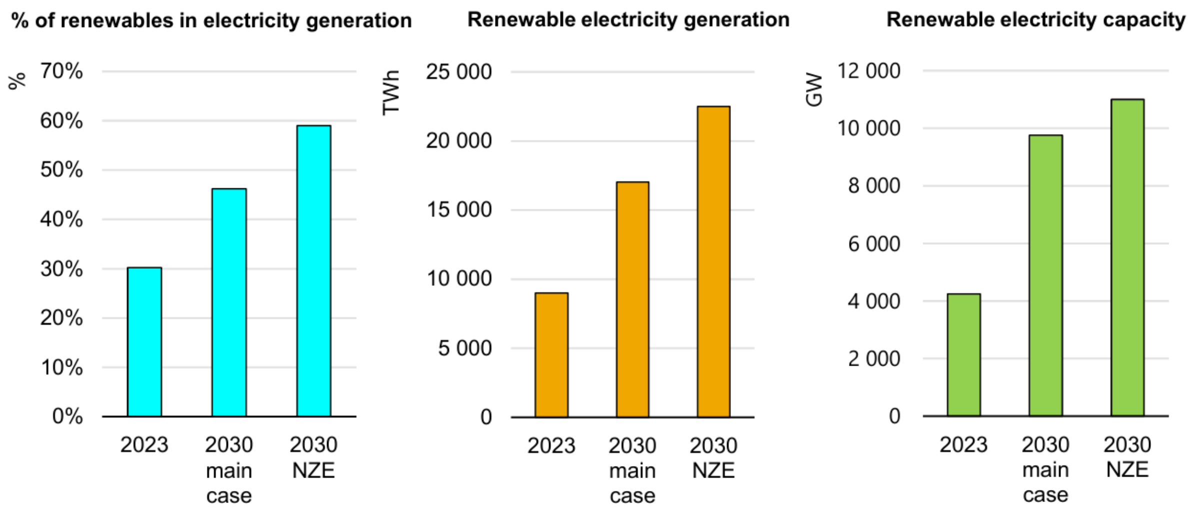

Figure 1.2: Global renewable electricity generation capacity and share in total generation: 2023 and 2030.[2]

One of the most important data is that in the main scenario of the green energy transition, 90% of the new renewables energy production from 2023-2028 will be made with variable renewable energy, mostly wind and solar energy. This dynamic, on one

[1]Source: [21]
[2]Source: [4]

hand,encourages the acceleration of the phase-out of coal and gas;on the other hand,it poses major challenges in terms of managing grid variability and stabilization.[4]

The growth of renewables is highly unbalanced globally. In Europe, installed capacity grows according to long-term strategic plans, supported by incentives and public auction mechanisms. In Asia (China above all), the growth is driven by centralized industrial planning. In the United States, on the other hand, market forces and regionalization prevail. However, in all macro-regions, there is an acceleration of investment in offshore wind power, considered a key technology for ensuring large-scale, high-capacity production near coastal load centres.[4] Offshore turbines access more stable and intense wind regimes than land-based installations, with capacity factors above 50%. The absence of orographic obstacles and less atmospheric turbulence allows for smoother and more predictable operation, while also reducing visual impact and land-use conflict.[11]

In light of the current framework, it is imperative to pursue, or at least to come close, to the decarbonization targets set for 2050 under the Net Zero initiative, to promote the adoption and development of innovative technologies in the Offshore wind energy sector. This technology, although still at a relatively embryonic stage compared to onshore wind, has considerable growth potential, especially in areas with high wind resource availability, and there is also the potential to extend this new technology in areas with deep waters.

In this scenario,the present work thesis is set, which aims to contribute to improving the dynamic performances of floating wind platform, through the implementation of an active control system applied to mooring cables. This thesis aims to demonstrate through a modelling and numerical approach how advanced control strategies can be a key element in order to improve the stability and the safety of structures, while reducing structural loads and associated energy consumption. Even though it is a limited contribution in a much bigger energy transition context, this approach wants to offer a concrete engineering perspective, on the possibility of optimising the technical solutions currently available, with the ambition of participating, even partially, in achieving the ambitious climate targets set at international level.

1.2 Offshore Wind in Europe: Growth, Challenges, and 2030 Targets

Wind capacity in Europe reached in 2024 285GW.

- 248 GW from Onshore installation
- 37 GW from Offshore installation.

Only in 2024, 16.4 GW of new wind capacity has been installed, from this

- 13.8 GW from Onshore (84%)
- 2.6 GW from Offshore (16%)

The offshore turbines installed in 2024 have an average unit power of 10.1 MW, a constant increase compared to previous years (7.4 MW in 2022), and are characterized by

- Rotor diameters greater than 220 m.
- Hub height >130 m.
- Single-pile foundation system for depths < 50 m and floating for depths>60-70 m.

Leading the offshore expansion in 2024 were:

- United Kingdom (historical leader), with more than 1 GW installed.
- Germany, which resumed installations after a slowdown between 2018 and 2021.
- France, with the connection to the grid of some of its first industrial-scale offshore parks.[11]

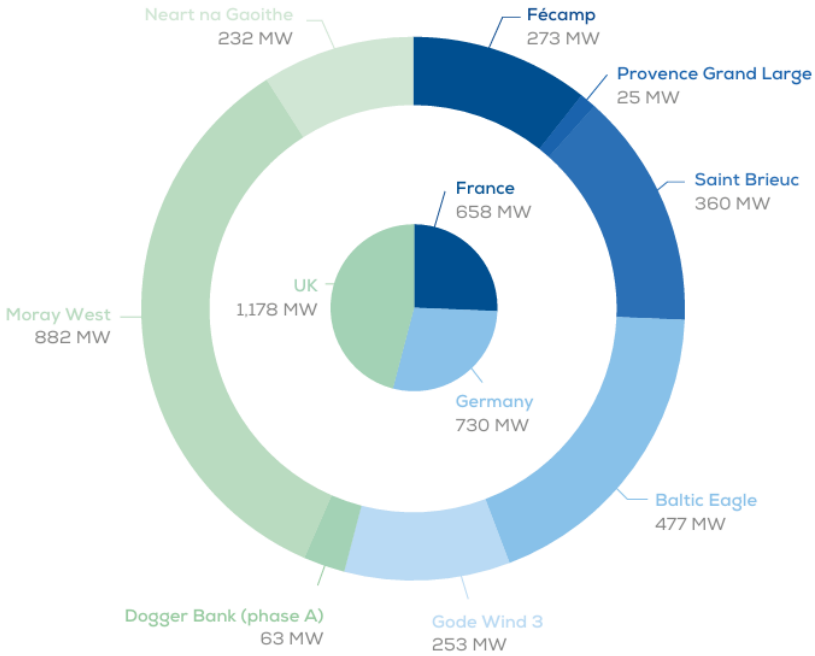

Figure 1.3: New offshore wind capacity connected in Europe in 2024.[3]

Offshore installations nowadays remain highly concentrated in some countries, while in others - such as Spain, Italy and Greece - installations are still marginal or at the planning stage. However, the technical offshore wind potential in the Mediterranean, according to Rystad Energy, exceeds 400 GW, making this region strategic for future expansion, particularly through the use of floating platforms. [3] Europe maintains very high ambitions for the development of offshore wind power. The continent has a unique combination of abundant wind resources and relatively shallow seas, particularly in the North and Baltic Seas, making it particularly suitable for the expansion of this technology. Historically, Europe has led innovation in the offshore sector, thanks to an established supply chain and long experience in the design, installation and operation of marine wind farms [11]. In 2021, European governments had set a collective target of 114 GW of installed offshore capacity by 2030. This target was later increased to 158 GW in September 2022. However, in subsequent years, several national governments have scaled back these targets, due to difficulties in building a favourable regulatory framework, the expansion of the electricity grid, and the capacity of local supply chains. As a result, the full realisation of

[3]Source: [11]

the capacity targets by 2030 appears difficult to achieve today. Despite these difficulties, the development of the offshore market has not come to a halt. New projects will continue to be connected beyond 2030, with an acceleration expected in the first half of the next decade. However, there are several bottlenecks risks that can jeopartise the desired rapid expansion:

- Delays in offshore auctions due to the absence of clear rules or comprehensive regulatory frameworks;
- Insufficient port capacity, which could become a bottleneck as early as 2029.
- Excessively long port infrastructure development times (6-10 years on average).
- Delays in grid connection, due to delays in onshore and offshore expansion plans and inadequate authorisation mechanisms (e.g,first-come-first-served instead of dynamic approaches based on project maturity.

Despite all that, the WindEurope report predicts that in the period 2025-2030 Europe will install a total of 187 GW of new wind capacity, of which:

- 48 GW offshore (about 11 GW/year);
- 139 GW onshore (about 20 GW/year).

This pace, if maintained, would bring total wind power capacity to 351 GW by 2030. However, the EU has set a more ambitious target in the REPowerEU package: 425 GW in total, of which 111 GW offshore. This means the urgency of accelerating the annual growth by 20-25% , especially in the area of offshore installation. [11]

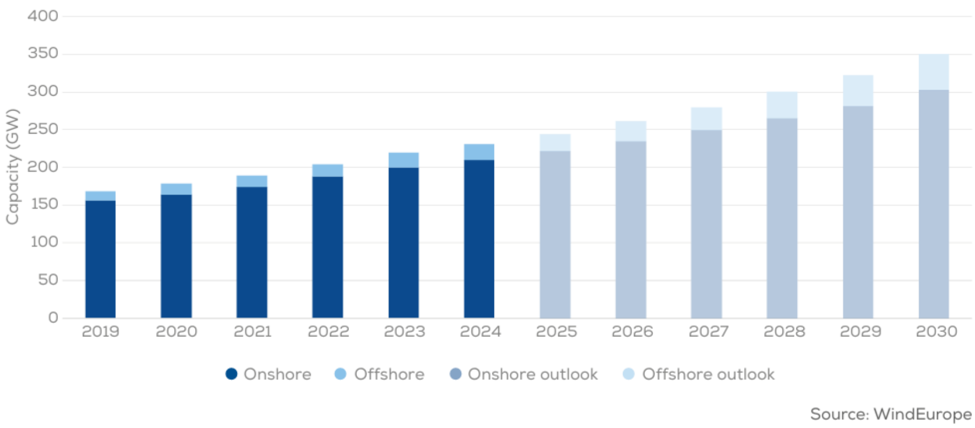

Figure 1.4: Wind Capacity Outlook 2019-2030 [4]

[4]Source: [11]

Chapter 2

Literature Review and Theoretical Framework

2.1 Technologies for Supporting Offshore Wind: From Foundations to Floating Platforms

The development of offshore wind is made possible by the evolution of turbine support technologies, which can be classified into two main macro-categories according to the type of foundation: fixed and floating. The choice of one or the other solution depends mainly on the depth of the seabed, the weather and sea conditions and the distance from the coast. [20, 15]

2.1.1 Fixed foundations

Fixed foundations are currently the most widely used solution in Europe, especially in the North Sea and the Baltic, where sea depths are very frequently less than 50 metres. The main types are:

Monopile

consisting of a large steel pole driven vertically into the seabed. The simplest and most Common foundation for seabeds of more than 40 m. Its beauty lies in its ease of installation and lower cost, making it a popular choice. However, this simplicity comes at a price. Monopiles aren't suitable for deeper waters or areas with rocky seabeds, limiting their applicability. For instance, the Hornsea One wind farm, located in the United Kingdom, in the North Sea, approximately 120 km off Yorkshire, utilizes this technology effectively due to the favorable seabed conditions. [5, 47, 6]

Jacket

For more challenging environments, jacket structures become relevant. These steel lattice structures are anchored to the seabed at multiple points using piles or suction buckets. They offer greater stability and can handle harsher marine conditions than monopiles, extending their use to depths of 30 to 60 meters. However, this robustness comes with increased costs and installation complexity. The Beatrice Offshore Wind Farm, located in Scotland, in the North Sea, as Hornsea, but approximately 13 km off Caithness, provides a good example of a project where the enhanced stability of jacket foundations was deemed necessary. [5, 35]

Gravity based

These are massive concrete structures that rely on their sheer weight to stay put on the seabed. While they eliminate the need for pile driving, their transport and installation are incredibly complex, requiring a flat and strong seabed. They're a niche solution, used only in specific circumstances where other foundation types are impractical. One example is the Thornton Bank Offshore Wind Farm, located in Belgium, in the North Sea, approximately 28km off the coast, where the unique seabed conditions helped this approach. [5, 35]

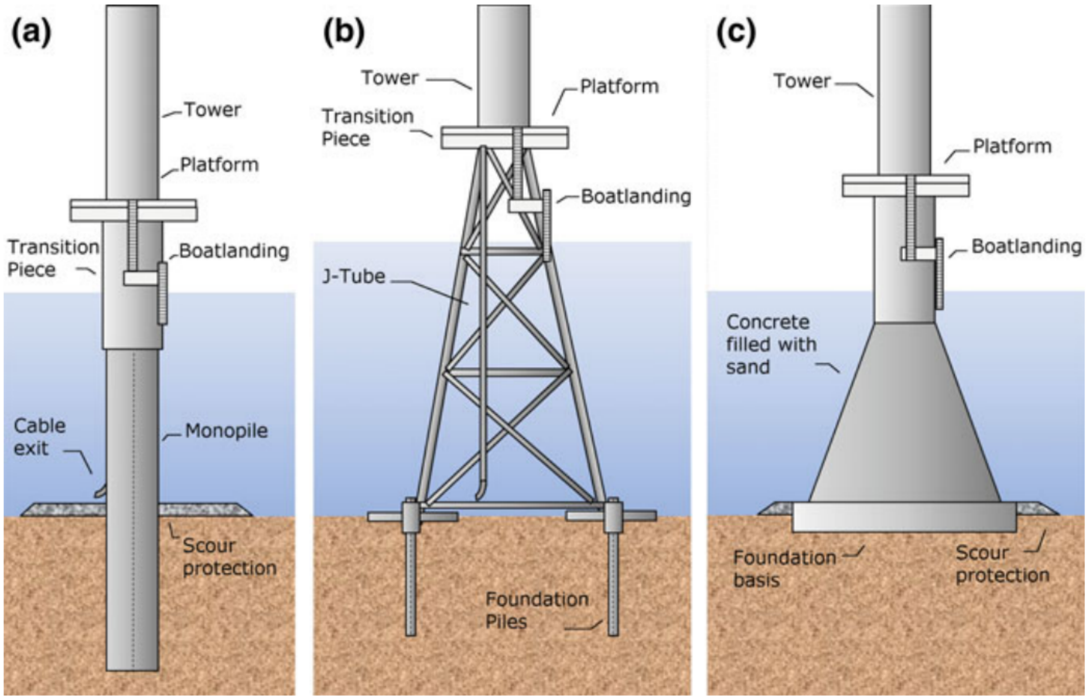

Figure 2.1: Three types of fixed foundations: Monopile (a), jacket (b) and gravity based (c)[1]

2.1.2 Floating platform

The lack of space on land and the necessity for a more reliable and constant source of energy have made it necessary to extend offshore installations on sites characterized by a sea depth of more than 60 meters, where the use of fixed foundation, as already explained before, is no longer economically viable and technically feasible. In this context, floating offshore wind platforms (FOWPs) are nowadays the only known solution to harnessing the potential of offshore wind energy in deep water. It's a relatively new frontier, full of exciting possibilities and ongoing innovation. The ever-increasing size of wind turbines, now regularly exceeding 10 MW, coupled with the demanding marine conditions in these deeper locations, necessitates platforms that are incredibly stable, robust, and durable. Currently, three main types of floating platforms are competing for dominance, each with its unique approach to stability: Spar-Buoy, Semi-Submersible, and Tension Leg Platform (TLP). Choosing the right platform is a delicate balancing act, taking into account factors such as water depth, weather conditions, mooring technologies, and the logistical challenges of installation.

[1]Source: [13]

Spar Buoy

Spar Buoy platform is based on the principle of gravitational stabilisation, achieved using a long vertical cylindrical body ballasted in its lower part. The operating principle is based on moving the centre of mass below the centre of buoyancy, generating a righting moment that ensures stability in roll and pitch. The submerged volume provides hydrostatic lift, while the high inertia gives good resistance to dynamic loads. From a dynamic point of view, the Spar presents its low frequencies, well outside the typical excitation range of ocean waves (0.05-0.3 Hz), enhancing long-term response. It is particularly suitable for depths greater than 100-150 m. From a dynamic point of view, Spar Buoy platforms are very stable in rotation, with very low proper frequencies for roll and pitch. However, they are particularly vulnerable to horizontal shifts (surge and sway) while vertical displacements are usually small. This type of platform is used in pioneering projects such as "Hywind Scotland" and "Hywind Tampen", developed by Equinor. [20]

The main advantage of Spar Buoys is their structural simplicity and high hydrostatic stability. However, major disadvantages are related to the high draft, which makes transportation and complete assembly in port difficult: the turbine often has to be installed offshore, increasing costs and operational risks.[20]

Tension Leg Platform (TLP)

The TLPs employ a constrained stabilization system, using vertical pre-tensioned cables (tension legs) anchored to the bottom. These structural elements generate very high stiffness along the vertical direction and drastically limit heave, pitch and roll motions. The dynamic response is similar to that of fixed structures, with extremely low amplitudes of motion even under significant environmental loads. Nevertheless, the installation requirements are stringent: TLPs need foundations capable of withstanding high axial loads (e.g. reinforced suction piles), as well as an accurate tensioning system. Currently, they have only been used in experimental contexts or feasibility studies. "Simulations in the reports Stabilisation of the Wind Turbine Floating Platform using Mooring Actuation" and "Fuzzy Airflow-Based Active Structural Control" demonstrate the validity of the principle and the high potential in combination with active control systems. [19, 31, 49]

Barge

Barge-type platforms constitute a floating structural solution characterized by a flat, shallow-draft geometry, usually derived from converted naval barges or wide-base rectangular pontoons. Barge stability is essentially ensured by the large waterline area and symmetric distribution of hydrostatic buoyancy. Compared with spar or semi-sub configurations, barges have higher roll and pitch eigenfrequencies, which make them more sensitive to wave excitation in the 0.05–0.3 Hz range typical of oceanic seas. This exposes them to amplified dynamic motions, especially in formed sea conditions, limiting their applicability to sites characterized by low wave intensity or near-shore pilot projects.

From a construction and logistics perspective, however, the barge is very competitive: the platform can be fully assembled in port, reducing installation time and costs. In addition, the simple geometry and high accessibility facilitate the integration of active control systems, inertial sinks, or hydraulic actuation devices.

In the literature, this type of configuration is treated critically in comparison with semi-submersible, spar and TLP, and often used as a reference for simplified numerical studies due to its direct geometric modelability and symmetric distribution of submerged masses and volumes. [23, 24]

Semi-Submersible

Semi-submersibles represent the most versatile structural solution today. They consist of three or more floating columns interconnected by horizontal pontoons, which evenly distribute the displacement volume and provide a large, stable base. The Stability it derives from the large waterplane area-based stabilisation and hydrostatic symmetry. The shallow draught (10-20 m) allows assembly to be completed in port and towed on site in operational trim. [19, 31]

Semi-submersibles exhibit a more complex dynamic response than spar: they are more susceptible to roll and pitch, but offer greater modularity, adaptability and logistical simplicity. The width of the platform allows the installation of active control systems, inertial dampers, or hydraulic actuation devices. Major projects include WindFloat Atlantic (Portugal), Kincardine (UK) and Damping Pool (France). [5, 10, 8]

In the model developed within this thesis work, a floating platform of the semi-submersible type was adopted, inspired by the one designed by the University of Maine

(UMaine), which has already been extensively documented in the technical literature and in the IEA Wind reports. The choice of this type of structure is not causal, but responds to precise reasons of a technical and perspective nature. [5]

In particular, it is believed that the semi-submersible configuration represents, to date, the most versatile and scalable structural solution in the panorama of floating offshore wind technologies. It combines good hydrostatic stability with a layout that is compatible with great depths, providing an effective balance between buoyancy requirements, damping capacity and construction simplicity. These characteristics make it particularly suitable for future large-scale industrial developments. [5]

In the specific case of the model implemented here, the operational depth is assumed to be 600 metres, a value that excludes a priori the use of fixed foundations and imposes the adoption of floating technologies optimised for deep waters. In this context, the semi-submersible platform is configured as the most suitable solution from both a structural and dynamic point of view, guaranteeing a solid base for the implementation and validation of the active control system on the mooring cables.

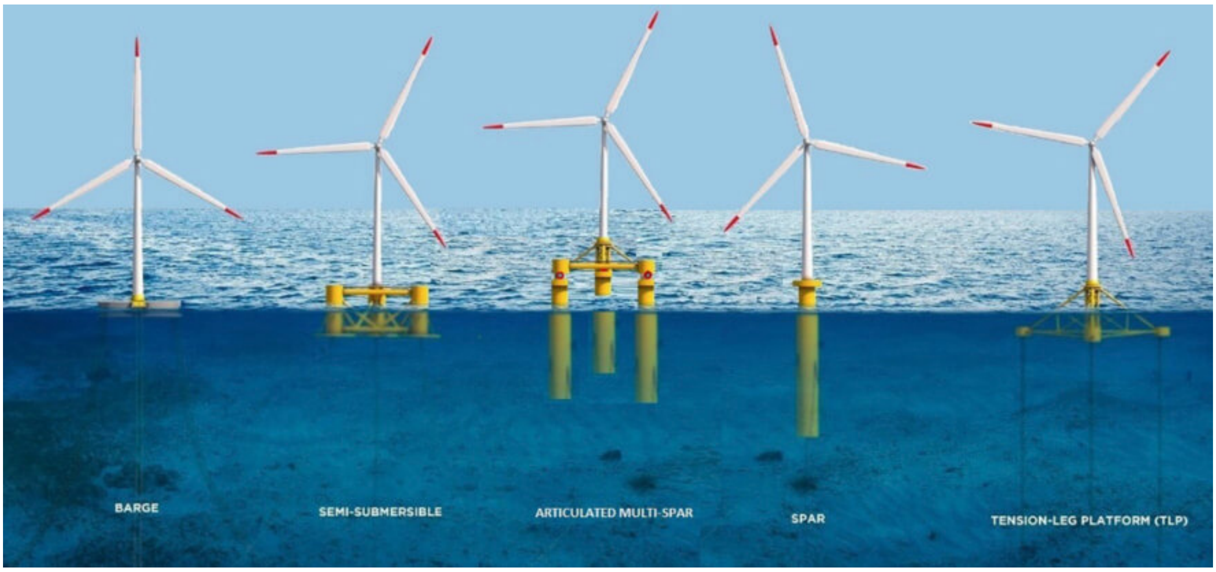

Figure 2.2: Different types of floating platform [2]

[2]Source: [18]

2.2 Dynamic Design Challenges and Literature Insights

Despite the promising prospects offered by floating offshore wind technology, deepwater platform engineering presents a wide range of design, operational, and economic challenges that require a multidisciplinary approach and a high degree of technological innovation.

2.2.1 Hydro-Aero-Structural Interactions

The first and most significant critical issue arises from the complex interaction between environmental forces (wind, waves, sea current) and the structural response of the platform, which requires the adoption of highly nonlinear and computationally expensive coupled aero-hydro-structural models. The oscillations induced by these loads significantly affect the stability, dynamic response, and overall efficiency of the system, necessitating careful design from the early stages.[46]

An additional challenge is posed by the hydrodynamic behaviour of the various types of floating platforms. For example, while semi-submersibles offer advantages in terms of stability and ease of installation, they are more exposed to wave-induced motions than TLPs or spars, and structurally more complex. Each platform type presents trade-offs among stability requirements, ease of deployment, operational costs, and site-specific adaptability [33, 19, 46].

2.2.2 Mooring System and Fatigue Issues

A particularly critical aspect is the design of the mooring system, which plays a fundamental role in station keeping. Voltage variations induced by surge and heave motions can result in fatigue cycles that reduce system durability, especially in configurations transitioning between taut and slack regimes. Optimization of layout and stiffness is thus essential not only for static equilibrium, but also for improving the dynamic response and limiting design loads. [40, 47, 30]

2.2.3 Aerodynamic Sensitivity and Wake Effects

From the aerodynamic perspective, the motion of the floating platform has a direct effect on rotor behaviour. In particular, pitch and roll induce cyclic variations in the apparent angle of attack on the blades, which can trigger dynamic stall and impulsive lift variations, thereby reducing efficiency and increasing unsteady loads. The interaction between aerodynamic wake and platform motion in multi-turbine arrangements or wind farm layouts represents an additional complexity. Wake effects are magnified by motion-induced turbulence and can cause significant losses in capacity factor and power variability. Notably, the geometrical layout of the turbines strongly influences performance: staggered configurations help mitigate wake losses better than tandem arrangements. [26]

2.2.4 Operational Constraints and Access Limitations

These technical challenges are further complicated by operational and maintenance issues. Floating wind platforms are subject to strict limitations in terms of accelerations and angular motion, which constrain access for inspections, crew transfers, and maintenance interventions. Roll angles and tower-top accelerations must be kept within well-defined thresholds to ensure operational safety and turbine longevity. [19].

2.2.5 Opportunities and Role of Active Control

Nevertheless, these challenges are counterbalanced by considerable opportunities. Floating wind turbines enable deployment in deeper waters, where wind regimes are more stable and intense, with higher potential capacity factors than near-shore installations. Furthermore, the possibility of onshore assembly and towing to site reduces the reliance on specialized offshore vessels, cutting both installation time and cost. [46, 31]

Finally, the development of active control strategies, whether through blade pitch control or actuation of the mooring cables, opens new prospects for mitigating dynamic loads and enhancing overall system performance. If integrated from the preliminary design phase, such strategies can enable a shift from passive to adaptive behaviour in floating platforms, improving resilience against extreme conditions and potentially extending operational limits to harsher offshore environments [49, 31].

2.3 Theoretical Frameworks

The design and control of floating wind platforms in deep water require accurate modeling of both the environmental stresses and the dynamic behavior of the platform-cable-turbine system. This section presents the main theoretical tools used to construct the simplified two-degree-of-freedom model developed as part of this work. After an introduction to stochastic wind and wave models, the equations of motion associated with the physical system are analyzed, with particular reference to the dominant heave and pitch modes. Finally, the fundamental concepts of control theory applied to the active regulation of mooring lines are introduced, highlighting the engineering rationale behind the choice of open- and closed-loop strategies. For further details, please refer to Appendix A

2.3.1 Enviromental Models

For a simplified model of active control on mooring cables to be reliable and representative of the operational reality of a floating wind platform in deep water, it is essential to test it in a realistic environmental context, i.e., subject to the main aerodynamic and hydrodynamic stresses to which the platform would be exposed under operating conditions. With this in mind, it is therefore essential to define a coherent and structured procedure to represent the "real environment" in which the platform operates. Such a procedure, involves three main phases: (1) the discretization of the operational environment into a finite set of meteorological conditions (bins) and the estimation of the probability of occurrence for each significant combination of wave height and wind speed; (2) the generation of representative time series for these conditions; (3) the conversion of the time series into time histories of forces acting on the platform, to be used as input for the dynamic simulations. This logic chain forms the basis for estimating average loads and expected dynamic stresses, as well as for evaluating the performance of the active control system under realistic environmental scenarios.

Environmental Binning and Load Estimation

It is therefore essential to define a systematic method to estimate the environmental loads acting on the platform. In particular, in the case study considered, we will proceed with a simplification of the problem, assuming that the dominant environmental forces can be attributed to the wind thrust force and the buoyancy variation induced by the significant wave height.

However, offshore environmental conditions are characterised by high variability: the platform will be exposed to a wide range of combinations of wind strength and wave height. Although the marginal distributions of these two parameters (which can be modelled with Weibull distributions for wind and Rayleigh distributions for waves, respectively) are often known, their joint correlation is generally unknown.

In order to simplify the analysis and make the problem computationally manageable, it is assumed that wind and wave are statistically independent of each other, while recognising that in reality this assumption is an approximation, because it is possible for the two phenomena to influence each other.

We therefore subdivide the domain of environmental conditions into a set of two-dimensional bins (hs, ws), determining for each bin a representative load calculated at the centre of the bin. The probability of occurrence of each bin is estimated as the product of the marginal probabilities, and the resulting loads are then weighted according to these probabilities to estimate the expected value of the average load acting on the platform.

This discretised approach makes it possible to statistically estimate the average behaviour of the system without having to perform numerical simulations for every possible environmental condition, and is an essential prerequisite for structural fatigue or energy yield assessments.

To implement the method just described, it is first necessary to construct Cumulative Distribution Functions (CDF) for each of the two environmental variables considered: wind speed and significant wave height. The CDF represents, for a given continuous random variable, the probability that this variable will assume a value less than or equal to a certain fixed value. In other words, the CDF provides a cumulative measure of the probability distribution and is fundamental to the calculation of the probabilities associated with the bins along each dimension of the environmental domain.

In our case, wind speed is modelled using a Weibull distribution, a distribution widely adopted in wind engineering due to its ability to accurately represent the empirical distribution of anemometric data at different offshore sites. The Weibull distribution is characterised by two parameters: the shape parameter $k = 2$, which controls the dispersion, and the scale parameter $\lambda = 6$, which determines the mean intensity. [9, 12]

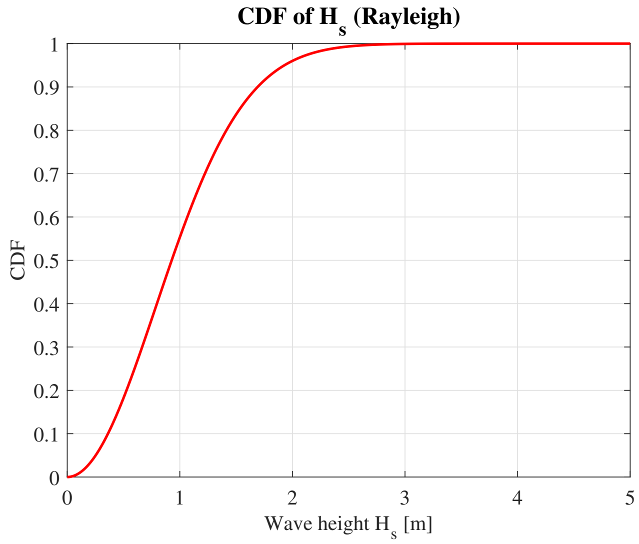

(a) CDF distribution for wave height

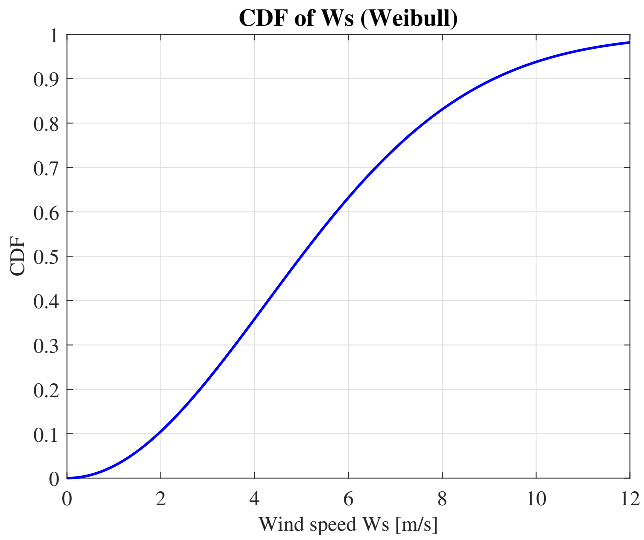

(b) CDF distribution for wind speed

Figure 2.3: CDF distributions for wind speed and wave height

The probability density function (PDF) of the Weibull distribution is:

$$f_W(w) = \frac{k}{\lambda}\left(\frac{w_s}{\lambda}\right)^{k-1} \exp\left[-\left(\frac{w_s}{\lambda}\right)^k\right] \tag{2.1}$$

And the corresponding cumulative distribution function (CDF) is:

$$F_W(w_s) = 1 - \exp\left[-\left(\frac{w_s}{\lambda}\right)^k\right] \tag{2.2}$$

As for the significant wave height, this is modelled using a single-parameter Rayleigh distribution, using a scaling value of $\sigma = 0.788$. The cumulative Rayleigh distribution function is given by:

$$F_H(h) = 1 - \exp\left(-\frac{h_s^2}{2\sigma^2}\right) \tag{2.3}$$

Once the CDFs of both distributions are known, it is possible to subdivide each variable into discrete intervals (bins), defined by fixed thresholds, and calculate the probability associated with each bin as the difference between the CDF values at the bin boundaries. [9, 12]

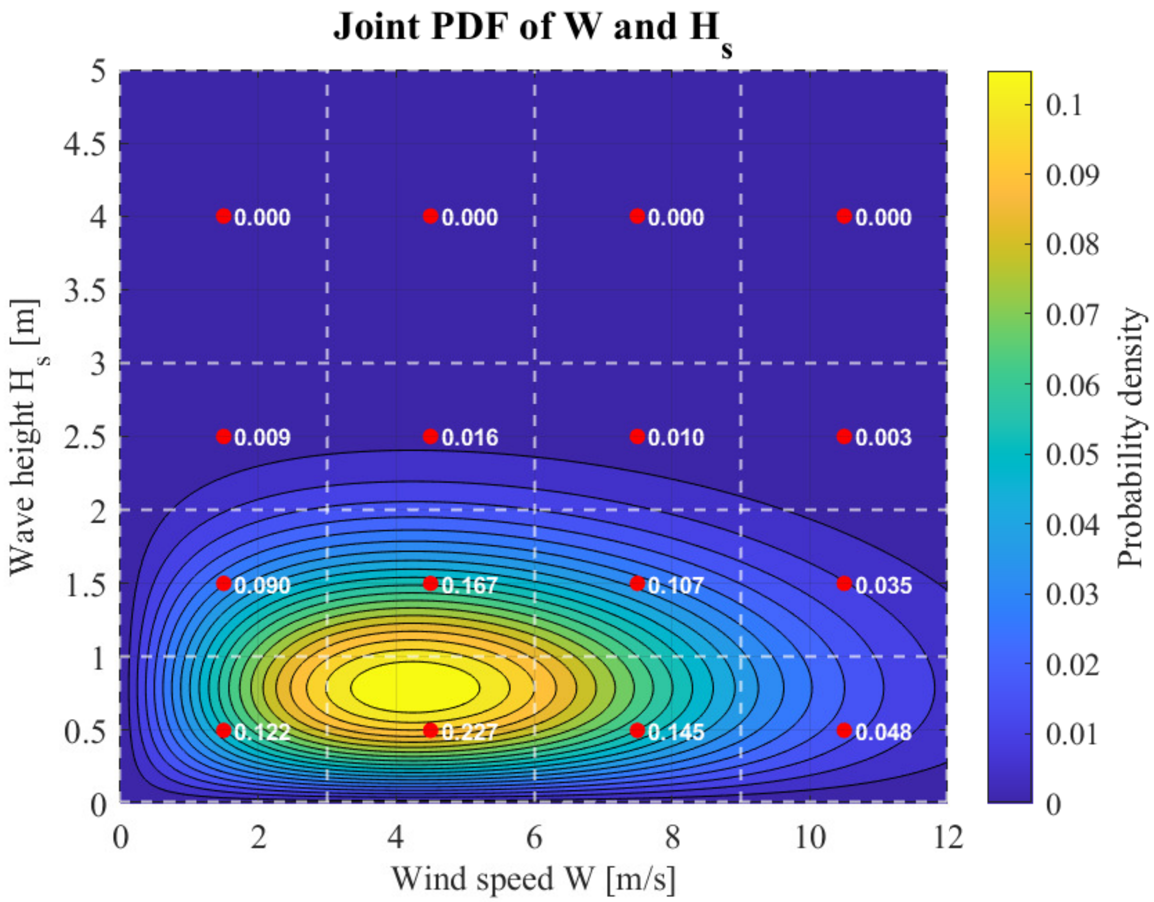

Figure 2.4: Joint PDF distribution

Generation of Environmental Time Series

In order to realistically simulate the operational environment of the floating wind platform, a simplified but consistent approach with the technical literature was adopted, aimed at the generation of representative time series of the acting environmental forces. These time series constitute the fundamental input for the dynamic analysis of the system in the time domain and are obtained through the inverse Fourier transformation of the spectral representation of the phenomena. In particular, the Kaimal spectrum was used for the generation of the turbulent wind and the JONSWAP spectrum for the generation of the significant wave height, assuming fully developed sea conditions. The procedure involves the definition of a discrete time interval with a constant step $\Delta t = 0.01$ s and a total duration of 60 seconds, with an associated spectral resolution of $\Delta f = 1/T_p$. The frequency vector is constructed from Δf up to a maximum limit of 0.5 Hz, consistent with the physically relevant limits for the time scales of platform motion.

For each pair of representative environmental conditions (i.e., a bin of significant height h_s and average wind speed w_s), two sets of independent random phases are constructed, made deterministic by assigning a separate initialisation seed for wind and wave, to ensure statistical independence between the two simulated signals. For wind, the turbulent component is assumed to follow a Kaimal spectrum, which is widely used in the wind context to represent the spectral distribution of turbulent energy at low altitude. The spectral function is defined as a function of the turbulence intensity I, the longitudinal scale length l, and the average wind speed, and is converted into spectral amplitudes via the square root of the spectral density multiplied by the interval Δf. The sum of harmonic sinusoids with defined amplitudes and phases finally allows the reconstruction in the time domain of the instantaneous wind speed.

For wave motion, the JONSWAP spectrum with peak parameter $\gamma = 1.0$, and peak period $T_p = 11$ s was used, assuming uni-directional waves. Spectral amplitudes are obtained analogously to the wind, and the resulting time series represents the free elevation of the sea surface as a function of time. In order to ensure that the generated series correctly reproduces the desired significant height, an iterative recalculation of the spectrum is performed until the condition $H_s = 4\sqrt{\int S(f)\,df}$ is met, with numerical tolerance set. While this approach is effective for the synthetic generation of realistic signals, it has some inherent limitations. First of all, the representation of wind using the Kaimal spectrum assumes stationary and homogeneous conditions of the turbulent flow, ignoring any transients or complex vertical gradients. Similarly, the JONSWAP spectrum adopted does not take into account directional components nor limited fetch or tidal effects. Furthermore, both time series are generated over relatively short time windows and do not resolve components at frequencies below Δf resolution. These assumptions must therefore be taken into account in the subsequent interpretation of the dynamic results.

Conversion of Time Series into External Loads

The process of converting the time series of wind and wave height into forces and moments applied on the floating platform is an essential step in the simulation of the operational environment. However, in order to keep the model computationally manageable and consistent with the level of abstraction adopted, several simplifications have been introduced that limit its physical fidelity, while retaining a good predictive value for comparison and control purposes.

First of all, the force exerted by the wind, denoted by $F_{\text{wind}}(t)$, is calculated using a simple drag force, assuming that all the wind hits only the rotor, not considering the force distribution along the entire turbine tower:

$$F_{\text{wind}}(t) = \frac{1}{2}\,\rho_{\text{air}}\,C_T\,A_{\text{rot}}\,[v_{\text{ts}}(t)]^2 \tag{2.4}$$

Where:

- ρ_{air} is the air density,
- C_T is the aerodynamic thrust coefficient of the rotor.
- A_{rot} is the frontal area of the rotor,
- $v_{\text{ts}}(t)$ is the wind speed value at time t extracted from the time series.

The aerodynamic torque $M_{\text{wind}}(t)$ is calculated by multiplying the force by the vertical arm represented by the height of the rotor relative to the point of rotation:

$$M_{\text{wind}}(t) = F_{\text{wind}}(t) \cdot h_t \tag{2.5}$$

This modelling neglects tip-speed ratio dependence, transient effects, pitch dynamics and blade-flow interaction, and is justifiable in the functional verification phase of the control.

About wave interaction, the instantaneous vertical buoyancy force $F_{\text{wave}}(t)$ is modelled as a linear function of sea surface height, calculated from the elevation time series:

$$F_{\text{wave}}(t) = \rho_{\text{sea}}\,g\,A_{\text{col}}\,h_{\text{t}}(t) \tag{2.6}$$

Where:

- ρ_{sea} is the density of seawater,
- g is the gravitational acceleration,
- A_{col} is the plan area of the floating platform column,
- $h_{\text{t}}(t)$ is the wave height value at time t taken from the corresponding time series.

The wave moment $M_{\text{wave}}(t)$ is obtained by exploiting the time delay between the wave impacting the first and second column of the platform. This delay, denoted by τ, is calculated based on the wave phase speed and the geometric distance between the two application points. The formulation is:

$$M_{\text{wave}}(t) = \rho_{\text{sea}} \cdot g \cdot A_{\text{col}} \cdot l \cdot [h_1^{\text{ts}}(t) - h_2^{\text{ts}}(t + \tau)] \tag{2.7}$$

Where:

- l_{plat} is half the longitudinal distance between the columns.
- $h_1^{\text{ts}}(t)$ and $h_2^{\text{ts}}(t + \tau)$ are the wave elevations on the two columns, obtained from the same time series with application of the phase shift τ.

This model introduces relevant assumptions: planar waves, rectilinear propagation, absence of reflection and neglected platform-wave interaction. Furthermore, fluid dynamics is here reduced to a purely hydrostatic component, neglecting dynamic contributions (slamming, viscous drag, added mass).

Finally, the duration of the time window (60 s) and the sampling rate (0.01 s) result in a limited spectral resolution, which does not allow for the capture of low-frequency contributions (swell) or long-term modulations.

Despite these limitations, the proposed approach is effective in reproducing the main dynamic environmental effects in a structured and repeatable manner, and is fully compatible with the objective of testing controllers in simplified but physically coherent architectures. The possibility of numerically efficiently handling multiple environmental combinations (bins) and isolating the controller's behaviour from the acting forces is a further advantage of this modelling.

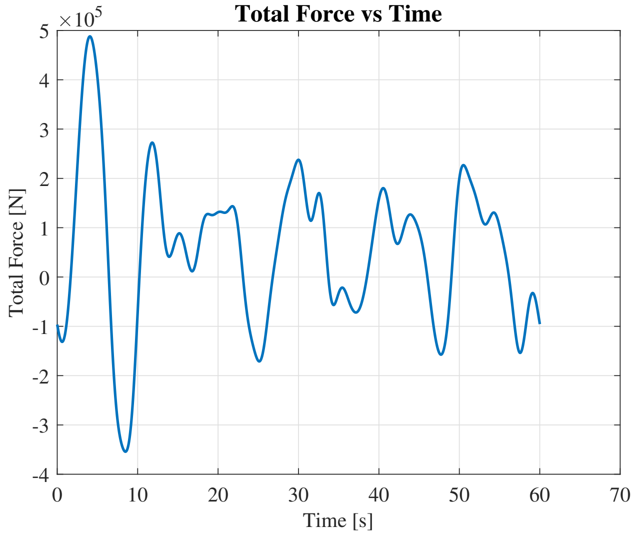

(a) Total forces over time of a representative central bin

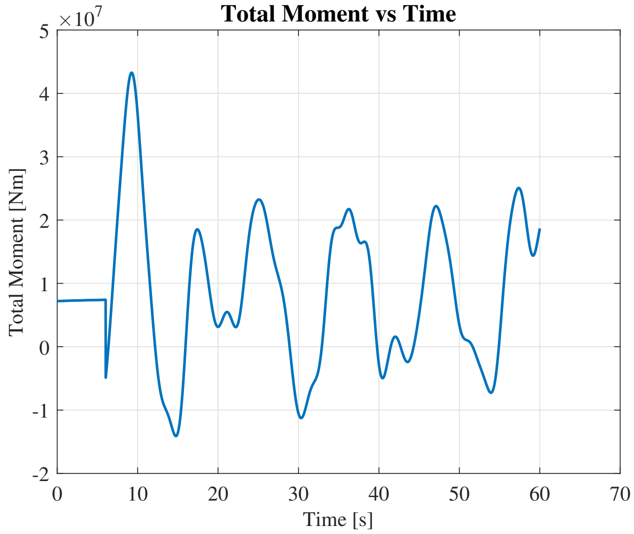

(b) Total moment over time for a representative central bin

Figure 2.5: Total forces and moment over time for a representative central bin

Extreme Operating Gust (EOG) Modelling

In the context of dynamic modelling of floating wind platforms, the Extreme Operating Gust (EOG) represents one of the most critical load cases for structural verification, as prescribed by IEC 61400-1:2019. This type of gust simulates a severe transient event characterised by a sudden and localised increase in wind speed, having a limited duration (typically 10.5 s) and an amplitude determined by site-specific turbulence conditions. Its function is to generate an aerodynamic pulse capable of significantly stressing the tower, mooring cables and platform, to test the robustness of the system under extreme but statistically plausible operating conditions.

In our work, the EOG was implemented considering the wind contribution alone, excluding hydrostatic and hydrodynamic effects generated by waves, in order to isolate and understand the pure aerodynamic impulse response. At a probabilistic level, the wind was considered constant and equal to the average speed of the central bin (11 m/s), corresponding to nominal operating conditions of the turbine, and for simplicity, it was assumed that the gust develops on this average value. In the present work, the turbine was classified as belonging to class A, for which, according to the specifications of the IEC 61400-1 standard, the value of the reference turbulence coefficient is $I_{\text{ref}} = 0.16$. Considering also that the hub height of the analysed turbine is greater than 60, the scaling parameter of the longitudinal turbulence is assumed to be $\Lambda = 42$, as expected for large wind turbines.

Starting from these parameters, the determination of the extreme gust is carried out according to the standard Extreme Operating Gust (EOG) procedure. Specifically, the average wind speed corresponding to the gust is first calculated, through the minimisation of the function describing the time course of the transient disturbance. Subsequently, the temporal profile of the gust speed is generated, using the analytical expressions provided by the regulation.

From this profile, the thrust force over time applied to the turbine is derived, according to the relationship:

$$F_{\text{gust}}(t) = \frac{1}{2}\rho_{\text{air}} C_T A_{\text{rot}} [v_{\text{gust}}(t)]^2 \tag{2.8}$$

Where:

- ρ_{air} is the air density,
- C_T is the turbine thrust coefficient,
- A_{rot} is the area swept by the rotor,
- $v_{\text{gust}}(t)$ is the time profile of the wind speed during the gust.

This force represents the transient aerodynamic reference input used to evaluate the dynamic response of the system (in particular, the maximum pitch). [1]

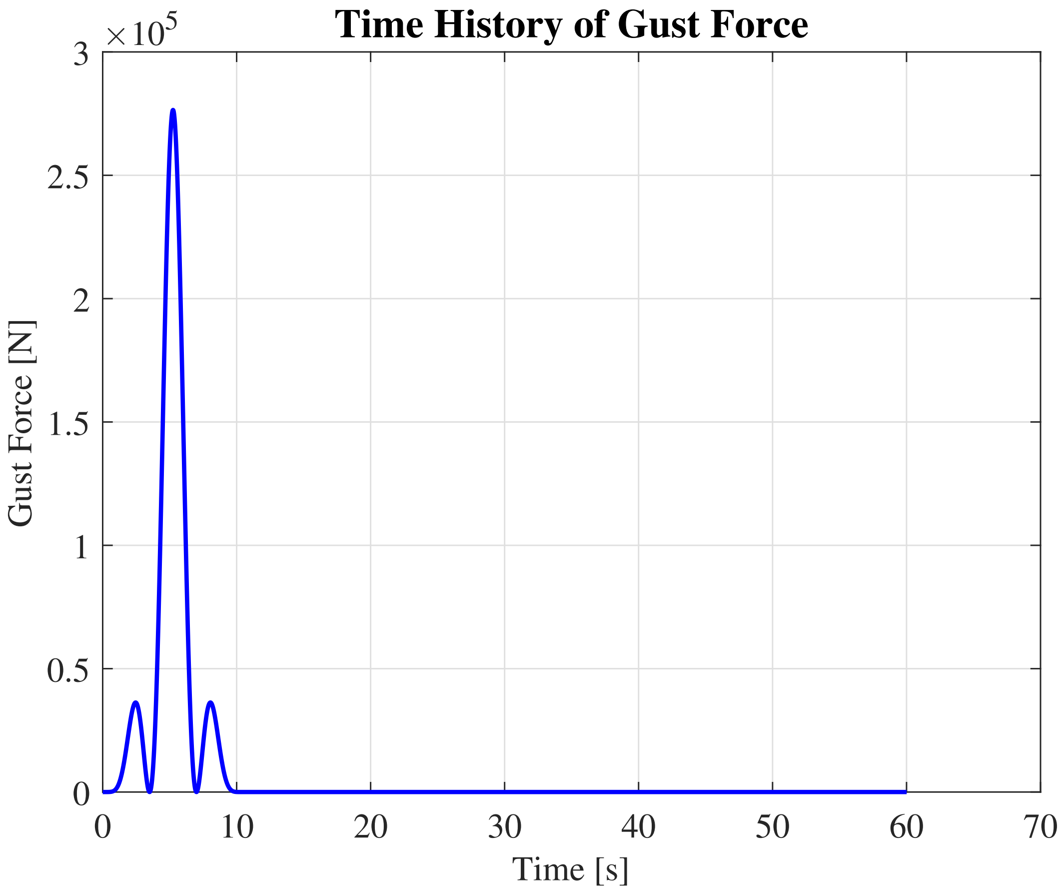

Figure 2.6: Gust force over time

2.3.2 Control Theory

As part of this thesis work, an active control methodology was implemented for stabilizing a floating offshore wind platform in deep water by directly acting on the tension of the mooring cables using controlled electric motors. In order to modify the dynamic response of the system in the presence of realistic environmental forcings (wind and waves), a state feedback control strategy based on the pole placement technique was adopted.

The mathematical formulation starts from the state-space representation of the continuous linear dynamic system:

$$\begin{aligned} \dot{\mathbf{x}}(t) &= \mathbf{A}\,\mathbf{x}(t) + \mathbf{B}\,\mathbf{u}(t), \\ \mathbf{y}(t) &= \mathbf{C}\,\mathbf{x}(t) \end{aligned} \tag{2.9}$$

where $\mathbf{x}(t) \in R^n$ is the state vector describing the dynamic variables of the system (in this case, vertical translation z, pitch θ, and their derivatives), $\mathbf{u}(t)$ represents the vector of control inputs (i.e., the forces acting in the cables via the motors), and $\mathbf{y}(t)$ the vector of measured outputs. The state feedback technique involves applying a shape control:

$$\mathbf{u}(t) = -\mathbf{gain}{*}\mathbf{x}(t) \tag{2.10}$$

where $\mathbf{gain} \in R^{m\times n}$ is the gain matrix to be determined. The effect of this control law is to change the dynamic matrix of the system, which becomes:

$$\mathbf{A}_{\text{cl}} = \mathbf{A} - \mathbf{B}{*}\mathbf{gain} \tag{2.11}$$

The poles of the closed-loop system are the eigenvalues of the matrix A_{cl} and completely determine its time and frequency response. The necessary condition for the full implementation of the technique is the complete controllability of the system, which occurs if the controllability matrix

$$C = \begin{bmatrix} B & AB & \cdots & A^{n-1}B \end{bmatrix} \tag{2.12}$$

has full rank n. [40, 42, 38, 32]

In the present study, the system was modeled with two degrees of freedom (heave and pitch), resulting in a linear model with four states and two control inputs. Once the model was validated by simulations under open-loop conditions, state feedback control was applied to analyze the effect of pole placement on the dynamic response of the platform. For this purpose, three distinct sets of complex conjugate eigenvalues were selected, each characterized by different real and imaginary parts. Physically and mathematically, each complex eigenvalue of the closed-loop system can be expressed in the form:

$$\lambda = \sigma \pm j\omega_d \tag{2.13}$$

where $\sigma < 0$ is the real part, governing the exponential decay rate of the transient response, and ω_d is the imaginary part, corresponding to the angular frequency of the damped oscillation.

The associated natural pulsation is defined as:

$$\omega_n = \sqrt{\sigma^2 + \omega_d^2} \tag{2.14}$$

while the damping ratio is given by:

$$\zeta = -\frac{\sigma}{\omega_n} \tag{2.15}$$

A value of $\zeta < 1$ indicates underdamped behavior, $\zeta = 1$ corresponds to the critically damped case (no oscillations), and $\zeta > 1$ identifies an overdamped regime.

From a design perspective, the choice of pole locations enables precise control over the trade-off between response speed, oscillation damping, and control effort. Poles with more negative real parts (i.e., located further to the left in the complex plane) imply faster decay and shorter settling times, but at the cost of increased control energy and potential numerical instability. Conversely, poles located closer to the imaginary axis yield slower, oscillatory responses. In the specific case, the three selected sets of closed-loop poles were chosen to investigate distinct dynamic configurations of the floating platform: [36, 42, 38, 32]

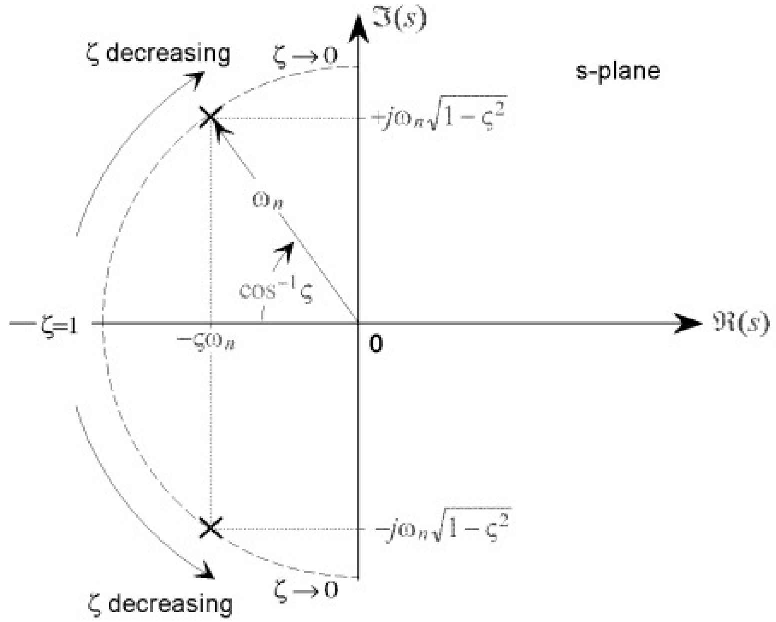

Figure 2.7: Response in terms of Poles and Zeros of Transfer Function. [3]

- **Light control (p_{light})**: eigenvalues with real part $\sigma \approx -0.02$ and high imaginary part ω_d, corresponding to a low damping ratio $\zeta \approx 0.1$. This configuration is associated with lightly damped dynamics and prolonged persistence of oscillations.

[3]Source: [36]

- **Aggressive control in frequency ($p_{\mathbf{freq}}$)**: eigenvalues with $\sigma \approx -0.3$ and $\omega_d \in [0.33, 0.94]$, yielding an intermediate damping ratio $\zeta \approx 0.7$. This setting allows to effectively avoid resonant interactions with the dominant frequency components of the wave excitation spectrum.

- **Aggressive control in damping ($p_{\mathbf{damp}}$)**: eigenvalues with $\sigma \approx -0.6$ and very low ω_d, resulting in a high damping ratio $\zeta \approx 0.95$. This configuration nearly suppresses oscillatory behavior, thus minimizing cyclic loads on the mooring lines and dynamic accelerations on the tower structure.

As illustrated in Figure 2.8, the location of the poles in the complex plane directly governs the transient response in terms of amplitude, frequency content, and decay rate. The imaginary axis represents pure oscillatory behavior, while the displacement along the real axis determines the rate of exponential decay. Poles near the origin lead to slow, potentially unstable dynamics, whereas poles further to the left in the complex plane ensure faster and more stable responses—though at the expense of higher energy consumption by the active mooring cable actuators.

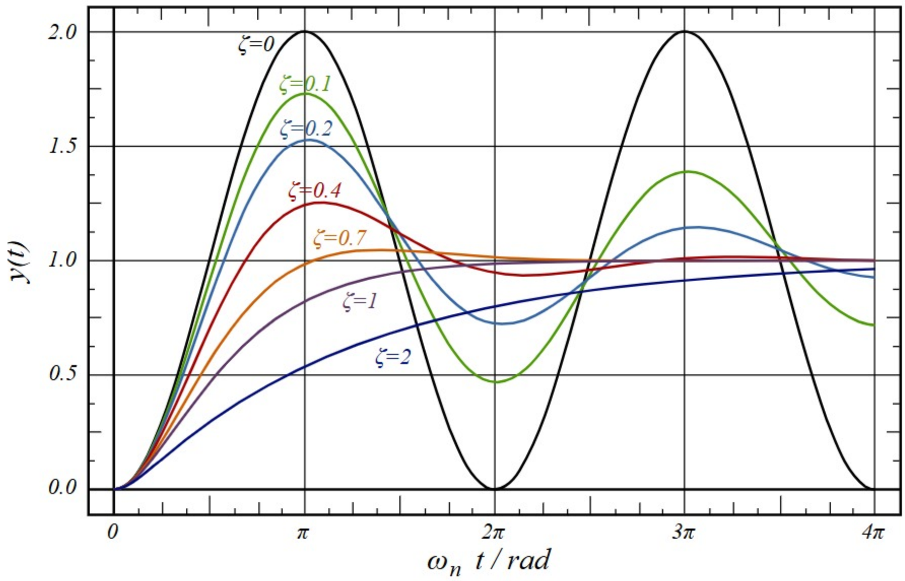

Figure 2.8: Schematic representation of the effect of pole position on the system response in terms of damping ratio.[4]

Pole placement, therefore, enables precise control of platform dynamics, adaptable to different operational priorities: dampening oscillations, reducing fatigue loads or minimizing energy consumption. [44]

[4]Source: [44]

Chapter 3

Scope, Objectives and Modelling Strategy

3.1 Research Objectives and Key Questions

This thesis aims to investigate the effectiveness of active control strategies applied to mooring cables in enhancing the dynamic stability of floating wind platforms deployed in deep water. The main objective is twofold: on the one hand, to suppress oscillations in the most critical degrees of freedom (heave and pitch); on the other hand, to mitigate structural accelerations and dynamic loads, while ensuring that the energy consumption associated with control actuation remains within technically and economically acceptable limits.

In this framework, the following research questions have guided the model development and simulation campaign:

- To what extent can active control of mooring cables reduce vertical and rotational oscillations of the platform under combined environmental loading (wind, waves, current)?
- Can the implementation of an active control system lead to a measurable reduction in dynamic loads and fatigue damage in mooring cables?
- What is the energy cost associated with the control implementation, and how does it vary as a function of the adopted control strategy (e.g. open-loop vs. feedback control)?

To address these questions, a simplified yet physically representative dynamic model with two degrees of freedom was developed. This allowed for a transparent evaluation of the influence of external environmental actions and control inputs on the platform's dynamic response

3.2 Modelling Choices and semplification strategies

This thesis lies within a rapidly expanding field of research, which nevertheless requires numerical tools, advanced software and multidisciplinary skills in order to comprehensively model the behaviour of offshore floating platforms.

Given the limited timeframe of the project, and the complexity of software commonly used in industry (such as OpenFAST, OrcaFlex or SIMA), it was decided to develop from scratch a simplified dynamic model of the platform, built and simulated entirely in the MATLAB environment. The aim was to ensure maximum transparency on the modelling steps and maximum controllability of the system, while accepting a certain degree of idealisation.

In particular, the platform was modelled as a system with two degrees of freedom (DOFs): heave (vertical displacement) and pitch (rotation around the transverse axis). This choice was motivated by two main factors:

- Physical representation: heave and pitch are the two predominant modes of response in semi-submersible platforms subject to wave and wind excitation. Pitch is particularly critical as it directly affects the inclination of the tower and thus the angle of attack of the rotor. Vertical oscillation (heave), on the other hand, governs changes in elevation that influence mooring line tension and hydrostatic restoring forces.

- Controllability and effectiveness of the active system: focusing on two degrees of freedom enables a clearer and more effective assessment of the potential of an active control system based on mooring line actuation, evaluating its impact on platform stability, structural accelerations, and fatigue loading. The active control is also very expensive in terms of energy consumption, so we chose to focus only on the two dofs that are more likely to be source of motion in the platform.

3.3 Structure and Flow of the Thesis

The thesis is articulated in five main chapters, structured to provide a coherent transition from theoretical background to numerical implementation and analysis:

- Chapter 1: Introduction to the global context of energy transition, with emphasis on the strategic role of offshore wind power in decarbonisation scenarios
- Chapter 2: Overview of foundation technologies and structural typologies for floating offshore platforms, including discussion of dynamic phenomena and rationale behind the adopted modelling simplifications, in chapter 2 there is also described in great detail all the theory used for this thesis and the explanation of the construction of the realisting environment where i have tested the platform
- Chapter 3: Scope of the thesis, reasearch questions and the modeling choices adopted for this thesis.
- Chapter 4:Construction of the two-degree-of-freedom model: formulation of the equations of motion, environmental excitation modelling (wind and wave), and implementation of controllable mooring lines, it is also explained in great detail the implementation of the static equilibrium configuration.
- Chapter 5: Design and comparison of different control strategies — both open-loop and closed-loop (e.g. proportional-derivative) — with quantitative evaluation of platform response, mooring loads, and energy expenditure.
- Chapter 6: Conclusions and outlook, with further implementation that can be done starting from my work.

This structure supports a rigorous and incremental investigation of the engineering challenges related to the stabilisation of floating offshore wind platforms via active mooring control.

Chapter 4

Modelling the Floating Platform: Structure and Dynamics

As already explained in the previous chapter, we are dimensioning a system comprising the platform, the tower and the RNA system. We are considering an approximate sea depth of 600 m. Among the reasons that led to the decision to adopt an operating depth of 600 metres, several technical, scientific, and strategic considerations were taken into consideration. First of all, this value was selected in order to explore an operating regime that has not yet been extensively investigated in the scientific literature, as there are currently no systematic studies available on the use of floating wind platforms at such depths. Therefore, it was considered appropriate to analyse the dynamic and structural behaviour of the system under extreme conditions, to contribute to the advancement of research in scenarios characterised by high bathymetric complexity. Second of all, the design hypothesis refers to a possible experimental application along the coast of Lazio, near Rome, where the optimal distance from the coastline for the installation of an offshore wind platform is approximately 25 kilometres. According to the available bathymetric data, this configuration corresponds to a sea depth of approximately 600 metres. Finally, as already discussed in Chapter 1, the Mediterranean Sea has significant energy potential for the development of offshore wind power, which is still largely unexploited. One of the main critical issues that slow down the expansion of these technologies in the region lies precisely in the morphology of the seabed, characterised by steep slopes and considerable depths even a short distance from the coast. In this context, the adoption of a floating platform optimised for deep waters is an essential step in making installations in the

Mediterranean accessible and technically feasible. The model of the system takes its cue from the UMaine VolturnUS-S platform developed for the 15-megawatt offshore IEA Wind reference wind turbine. In our project, unlike what is described in the IEA paper, we are also accurately dimensioning the tower and the RNA system; furthermore, our system only takes into account two degrees of freedom; the vertical translation of the system (z) and the rotation around the x-axis (θ); for this reason, changes will have to be made to what is stated in the report. [5]

4.1 System Architecture and Geometrical Configuration

The structure of the platform consists of four main columns: a central one, which acts as an interface with the wind tower, and three radial columns, which are equidistant from each other and connected to the central column by rectangular pontoons at the base and upper and lower cylindrical stays.

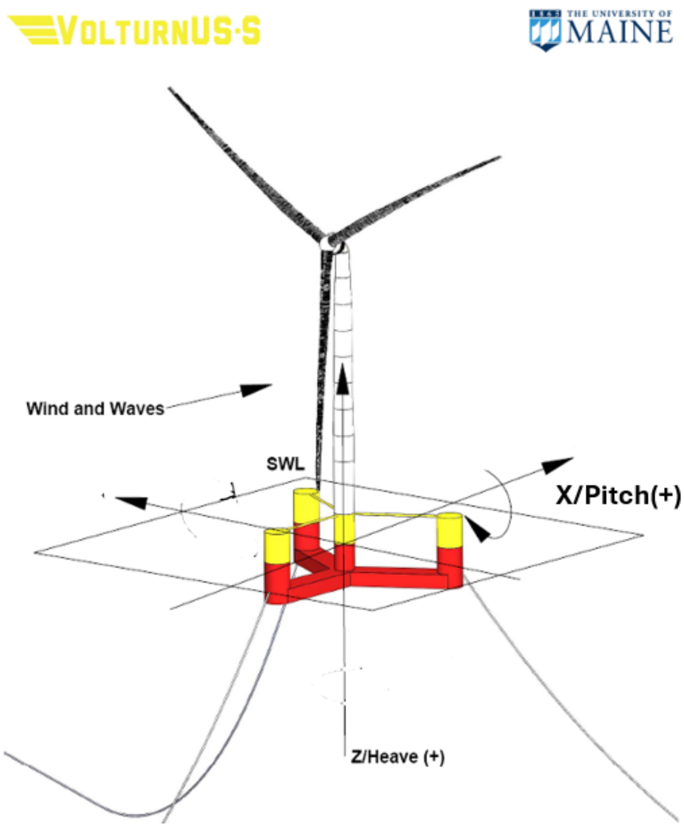

Figure 4.1: Floating offshore wind turbine reference coordinate system.[1]

4.1.1 General Geometry and Dimensions of the platform

According to the information provided in Table 4.1, the platform has a draught (draft) of 20 metres and a freeboard (distance between the waterline and the upper deck) of 15 metres, bringing the total submerged/emersed height of the platform to 35 metres. The rectangular pontoons connecting the outer columns to the central one are 12.5 metres wide and 7.0 metres high, while the radial stays have a diameter of 0.9 metres.

The three outer columns are positioned 51.75 metres away from the centre of the central column, forming an equilateral triangle. Each column has a diameter of 12.5 metres. The symmetrical arrangement of the columns provides stability with respect to rolling and pitching and allows an even distribution of loads. [5]

Table 4.1: Main geometric parameters of the semi-submersible platform

Parameter	**Value**
Draught (Draft)	20 m
Freeboard	15 m
Column diameter	12.5 m
Distance from central to outer column	51.75 m
Ponton width × height	12.5 m × 7.0 m
Radial stay diameter	0.9 m

[1]Source: Figure courtesy of the University of Maine

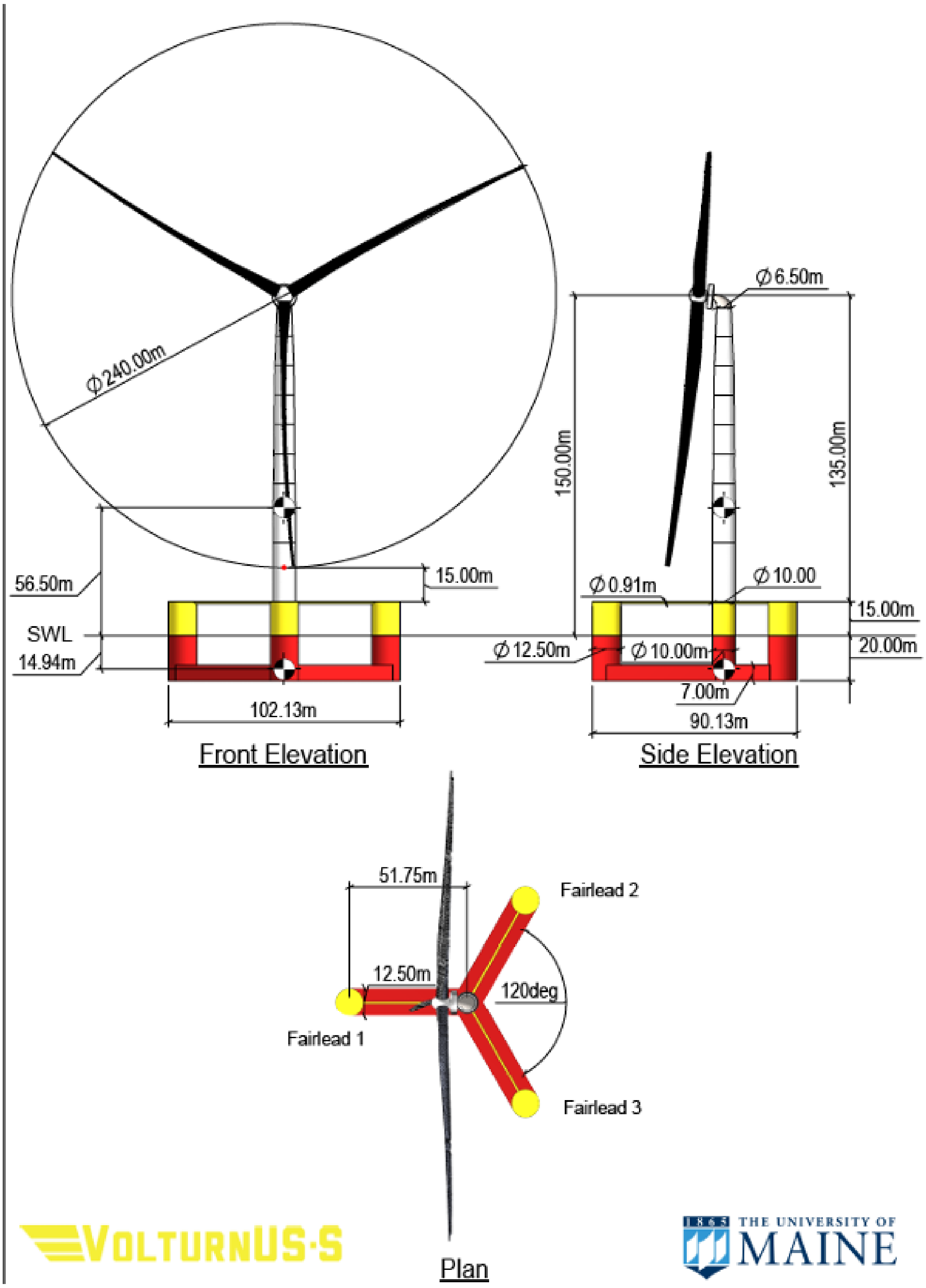

Figure 4.2: General arrangement.[2]

[2]Source: Figure courtesy of the University of Maine

4.1.2 weights of the platform

Floating Platform

The steel structure of the platform, including the three radial columns, the central column, and the connecting pontoons, has a total mass of 3,914 tonnes. This value refers exclusively to the primary structural steel and does not account for ballast or secondary components such as outfitting or appurtenances.

Ballast

Platform stabilisation is achieved through a dual ballast system composed of:

- **Fixed ballast:** 2,540 tonnes of ferro-concrete mix positioned at the base of the three radial columns.
- **Fluid ballast:** 11,300 tonnes of seawater stored within the lower floodable pontoons.

The combination of fixed and fluid ballast effectively lowers the platform's centre of gravity, contributing to enhanced static and dynamic stability by the design specifications. The operational draught of the platform is maintained at 20 metres. [5]

Table 4.2: Mass distribution of the UMaine VolturnUS-S platform (excluding RNA and tower)

Component	Description	Mass [t]	CG Height from SWL [m]
Steel Platform Structure	Columns, pontoons, and primary steel structure	3,914	–
Fixed Ballast	Iron-concrete ballast in outer columns	2,540	–
Fluid Ballast	Seawater ballast in lower pontoons	11,300	–
Total platform Mass	Sum of platform and ballast masses	**17,754**	**–14.94**

4.1.3 Inertia of the platform

The calculation of the principal moments of inertia plays a crucial role in the dynamic modelling of a floating wind platform, as it determines the structure's response to the rotational environmental loads induced by wind, waves, and current. In the case of the *UMaine VolturnUS-S* platform, designed to support the 15 MW IEA-15-240-RWT turbine, the inertia values are explicitly provided in the document *IEA Wind TCP Task 37* , and refer to the coordinate system centred in the centre of mass of the floating platform, excluding the tower and the turbine. The values stated in the report (Table 2, page 6) for the global moments of inertia of the floating platform are: [5]

- Rolling moment of inertia: $I_{yy} = 1.251 \times 10^{10}$ kg·m^2
- Pitch moment of inertia: $I_{xx} = 1.251 \times 10^{10}$ kg·m^2
- Yaw moment of inertia: $I_{zz} = 2.367 \times 10^{10}$ kg·m^2

These values are consistent with the symmetrical tri-radial planform configuration of the platform, consisting of:

- a vertical cylindrical central column housing the wind tower;
- three identical radial vertical cylindrical columns, arranged at 120°;
- three horizontal rectangular lower pontoons with cross section 12.5×7.0 m and length 51.75 m, connecting the central column to each radial column.

The above moments of inertia are calculated based on the following geometric and physical assumptions:

Geometry: Each structural sub-component (columns, pontoons, ballast) is modelled as a rigid body with simple shape (solid cylinder or rectangular prism).

Mass distribution: The mass of each component is assumed to be uniformly distributed.

Included mass: The total mass used for the calculation includes the steel structure, fixed ballast, and fluid ballast. The RNA and the tower are excluded (see Table 1, p. 3 and Table 2, p. 6).

Reference origin: The origin of the reference system is placed at the global centre of mass of the platform.

The radial columns, positioned 51.75 m away from the platform centre, constitute the most significant contribution to the moments of inertia in roll and pitch. The identical values of I_{xx} and I_{yy} are a direct consequence of the threefold axial symmetry of the platform geometry.

The rectangular pontoons, arranged radially and extending downward, contribute predominantly to the yaw inertia I_{zz}, which is approximately twice as large as the roll and pitch components.

Although the document *IEA Wind TCP Task 37* does not provide a complete analytical derivation of the global inertia values, the stated numbers are consistent with an elementary geometric decomposition based on classical expressions for rigid bodies: [5]

$$\begin{aligned} I_{\text{cylinder, axial}} &= \frac{1}{2}\, m\, r^2 \\ I_{\text{cylinder, transverse}} &= \frac{1}{4}\, m\, r^2 + \frac{1}{12}\, m\, h^2 \\ I_{\text{rect. prism}} &= \frac{1}{12}\, m\, (b^2 + h^2) \end{aligned}$$

In addition, for all components not centred at the platform's global centre of mass, the **parallel axis theorem** (Huygens–Steiner) is applied:

$$I = I_{\text{local}} + m\, d^2$$

Where d is the distance between the local centre of the sub-component and the global centre of mass of the platform.

Table 4.3: Principal moments of inertia of the UMaine VolturnUS-S platform (values referred to the platform centre of mass, excluding tower and RNA)

Inertia component	**Symbol**	**Value [kg·m^2]**
Roll moment of inertia	I_{yy}	1.251×10^{10}
Pitch moment of inertia	I_{xx}	1.251×10^{10}
Yaw moment of inertia	I_{zz}	2.367×10^{10}

4.2 Modelling of the upper components

In the official IEA Wind report for the 15 MW offshore reference turbine (NREL, 2020), each major component of the system is described in sufficient detail to support implementation in multibody aero-elastic and dynamic models.

The turbine is divided into distinct subsystems: tower, blades, hub, RNA (Rotor-Nacelle Assembly), and nacelle, including several mechanical sub-components such as the yaw system, generator, shaft, and support plate.

For each of these elements, the following data are provided:

- mass,
- vertical position of the centre of mass with respect to the still water level (SWL),
- when available, the moment of inertia with respect to the transverse x-axis (pitch).

4.2.1 Geometry and masses of the Upper Components

Tower

The tower is modelled as a cylindrical steel shell with a variable circular cross-section. The diameter at the base is 10.0 m and gradually decreases to 6.5 m at the top, with an overall height of 129.495 m. The total mass of the tower is 860 t, and its vertical centre of mass is located at +50.22 m above the still water level (SWL). [15]

The report explicitly states that the tower is axially symmetrical; thus, the transverse coordinates of the centre of mass are null:

$$x = 0, \quad y = 0 \tag{4.1}$$

The moment of inertia concerning the pitch axis (x-axis) is not directly provided. However, it can be estimated by modelling the structure as a hollow cylinder, knowing that the diameter of the tower didn't change much compared to its length. In order to be very precise, we need to know the mass distribution along the tower, data that is not specified in the report. For this reason, we are using the following analytical expression:

$$I_{xx} = \frac{1}{12} m_{tower} \left(3(r_1^2 + r_2^2) + h_{\text{tower}}^2\right) \approx 1.2 \times 10^9 \text{ kg} \cdot \text{m}^2 \tag{4.2}$$

where:

- I_{xx} is the moment of inertia of the hollow cylindrical tower concerning (x-axis).
- m_{tower} is the total mass of the tower [kg].

- r_1 is the inner radius of the tower [m].
- r_2 is the outer radius of the tower [m].
- h_t is the total height of the tower [m].

Blades

Each blade is modelled as a slender beam with a variable mass distribution, defined by a sequence of aerofoil sections and structural data along its length. The mass of a single blade is 65.25 t. The longitudinal centre of mass of each blade is located approximately 26.8 m from the blade root. The global coordinates of the blade centre of mass in the (x, y, z) reference system depend on the angular orientation of the blade concerning the hub. In simplified models, the blades are mounted radially on the hub and treated as an integral part of the rigid rotor. To estimate the moment of inertia of the blades, we can assume that the mass is equally distributed along the blades, and we can consider the system of the three blades as a rigid disk. For this reason, we are using this analytical formula:

$$I_{xx}^{\text{blades}} = \frac{1}{2} m_{\text{blades}} r_{\text{blades}}^2 \approx 1.41 \times 10^9 \ \text{kg} \cdot \text{m}^2 \tag{4.3}$$

where:

- I_{xx}^{blades} is the moment of inertia of the three blades treated as a rigid disk [kg·m^2],
- m_{blades} is the total mass of the three blades [kg].
- r_{blades} is the effective radial position of blade center of mass (approx. 26.8 m) [m]. [15]

Hub and Rotor

The hub is modelled as a rigid spherical shell to which the three blades are attached. It has a mass of 190 t, and its centre of gravity is located at +10.6 m above the SWL. The rotor, understood as the union of the hub and three blades, has an aggregate mass of 385.75 t.

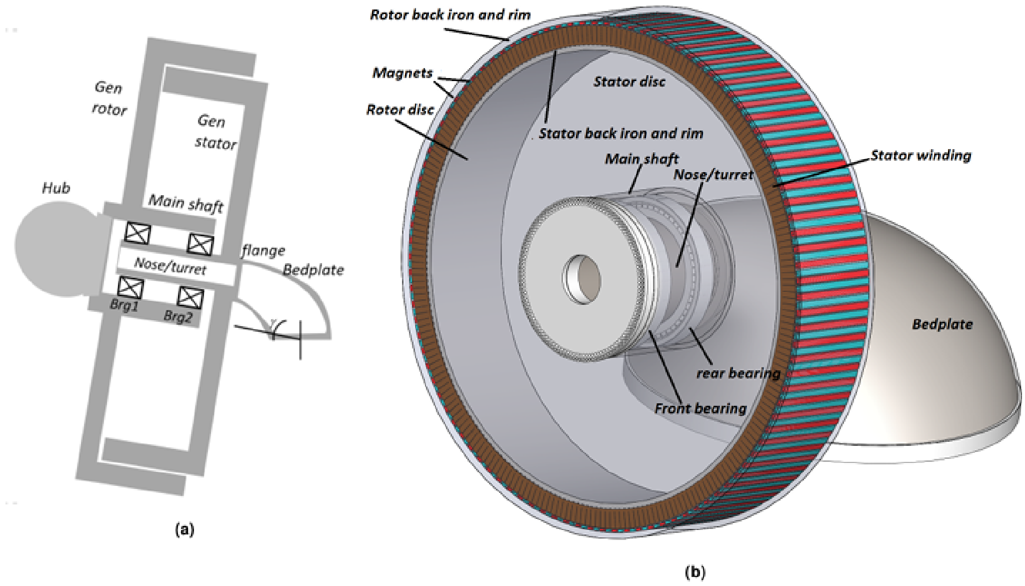

Figure 4.3: A sketch and CAD model of the nacelle layout of the 15-MW direct-drive wind turbine. Not to scale and some structural details omitted. Blades (not shown), hub, shaft, and generator rotor rotate [3]

In the simplified dynamic model, the rotor is treated as a rigid rotating body. The moment of inertia with respect to the x-axis for the hub alone is given as:

$$I_{xx}^{\text{hub}} = 1.38 \times 10^6 \ \text{kg}\cdot\text{m}^2 \tag{4.4}$$

Nacelle and Subcomponents

The nacelle has a total mass of 820.89 t and its centre of gravity is located at +3.978 m from the origin of the coordinate system. The internal subcomponents of the nacelle are represented by individual lumped masses and associated inertia values as follows:

[3] [15]

Table 4.4: Lumped Masses, CG Height (The coordinate system has its origin at the tower top)and I_{xx} for the Nacelle Assembly [4]

Component	**Mass [t]**	Z_{TT} **[m]**	I_{xx} **[kg·m^2]**
Yaw system	100.000	-0.190	490,266
Turret nose	11.394	4.956	12,571
Inner generator stator	226.629	4.913	3,777,313
Outer generator rotor	144.963	5.033	3,173,003
Shaft	15.734	5.000	33,009
Hub	190.000	5.462	1,382,171
Bedplate	70.329	2.697	398,973
Flange	3.946	4.831	4,081
Misc. equipment	50.000	0.000	16,667
TDO shaft bearing	2.230	5.040	3,515
SRB shaft bearing	5.664	4.914	8,930
Nacelle total	**820.888**	**3.978**	**12,607,277**
Nacelle w/o hub	**630.888**	**3.352**	**10,680,747**

RNA (Rotor–Nacelle Assembly)

The Rotor–Nacelle Assembly (RNA) includes the hub, blades, and nacelle structures. The total mass of the RNA is 1,017 t, and its vertical centre of gravity is located at +109.17 m above the SWL.

In rigid-body structural models, the RNA is represented as a concentrated mass located at the top of the tower. The equivalent moment of inertia for the assembly results from the sum of the individual contributions of its sub-components.

Here, there is a summarized table that takes into account all the data used in the present work [15]

Table 4.5: Summary of global properties of platform, tower, RNA, and blades (relative to SWL)

Component	**Mass [t]**	**CG Height from SWL [m]**	I_{xx} **[kg·m^2]**
Platform	17,754	–14.94	1.251×10^{10}
Tower	860	+50.22	1.2×10^{9}
RNA (hub + nacelle)	820.888	+148.47	1.260×10^{7}
Blades (3)	195.75	+176.76	1.41×10^{9}

[4]Source: Table 5-1,[15]

4.3 Calculation of the Total Centre of Mass of the System

In the context of dynamic modelling with reduced degrees of freedom, particularly for analyses in pitch (rotation about the x-axis) and vertical translation (heave along z), it is essential to accurately determine the vertical coordinate of the overall centre of mass of the system.

Since the VolturnUS-S platform and all the upper components of the IEA 15 MW turbine are mounted in an axially symmetrical configuration along the central column, the transverse coordinates of the centre of mass (x, y) are zero by design. Therefore, the overall centre of gravity can be fully characterised by its vertical position z_{CG}, measured relative to the still water level (SWL), along the global vertical axis.

The total vertical position of the centre of mass is computed as a mass-weighted average using the following expression:

$$z_{\mathrm{CG,tot}} = \frac{\sum m_i \cdot z_i}{\sum m_i} \tag{4.5}$$

Where m_i is the mass of component i, and z_i is the vertical position of its centre of gravity relative to the SWL.

Applying the above formula yields a total system mass of 19,487.84 t and a vertical position of the global centre of mass equal to:

$$z_{\mathrm{CG,tot}} = -3.34 \text{ m relative to the SWL} \tag{4.6}$$

This value will be used as a reference in the two-degree-of-freedom dynamic models for deriving the equations of motion and evaluating the hydrostatic behaviour of the integrated platform–turbine system.

4.4 Inertias of the system

4.4.1 Total Moment of Inertia with Respect to the Pitch Axis

In the context of two-degree-of-freedom (2-DoF) dynamic modelling, which considers only pitch motion (rotation about the x-axis) and vertical translation (heave), it is essential to accurately determine the total moment of inertia with respect to the x-axis, computed relative to the global centre of mass of the system.

Starting from the established position of the global centre of mass along the vertical axis ($z = -3.34$ m), the parallel axis theorem (also known as the Huygens–Steiner theorem) is applied to translate each local moment of inertia $I_{xx,\text{local}}$ to the global barycentric reference frame. The equivalent moment of inertia for each component is then obtained using the following expression:

$$I_{xx} = I_{xx,\text{local}} + m \cdot d^2 \tag{4.7}$$

Where m is the mass of the component and d is the vertical distance between the component's local centre of mass and the global centre of mass of the system.

The total moment of inertia of the system with respect to the overall centre of mass is thus:

$$I_{xx,\text{tot}} \approx 4.29 \times 10^{10}\ \text{kg}{\cdot}\text{m}^2 \tag{4.8}$$

This value is employed in the reduced dynamic models to describe the inertial pitch response of the tower–platform–turbine system, ensuring strict consistency with the geometric and structural distribution of the subsystems.

4.5 Computation of the Static Equilibrium of the Platform

Once the physical and geometric system under consideration has been fully defined, the first fundamental step is to determine the static equilibrium configuration of the floating platform. From this configuration, it is possible to proceed with the calculation of the stiffness, damping and mass matrices of the system, obtained by studying the variation of the resulting forces in response to small perturbations around the equilibrium position. In the present work, this analysis was conducted assuming a constant value of the sea current velocity of 1 m/s, while the wind velocity was assumed to vary for each bin considered in the environmental domain. For each value of the reference wind speed, the corresponding static configuration was calculated, including the static tensions in the mooring cables, from which the dynamic properties of the system were derived. This approach made it possible to generate a set of dynamic matrices (mass, damping, stiffness) specific to each bin, subsequently enabling the simulation of the dynamic response of the platform over time under realistic environmental conditions. Please refer to the previous chapter and Appendix A for a detailed description of the environmental bin discretisation method and the assumptions implemented, and refer to Appendix B for further detail on the determination of the static equilibrium.

This section will describe how the cable tension and system matrices were calculated, together with the approximations adopted. For purposes of exposition, these procedures will be illustrated by referring to a generic bin, i.e., corresponding to a generic wind speed condition. This choice makes the discussion clearer and more readable, without loss of generality, as the calculation was subsequently extended to all the environmental conditions considered. The key variable for determining static equilibrium is the static pitch angle of the platform. To this end, a function was developed in the MATLAB environment which, starting from the value of the aerodynamic force considered, establishes for each cable whether it is in a taut or slack configuration. Based on this classification, the vertical components of the forces exerted by the cables are calculated, from which the overall moment due to the mooring system is obtained. Knowing the latter, it is possible to resolve the balance of moments around the center of mass and thus determine the value of the static pitch angle of the platform.

step 1

The first task was to calculate the lateral cable forces needed to counter the lateral wind and current forces. We have to solve this system that takes into consideration the three mooring cables and the two forces that we are now taking into account, wind and current. where α_{wind} and α_{current} represent the directions of the wind and current forces, respectively. The mooring cables are arranged at fixed angles, each separated by 120°.

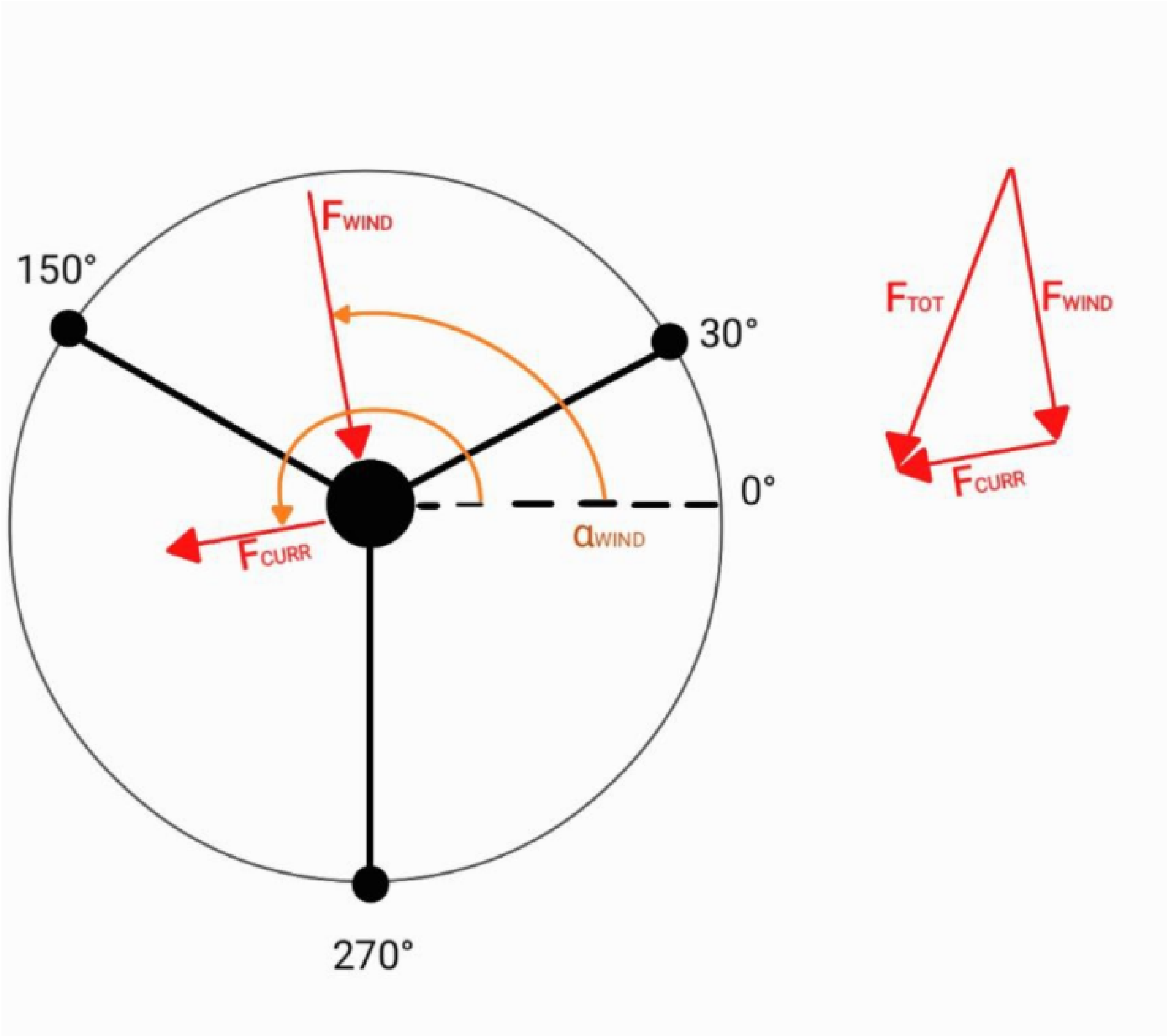

Figure 4.4: Direction of wind and current forces

Step 2.

After having calculated the total force in the system, we are now able to solve the equation to determine the tension on each of the three cables.

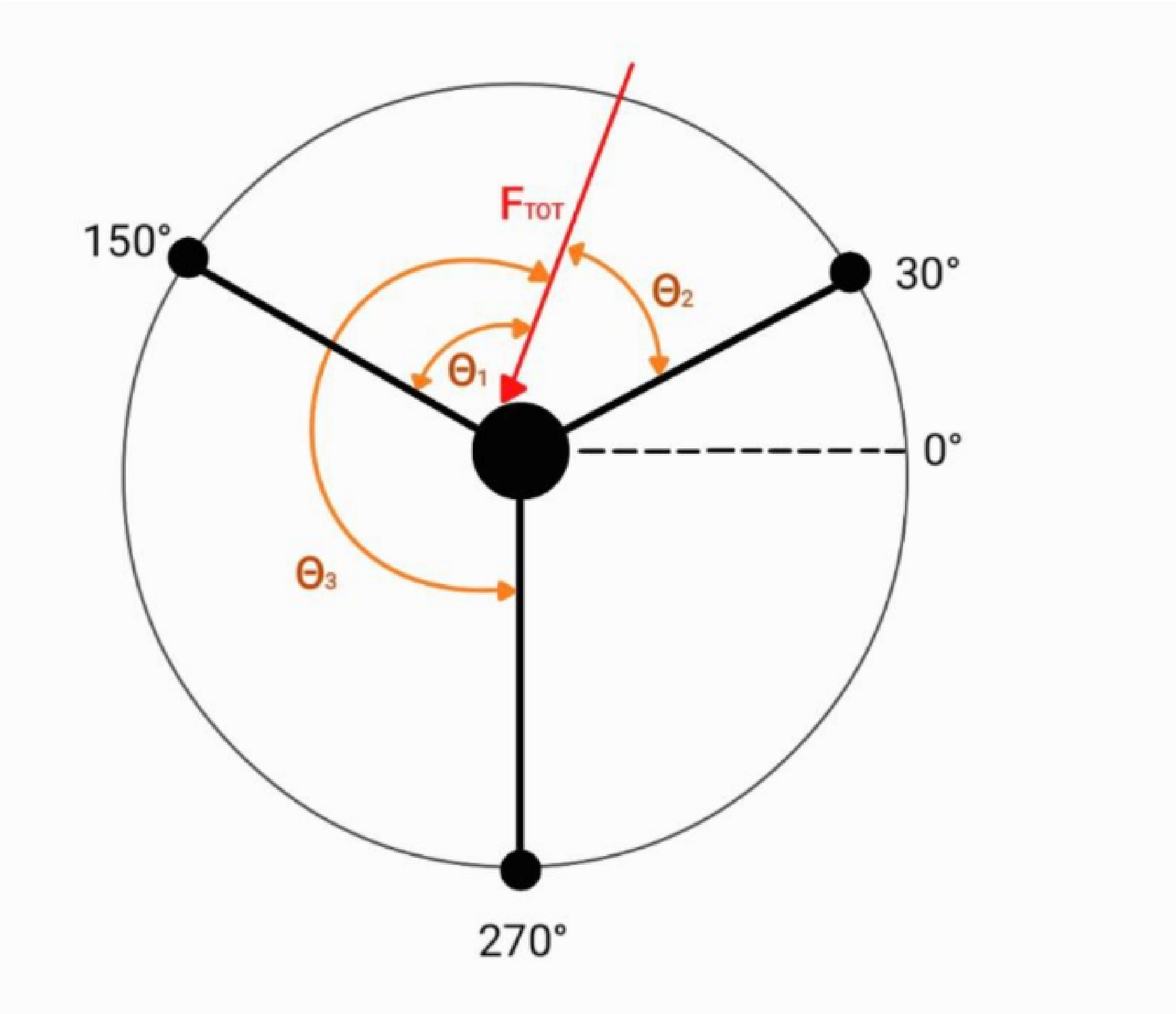

Figure 4.5: System configuration

In this thesis we are only considering the cases where either one or two cables are active. Starting from this assumption we are excluding all the cases where all the three cables are active at the same time. Here we are going to show two different system of equations, one used when only one cable is active, the other used when two cables are active. For an easy reading of this thesis we are only reporting here the case where cable 1 is active for the first case, and where cable 1 and 2 are active for the second case, knowing that we have considered all the possible combinations. 1) System of equation for T1

$$T_1 = \vec{F}_{\text{tot}} \cdot \hat{t}_1 = F_{\text{tot}} \cos(\theta_1) + 0 \cdot \sin(\theta_1) = F_{\text{tot}} \cos(\theta_1) \tag{4.9}$$

2) System of equations for T1 and T2

$$
\begin{cases} T_1 \cos(\theta_1) + T_2 \cos(\theta_2) = F_{\text{tot}} \\ T_1 \sin(\theta_1) - T_2 \sin(\theta_2) = 0 \end{cases} \tag{4.10}
$$

Step 3.

Once we have calculate the tension inside each cable we can now calculate the down forces for both the taut and slack configuration, then we have to calculate the angle between the lateral force that we have just found and the cable, to understand if we are in a taut or slack configuration, so we can select the right force for the momentum.

Step 4: Taut configuration

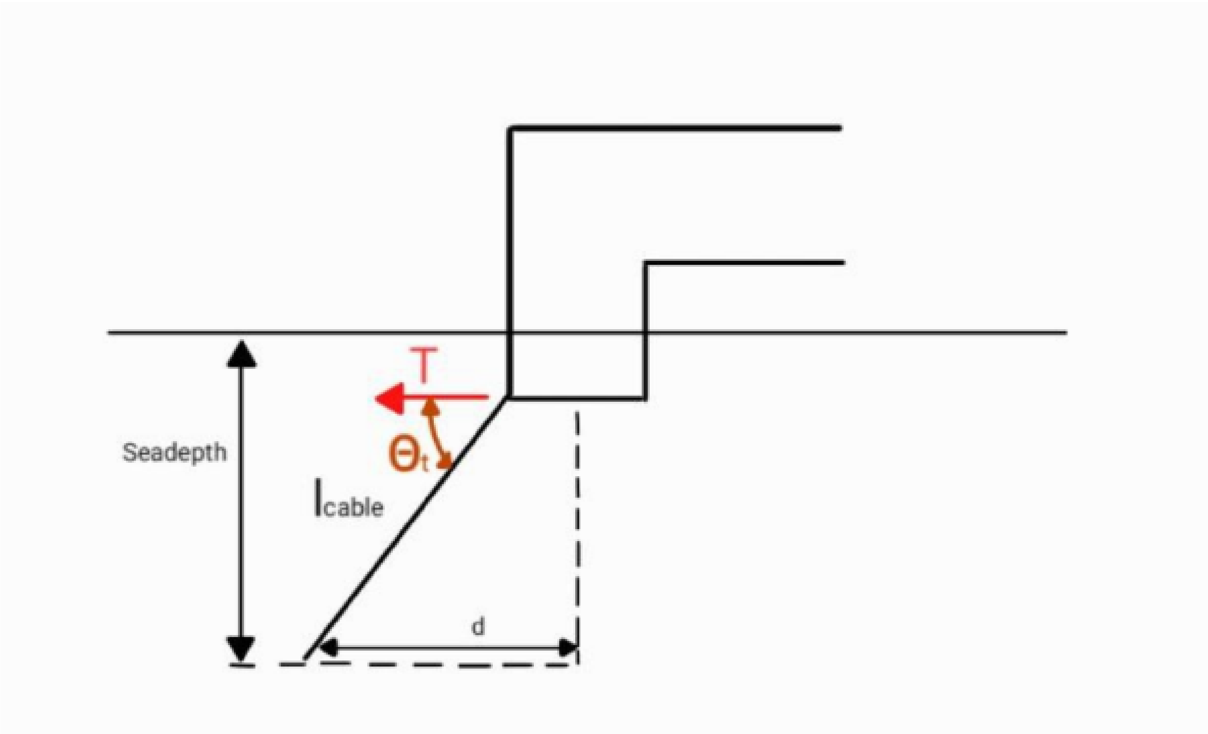

Figure 4.6: taut configuration

$$
\theta_t = \arcsin\left(\frac{\text{sea\_depth}}{\ell_{\text{cable}}}\right) \tag{4.11}
$$

$$
d = \sqrt{\ell^2_{\text{cable}} - \text{sea\_depth}^2} \tag{4.12}
$$

$$
F_{\text{down}} = \frac{T \cdot \text{sea\_depth}}{d} \tag{4.13}
$$

Step 5: Slack configuration

In the slack configuration, because the platform supports all the weight of the cable, we can calculate the down force directly from the length of the cable.

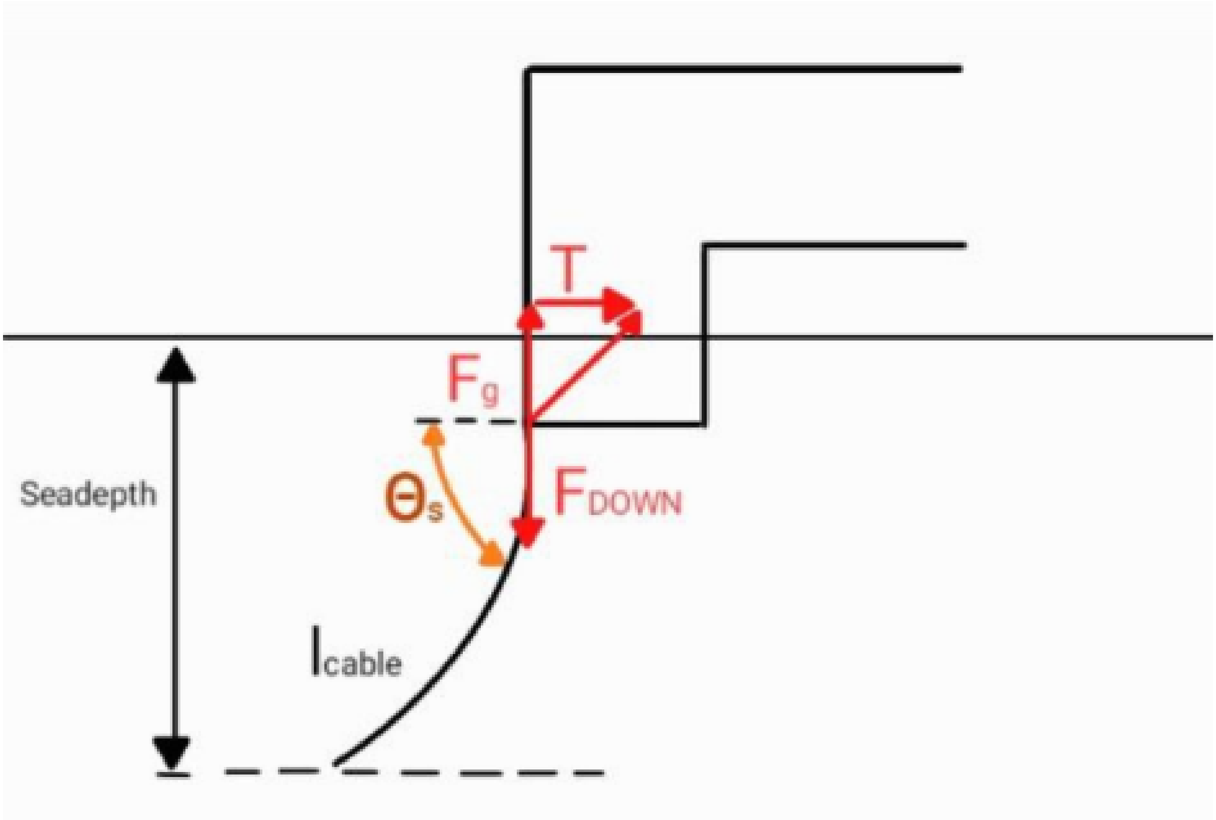

Figure 4.7: Slack Configuration

$$F_g = \rho A\,\ell_{\text{cable}} \tag{4.14}$$

$$\theta_s = \arctan\left(\frac{F_g}{T}\right) \tag{4.15}$$

$$F_{\text{down}} = F_g \tag{4.16}$$

Step 6

Now that we have calculated the angles and the down forces for each configuration, we can implement a logic equation to determine which force we have to use for each cable. In fact

$$\text{If } \theta_s > \theta_t \text{, the cable is } \textbf{slack}\text{; otherwise, the cable is } \textbf{taut}. \tag{4.17}$$

Step 7

Now that we know which down force we have to use for each cable, we can finally calculate the static pitch angle as follows:

$$M_{\text{cable}} = +F_{\text{down},1} \cdot (\ell_{\text{plat}} \cos(30)) - F_{\text{down},2} \cdot (\ell_{\text{plat}} \cos(30)) + F_{\text{down},3} \cdot \cos(\gamma) \tag{4.18}$$

$$M_{\text{wind}} = F_{\text{wind}} \cdot h_{\text{RNA}} \tag{4.19}$$

$$M_{\text{res}} = M_{\text{wind}} - M_{\text{cable}} \tag{4.20}$$

$$\text{res} = \frac{M_{\text{res}}}{2 \cdot \ell_{\text{plat}}^2 \cdot A_{\text{circle}} \cdot g \cdot \rho_{\text{sea}} \cdot C_V} \tag{4.21}$$

$$\theta_{\text{eq}} = \arcsin(\text{res}) \tag{4.22}$$

4.6 Stiffness matrix

Once the static equilibrium configuration is determined, after having calculated a set of tensions inside the cable for each bin, we then proceed with the determination of the matrices of the system. (Please refer to the previous section and Appendix B for further explanations on how the tension in the cables and the static pitch angle were calculated.)

In the dynamic behaviour of a floating offshore wind platform anchored with taught or semi-taut cables, the elastic response of the system is governed by two fundamental stiffness contributions, which add up in the overall linear model and act in a coupled manner in the different degrees of freedom. These contributions are: (1) geometric stiffness related to the deformed configuration, and (2) buoyancy stiffness, related to the variation of Archimedes thrust as a function of displacement.

In order to calculate the stiffness matrix, we had to calculate the contribution of each of the two degrees of freedom of the model, the vertical translation and the rotation along the x-axis. In our simplified model, we have made two assumptions that are very important to determine these terms of the stiffness matrix.

1. We can assume that there is a contribution of each term in the stiffness matrix, just when the cable is in a taught configuration; if the tension If inside the cable is zero or the cable is slack, we can say that the cable doesn't contribute to this stiffness

2. We can assume that when we consider the contribution of this stiffness term from the vertical movement of the platform, the attaching point of The cable is moving in a

direction that is perpendicular to the direction of the cable, making an infinitesimal circumferential arc.

Because of the second assumption, and because for now we are not considering changes in the cable length, we can assume that the contribution of elastic stiffness to the total stiffness matrix is negligible.

4.6.1 Geometric stiffness

Geometric stiffness is the contribution that emerges from the effect of bending and spatial reconfiguration of the cable under load. It manifests itself as an increase in the cable's reactive tension in response to a displacement that changes the equilibrium geometry. In this simplified model, this stiffness is a function of the cable's linear submerged weight, depth, and horizontal tension, and is treated as a nonlinear but linearisable element for small displacements [19]. It is dominant in catenary configurations and can be calculated by derivative methods from analytical solutions. [42].

Contribution to the geometric stiffness from the vertical displacement

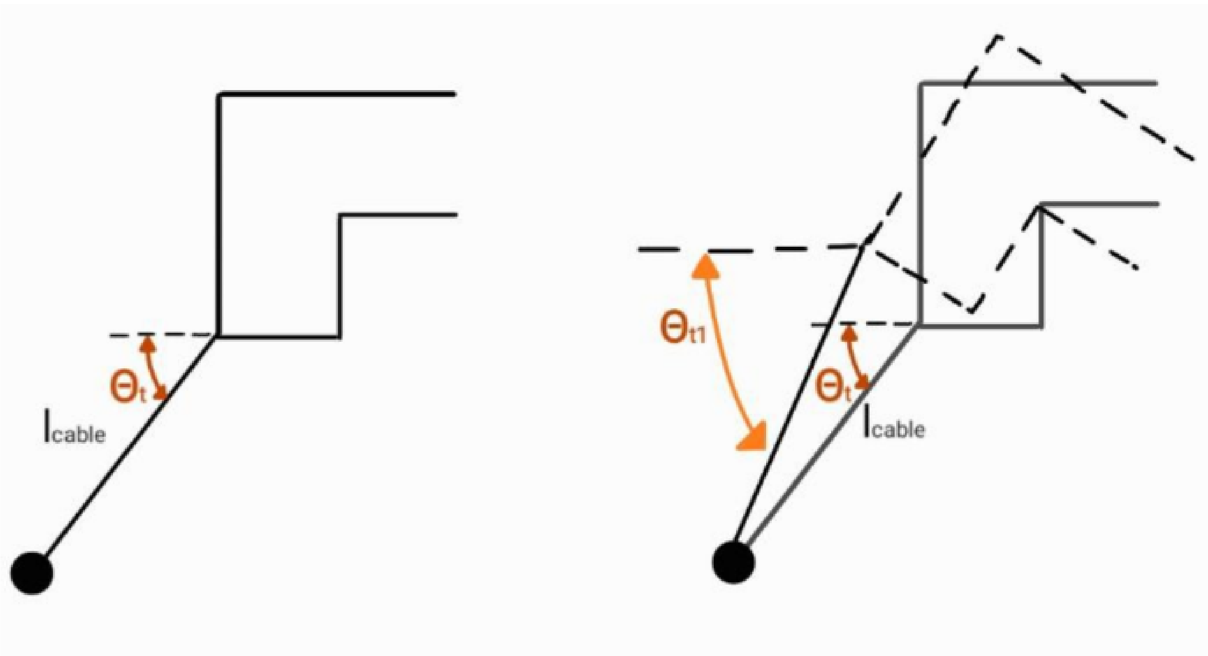

Figure 4.8: Infinitesimal angular movement of the platform

Where:

$$\delta\theta = \theta_{t1} - \theta_t \tag{4.23}$$

If we decompose the tension of the cable into its two components (along x and y), we can write the following equation. Then, by differentiating it with respect to the small displacement angle $\delta\theta$, we obtain:

$$\mathbf{F} = T \begin{bmatrix} \cos\theta_t \\ \sin\theta_t \end{bmatrix} \quad \Rightarrow \quad \frac{d\mathbf{F}}{d\delta\theta} = T \begin{bmatrix} -\sin\delta\theta \\ \cos\delta\theta \end{bmatrix} \tag{4.24}$$

Where T is the tension in the cable, assumed to be in a taut configuration.

Subsequently, we must determine a relationship between the angular variable $\delta\theta$ and the reference variable used in the state-space formulation. In this case, since we are evaluating the contribution with respect to the vertical displacement of the platform, the relevant variable is z:

$$\frac{d\mathbf{F}}{dz} = \frac{d\mathbf{F}}{d\delta\theta} \cdot \frac{d\delta\theta}{dz} \tag{4.25}$$

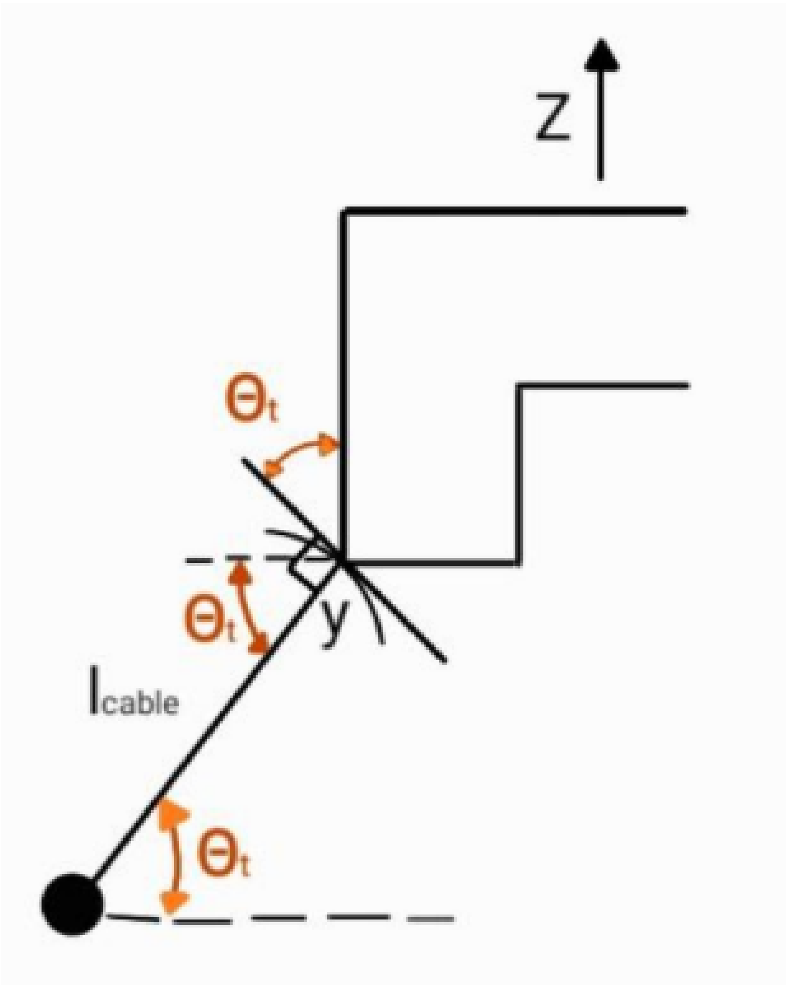

Figure 4.9: Contribution of the vertical displacement to the geometric stiffness

$$
\begin{aligned}
y &= \frac{z}{\cos\theta_t} \\
\Delta\delta\theta &= \frac{\Delta y}{l_{\text{cable}}} \\
\frac{d\delta\theta}{dz} &= \frac{d\delta\theta}{dy}\cdot\frac{dy}{dz} = \frac{1}{l_{\text{cable}}}\cdot\frac{1}{\cos\theta_t}
\end{aligned}
$$

So in the end, we can calculate the contribution of the vertical displacement to the geometric stiffness as:

$$
\frac{d\mathbf{F}}{dz} = \frac{T}{l_{\text{cable}}\cos\theta_t}\begin{Bmatrix} -\sin\delta\theta \\ \cos\delta\theta \end{Bmatrix} \tag{4.26}
$$

Contribution of Pitch to geometric stiffness

Following the same logic that we used for the calculation of the contribution to the vertical displacement, we can calculate the contribution to the geometric stiffness caused by the rotation along the x-axis.

Where l_{plat} is the distance between the centre of the platform and the point where the cable is attached to the platform, we can easily calculate

$$
\Delta z = l_{\text{plat}}\cdot\sin(\theta_x)\Delta z \approx l_{\text{plat}}\cdot\theta_x \quad \text{if } \theta_x \text{ is sufficiently small} \tag{4.27}
$$

From this equation, we can easily determine

$$
\frac{d\vec{F}}{d\theta_x} = \frac{d\vec{F}}{dz}\cdot\frac{dz}{d\theta_x} = \frac{T\cdot l_{\text{plat}}}{l_{\text{cable}}\cos\theta_t}\cdot\begin{Bmatrix} -\sin\theta_t \\ \cos\theta_t \end{Bmatrix} \tag{4.28}
$$

Now we can write the single term of the geometric stiffness for each cable

$$
k^g_{zz} = -\frac{T_i\cos\theta_t}{l_{\text{cable}}\cos\theta_t} \qquad [\text{N/m}] \tag{4.29}
$$

$$
k^g_{\theta\theta} = -\frac{T_i\, l^2_{\text{plat}}\cos\theta_t}{l_{\text{cable}}\cos\theta_t} \qquad [\text{Nm/rad}] \tag{4.30}
$$

$$
k^g_{\theta z} = k^g_{z\theta} = -\frac{T_i\, l_{\text{plat}}\cos\theta_t}{l_{\text{cable}}\cos\theta_t} \qquad [\text{N}] \tag{4.31}
$$

- T_i: Tension in the i-th taught mooring line [N]

- l_{cable}: Length of the mooring cable [m]
- l_{plat}: Horizontal distance from the center of the platform to the mooring line attachment point [m]

4.6.2 Buoyancy stiffness

Finally, the buoyancy stiffness is the contribution made by the variation of Archimedes' buoyancy as the platform moves. For a partially submerged body, each increment in sinking generates a change in the buoyancy force proportional to the derivative of the force with respect to the vertical displacement; so if we consider the displacement made by a vertical translation of the platform or by a rotation along the x-axis, we can write:

$$\Delta F_z = \rho_{\text{sea}}\, g\, A_{\text{platform}}\, \Delta z \tag{4.32}$$

So we can find the stiffness term related to a pure vertical translation:

$$k^b_{zz} = \frac{dF_z}{dz} = -\rho_{\text{sea}} g\, A_{\text{platform}} \tag{4.33}$$

where A_{platform} is the waterplane area of the platform.

The stiffness term related to a pure rotation along the X-axis can be found by considering that the buoyancy force is applied to a single column. Because we are considering two symmetric equal columns in this platform, we can write:

$$\Delta M^b = 2 \cdot \Delta F_z \cdot l_{\text{platform}} = 2 \cdot \rho_{\text{sea}} \cdot g \cdot A_{\text{column}} \cdot \Delta z \cdot l_{\text{platform}} \tag{4.34}$$

We can then find, by a simple geometric consideration, that

$$\Delta z = l_{\text{platform}} \cdot \theta_x \tag{4.35}$$

So we can rewrite the moment as:

$$\Delta M^b = 2 \cdot \rho_{\text{sea}} \cdot g \cdot A_{\text{column}} \cdot l^2_{\text{platform}} \cdot \theta_x \tag{4.36}$$

From this equation, we can easily determine the pure rotational term.

$$k^b_{\theta\theta} = \frac{dM^b}{d\theta_x} = -2 \cdot \rho_{\text{sea}} \cdot g \cdot A_{\text{column}} \cdot l^2_{\text{platform}} \tag{4.37}$$

In this case, if the platform makes a pure translation, we don't see a rotation. The cross-sectional term can be considered equal to zero.

$$k_{\theta z} = k_{z\theta} = 0 \tag{4.38}$$

In the end, the complete stiffness matrix of the system is made by the sum of each single term, and the form of the general matrix will be

$$K_{\text{tot}} = K^b + K^g \tag{4.39}$$

$$K_{\text{tot}} = \begin{bmatrix} k^{\text{tot}}_{\theta\theta} & k^{\text{tot}}_{\theta z} \\ k^{\text{tot}}_{z\theta} & k^{\text{tot}}_{zz} \end{bmatrix} \tag{4.40}$$

It has been seen in the calculation that the buoyancy terms of the stiffness matrices are, for all the bins considered, usually 3-4 times bigger than geometric terms. This is perfectly coherent with the assumptions made in this model. Taking into consideration the way we build our matrices, the buoyancy term takes into account all the weight of the platform, while at the same time, the geometric terms only consider the thrust force in the cables made by the wind.

4.7 Inertia Matrix

The matrix of inertia is made by the sum of two different terms; one is m_{platform}, which is related to the total mass and inertia of the system, and the other is related to the inertia of the cable m_{cable}. The first term of the matrix is the result of how the platform is made, and we can take all the data that we need from the previous chapter. In order to determine how the second term is made, we have to make the same assumption that we made in order to write the geometry stiffness term. So, if we imagine that the platform is moving in a perpendicular direction to the direction of the cable itself, we can calculate the moment of the down force as follows:

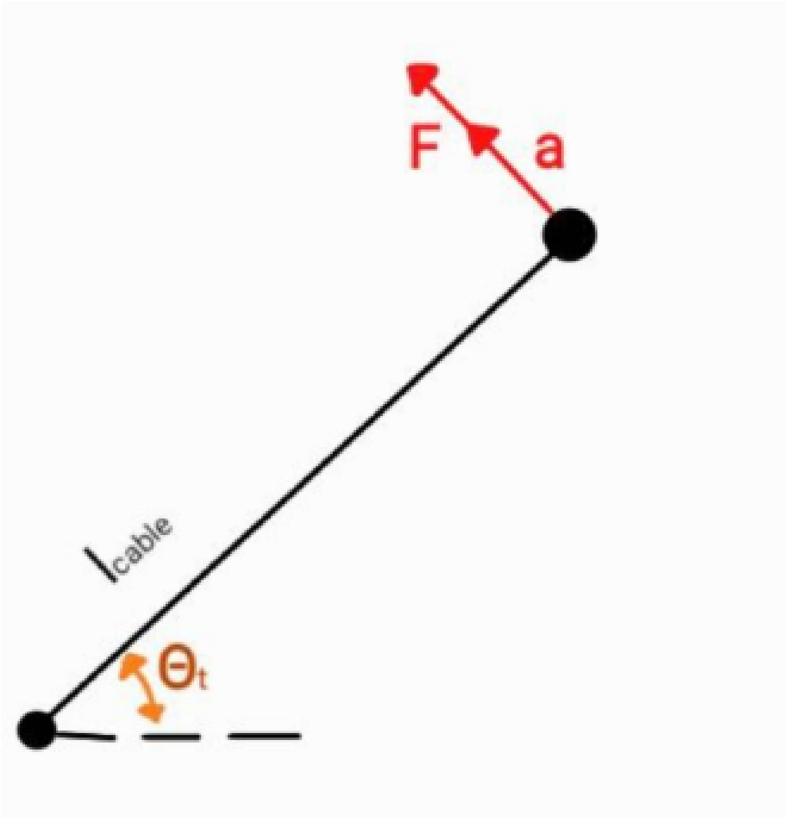

Figure 4.10: Force moment

$$F \cdot l_{\text{cable}} = \frac{I \cdot a}{l_{\text{cable}}} \qquad [\text{N}\cdot\text{m}] \tag{4.41}$$

Where:

$$I = \frac{1}{3}\,\rho_{\text{cable}}\,l_{\text{cable}}^{3} \qquad [\text{kg}\cdot\text{m}^{2}] \tag{4.42}$$

- ρ_{cable} = Density per unit length of the cable [Kg/m]
- l_{cable} = Length of the cable [m]

We can then rewrite the formula of the force as follows:

$$F = \frac{\rho_{\text{cable}}\,l_{\text{cable}} \cdot a}{3} \tag{4.43}$$

- a = Acceleration of the platform [m/s^2]

From there, we can then calculate the mass of the cable by deriving the force for the acceleration and dividing by the cosine of the angle theta taut, following the same assumption made for the stiffness term, as follows:

$$m_{\text{cable}} = \frac{dF}{da} = \frac{\rho\, l_{\text{cable}}}{3} \tag{4.44}$$

$$m_{\text{cable}} = \frac{\rho\, l_{\text{cable}}}{3\cos\theta_t} \tag{4.45}$$

From there, we can then find, in the same way as done for the stiffness matrix, all the terms where l_{plat} is the distance between the centre of mass of the platform and the point where the cable is attached:

$$\mathbf{m}_{\text{cable}} = \frac{\rho\, l_{\text{cable}}}{3\cos\theta_t}\begin{bmatrix} 1 & l_{\text{plat}} \\ l_{\text{plat}} & l_{\text{plat}}^2 \end{bmatrix} \tag{4.46}$$

knowing that the $matrix_{plat}$ can be written as:

$$\text{matrix}_{\text{plat}} = \begin{bmatrix} m_{\text{plat}} & 0 \\ 0 & I_{\text{xxplat}} \end{bmatrix} \tag{4.47}$$

In the end, we can write all the matrices as

$$\mathbf{M}_{\text{tot}} = \mathbf{matrix}_{\text{plat}} + \mathbf{m}_{\text{cable}} \tag{4.48}$$

4.8 Damping Matrix

The damping matrix is composed of three terms: one is related to the wind force that hits the rotor, one term is related to the drag force of the cable when it moves under the water, and the last term is related to the damping ratio.

Rotor damping term

In order to determine the first term c_{rotor}, we have to consider the lateral movement made by the rotor when it is hit by the wind force.

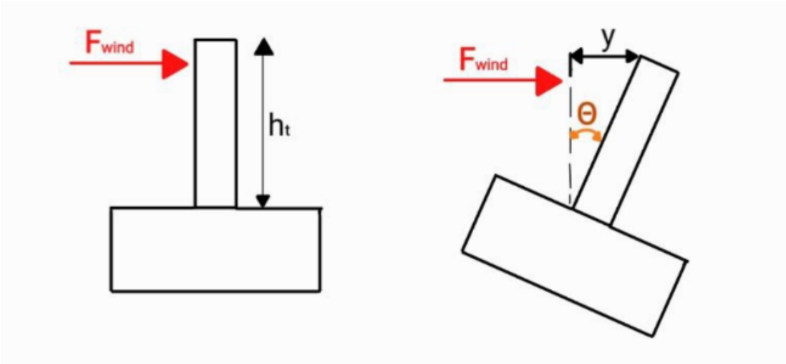

Figure 4.11: rotor damping term

From there, we can write in this way the force

$$F = \frac{1}{2}\,\rho_{\text{air}}\,A_{\text{rot}}\,C_T\,\left(v_\infty - v_T\right)^2 \tag{4.49}$$

Where:

- $v_T = h \cdot \dot{\delta\theta}$ is the velocity of the rotor when impacted by the wind [m/s]
- v_∞ is the free-stream wind velocity [m/s]
- C_T is the thrust coefficient of the rotor [–]

Now, if we make the derivation of the F by $\dot{\theta}$, we can write:

$$\frac{dF}{d\dot{\delta\theta}} = \frac{1}{2}\,\rho_{\text{air}}\,A_{\text{rot}}\,C_T\,\left(-2v_\infty h + 2h^2\dot{\delta\theta}\right) \tag{4.50}$$

if we now consider the equilibrium situation where $\dot{\delta\theta} = 0$

We can simplify the term and write:

$$c_{\text{rotor}} = \frac{dF}{d\dot{\delta\theta}} = -\rho_{\text{air}}\,A_{\text{rot}}\,C_T\,V_\infty\,h \tag{4.51}$$

Cable damping term

For the damping term related to the cable, we have to consider, as already explained, the movement of the cable in a direction perpendicular to that of the cable direction and consider the drag force resulting from that movement.

$$F_{\text{drag, l}} = \frac{1}{2}\,\rho_{\text{sea}}\,C_D\,v^2 \tag{4.52}$$

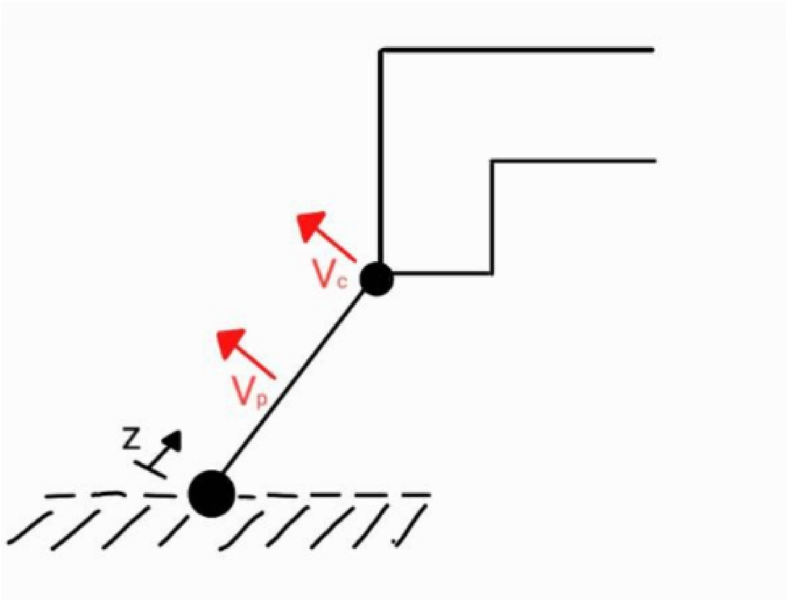

Figure 4.12: Cable damping term

$$\text{where } v = \frac{v_c}{l_{\text{cable}}} \quad \text{is the generic velocity of a single point of the cable} \tag{4.53}$$

When can we now integrate along the entire length of the cable and find out

$$F_{\text{drag}} = \int_0^{l_{\text{cable}}} \frac{1}{2}\,\rho_{\text{sea}}\,C_D\,\frac{V_c^2\,z^2}{l_{\text{cable}}^2}\,dz F_{\text{drag}} = \frac{1}{6}\,\rho_{\text{sea}}\,C_D\,v_c^2\,l_{\text{cable}} \tag{4.54}$$

We now have to assume the type of flow that we are considering. To do that, we first have to calculate the Reynolds number, and from there, with an empirical formula, we can calculate the right drag coefficient. so from

$$\text{Re} = \frac{\rho_{\text{sea}}\,D_{\text{cable}}\,v}{\mu} \approx 10\text{–}100$$

$$\text{from which we find that} \quad C_D = 1.5$$

If we then derive the equation from the variable v_c. We can write that

$$\frac{dF}{dv_c} = \frac{1}{3}\,\rho_{\text{sea}}\,C_D\,V_c\,l_{\text{cable}} \tag{4.55}$$

But if we now consider an equilibrium situation where $v_c = 0$

We can write

$$\frac{dF}{dv_c} = 0 \tag{4.56}$$

so $c_{cable} = 0$

Rayleigh Damping term

The third term is calculated starting from the definition of compression ratio (δ), in a 1DOf model, because it's a very useful parameter in order to determine whether the system is isolated ($\delta < 1$)or not. Defined as:

$$\delta = \frac{C}{2\sqrt{KM}} \tag{4.57}$$

The damping matrix in the Rayleigh model is given by:

$$C_{\text{Rayleigh}} = \alpha\,[M] + \beta\,[K] \tag{4.58}$$

If we assume that the proportionality coefficients are equal, i.e., $\alpha = \beta$, the expression simplifies to:

$$C_{\text{Rayleigh}} = \alpha\,[M + K] \tag{4.59}$$

If we then assume that the platform itself has a $\delta = 0.4$ We have to find the right value of α, so we can use this formula.

$$\delta = \frac{\alpha\,[M + K]}{2\sqrt{KM}} \tag{4.60}$$

In our model, because we have a 2Dof system and [M]and [K] are matrices, we cannot invert this formula; otherwise, we will have a problem of consistency. We make an assumption and calculate the Rayleigh term as follows:

$$c_{\text{Rayleigh}} = \frac{\delta}{2}\,[K_{\text{tot}} + M_{\text{plat}}] \tag{4.61}$$

And we can now find the damping matrix as

$$C_{\text{tot}} = c_{\text{rotor}} + c_{\text{cable}} + c_{\text{Rayleigh}} \tag{4.62}$$

So now, given all the considerations, we can write the following generalized equation for our model in a condition of static equilibrium:

$$[M]\{\ddot{q}\} + [C]\{\dot{q}\} + [K]\{q\} = 0 \tag{4.63}$$

- $[M]$ = Global inertia matrix
- $[C]$ = Global damping matrix
- $[K]$ = Global stiffness matrix

where the global vector of the degrees of freedom is defined as:

$$\{q(t)\} = \begin{bmatrix} z(t) \\ \theta(t) \end{bmatrix} \tag{4.64}$$

4.8.1 State-Space system

Once the mass matrix $\mathbf{M}$, the damping matrix $\mathbf{C}$, and the stiffness matrix $\mathbf{K}$ were defined, and the degrees of freedom of the system were identified through the generalised state vector $\mathbf{q} = \begin{bmatrix} z \\ \theta \end{bmatrix}$, the system was reformulated in the state-space form to allow for numerical integration and control implementation. As already explained in Chapter 2 and in Appendix B, here we are only going to report the generic calculation of the state-space system, knowing that this can be extended to all the matrices calculated for each bin taken into consideration. The complete state vector was defined as:

$$\mathbf{x} = \begin{bmatrix} \dot{z} \\ \dot{\theta} \\ z \\ \theta \end{bmatrix} \tag{4.65}$$

The system matrix $\mathbf{A}$ was constructed in the canonical second-order form as:

$$\mathbf{A} = \begin{bmatrix} -\mathbf{M}^{-1}\mathbf{C} & -\mathbf{M}^{-1}\mathbf{K} \\ \mathbf{I} & \mathbf{0} \end{bmatrix} \tag{4.66}$$

The input matrix for environmental forcing is:

$$\mathbf{B}_{\text{force}} = \begin{bmatrix} \mathbf{M}^{-1} \\ \mathbf{0} \end{bmatrix} \tag{4.67}$$

The matrix $\mathbf{B}_t$ represents the direction and lever arm contributions of the two active cables in the taut configuration, and is defined as:

$$\mathbf{B}_t = \begin{bmatrix} \sin(\theta_{\text{taut}}) & \sin(\theta_{\text{taut}}) \\ l_{\text{plat}} \cdot \cos(\theta_{\text{taut}}) & -l_{\text{plat}} \cdot \cos(\theta_{\text{taut}}) \end{bmatrix} \tag{4.68}$$

Based on this, the control input matrix for the state-space system is:

$$\mathbf{B}_{\text{control}} = \begin{bmatrix} \mathbf{B}_{\text{force}} \cdot \mathbf{B}_t \\ \mathbf{0}_{2\times2} \end{bmatrix} \tag{4.69}$$

Where $\mathbf{B}_{\text{force}}$ is the input matrix mapping control forces to accelerations, and $\mathbf{0}_{2\times2}$ is a null matrix that ensures the correct dimensionality in the augmented state-space formulation.

The open-loop input matrix $\mathbf{B}_{\text{open-loop}}$ is defined to represent the uncontrolled system, where only the external environmental forces act on the platform. It is structured as:

$$\mathbf{B}_{\text{open-loop}} = \begin{bmatrix} \mathbf{B}_{\text{force}} \\ \mathbf{0}_{2\times2} \end{bmatrix} \tag{4.70}$$

Here, $\mathbf{B}_{\text{force}}$ maps external forces to the acceleration states, while the zero matrix $\mathbf{0}_{2\times2}$ accounts for the absence of direct input on the displacement states in the state-space formulation.

The output matrices were set as:

$$\mathbf{C} = \mathbf{I}, \quad \mathbf{D} = \mathbf{0} \tag{4.71}$$

This state-space formalism enables the numerical integration of the equations of motion and the simulation of the system's dynamic response to both external disturbances and active control actions.

Chapter 5

Benchmarking Against Published Studies

After the complete development of the dynamic model and its implementation in a simulation environment that reflects realistic operating conditions, it was necessary to assess the reliability and representativeness of the model both in terms of the physical assumptions adopted and the simplifications introduced during the modeling phase. The aim of this validation phase was not to achieve a quantitative match with the reference data from fully detailed high-fidelity models, such as those presented in the paper used for the validation, but rather to verify the consistency and coherence of the underlying mechanical logic and control architecture. Given the preliminary nature of this study, the model incorporates significant simplifications, including reduced degrees of freedom, idealized mooring line behavior, and lumped parameter approximations. Despite these assumptions, the objective was to evaluate whether the main dynamical trends qualitatively reflected those observed in more advanced numerical frameworks. This validation step was essential to justify the use of the simplified model in the subsequent active control design phase, ensuring that the key dynamic couplings and feedback paths were correctly captured and could support meaningful controller synthesis and performance analysis.

Due to the limited time available for the realisation of the present work, it was decided to focus the model validation activity exclusively on the pitch degree of freedom. This choice is motivated by the fact that pitch represents, in floating offshore wind applications, the most critical degree of freedom in terms of dynamic stability, as well as the one that manifests the greatest variability under the combined action of wind, waves, and current. Consequently, it is also the degree of freedom that needs targeted validation more than others, as it strongly influences the overall system response and the estimation of structural loads.

For similar reasons of time, the validation was carried out on the basis of two selected studies in the literature, each relating to a specific operating condition. Although limited in number, these scenarios were chosen to be sufficiently representative of the range of conditions that the system may reasonably be expected to encounter in operation.

Although it is recognised that a complete validation would require the extension of the analysis to all degrees of freedom and to a larger number of cases, it is believed that the verifications carried out constitute a methodologically sound basis for considering the model developed reliable even in its components that have not been directly validated, at least in terms of qualitative consistency and order of magnitude of the simulated responses.

5.1 Verification of Physical Consistency through Free Decay Tests

Numerous simplifications were adopted in the construction of the model. For example, it was assumed that the platform, despite its size and considerable weight, does not affect the wave in any way at the moment of impact. In reality, as is known in the literature, such interaction exists and is not negligible. In more advanced academic work, `WAMIT` software is frequently used to accurately simulate the interaction between the platform and the wave field, while in the present work, a simplified approach of a statistical nature was used, based on the spectral theory of JONSWAP (see chapter 2 and Appendix A for a more detailed explanation of the method used).

The dynamic model adopted is also extremely simplified, being limited to only two degrees of freedom. The mooring cables have been modelled as rigid elements, assuming that they instantaneously follow the motion of the platform. In reality, the cables possess their intrinsic dynamics and do not move rigidly with the floating structure. Furthermore, it was assumed that in static conditions, i.e., with a perfectly still and stable platform, the cables also remain still. This assumption is idealised: in the real case, the cables, subject to non-linear behaviour, always exhibit a certain dynamic, even under apparently static platform conditions.

In order to empirically account for these simplifications, corrective factors were introduced on the stiffness matrix and the damping coefficient in order to obtain a dynamic response compatible with that of the reference model.

To verify whether the physical approximations adopted in the construction of the model were justified, the free-decay response in pitch reported in the *IEA Wind TCP Task 37* paper was reproduced as faithfully as possible. This IEA study considers the same floating wind platform and turbine used in this paper. Therefore, being able to exactly replicate the free-decay response of the system, obtained from an initial impulse of 10° in pitch, is a significant indication of the correctness and consistency of the approximations adopted.[5]

The first aspect to be verified was that the model had the same equivalent mass and global stiffness as the reference system, which translates into the superposition of the periods of the oscillations, i.e., that the time between two consecutive peaks in the two graphs was the same. This parameter is directly related to the natural frequency of the system, according to the well-known relationship:

$$f = \frac{1}{2\pi}\sqrt{\frac{k}{m}} \tag{5.1}$$

Since the mass matrix of the system was faithfully derived from the data of the reference report, and since the mass and geometry of the platform were accurately replicated, it can be reasonably assumed that any discrepancies between the periods of the two graphs are attributable to stiffness.

To obtain a period coincident with that of the reference system, a correction factor was introduced on the stiffness equal to:

$$k_{factor} = 0.36$$

Which is equivalent to reducing the stiffness of the modelled system by 64%. This correction is consistent with the simplifications described above and justifiable since the present work is highly preliminary in nature.

As far as damping is concerned, the parameter ζ was adjusted so that the amplitude decay rate over time was identical in the two models, i.e., the time required for the pitch amplitude to halve was the same. The value used:

$$\zeta = 0.03$$

It was chosen so that the exponential envelope of the decay would overlap. According to the following relationship:

$$\zeta = \frac{1}{\sqrt{1 + \left(\frac{\pi}{\ln\left(\frac{x_1}{x_2}\right)}\right)^2}} \tag{5.2}$$

Where x_1 and x_2 are two consecutive peaks, it can be verified that the damping coefficient thus chosen produces a decay consistent with that of the reference model.

Based on these considerations, it is considered that the correction coefficients introduced on stiffness and damping are physically plausible and justified, and that the dynamics of the simplified model are in agreement with those of the reference system used in the *IEA Wind TCP Task 37* paper. Consequently, the physical modelling employed can be considered consistent with the assumptions made and appropriate for the level of detail of the present study. [5]

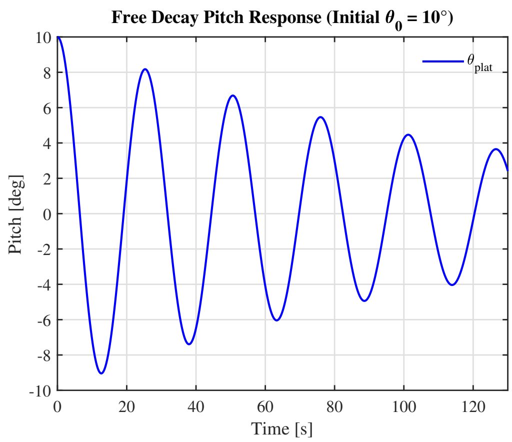

(a) free decay response of our model

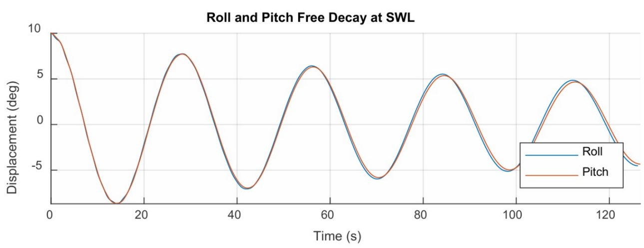

(b) free decay pitch response [1]

Figure 5.1: validation of the physics of the model

[1]Source: [5]

5.2 Dynamic Validation in Operational Scenarios

This section describes the procedure adopted to verify the dynamic model developed, through the simulation of the system's behaviour in a realistic environmental context. In particular, the temporal evolution of the pitch angle of the wind platform was observed, comparing the results obtained with those presented in the report *2024 – Dynamic Analysis of a 10 MW Floating Offshore Wind Turbine Considering the Tower and Platform Flexibility*[16].

In the reference work, a different model is adopted from the one used in this thesis: specifically, the turbine considered is the DTU 10 MW Reference Wind Turbine, installed on a floating platform of the Triple Spar type. In order to reproduce as faithfully as possible the conditions simulated in the paper, it was decided to replace, within my model, the data relating to the 15 MW IEA turbine previously adopted with those corresponding to the 10 MW turbine. On the other hand, the platform remained unchanged: the model inspired by the VolturnUS-S developed by the University of Maine, which forms the basis of the IEA reference platform, was retained.

These differences are compounded by the simplifications already discussed in the previous section. For this reason, a perfect overlap between the simulation results conducted and those reported in the comparison work is not expected. Instead, the main purpose of the verification is to obtain qualitatively consistent trends, particularly in the pitch angle dynamics, with peaks of comparable amplitude to those of the validated model, while taking into account the inevitable numerical discrepancies.

The model presented in *Dynamic Analysis of a 10 MW Floating Offshore Wind Turbine Considering the Tower and Platform Flexibility* was tested under two distinct load conditions:[16]

- **LC1 (Load Case 1)**: standard operating condition, characterised by a wind speed $W_s = 2.9$ of 10.1 m/s, a significant wave height $H_s = 2.9$ m, a turbulence level $I = 0.14$, and a spectral parameter $\gamma = 3.3$.

- **LC2 (Load Case 2)**: extreme weather and sea conditions, with wind speed of 37.5 m/s and significant wave height of 9.5 m.

In the context of this thesis, the simulation was limited to the LC1 condition only. The main reason is that the implemented model is not suitable for reproducing the extreme conditions described by LC2. Specifically, the aerodynamic coefficient $C_{T,\text{wind}}$ was calculated as:

$$C_{T,\text{wind}} = \frac{P}{W_s}$$

Where P is the Power (MW) of the turbine, and W_s is the wind speed considered.

This formulation is only approximately valid when the wind force can be idealised as a concentrated thrust force, which is valid for standard operating regimes with moderate wind and current. Under extreme conditions, this approximation loses validity. In addition, when the system is subjected to such high wind speeds, the turbine automatically enters emergency mode (shut-down), and the blades are then oriented out of the wind by pitching, cancelling the aerodynamic thrust, and the rotor's contribution is decoupled from the platform dynamics.

The model proposed in this thesis, being highly simplified, cannot reproduce such operational transitions, nor accurately model the pitch and emergency shut-down control mechanisms. For this reason, the LC2 condition is excluded from the analysis, focusing only on behaviour in the operational regime (LC1) or transient events of an exceptional nature.

An exception is the simulation of the extreme gust (Extreme Operating Gust – EOG), an event of short duration and low probability (return time 40 years). In this case, the phenomenon occurs in such a short time interval that the system does not have the physical time to activate the shut-down, and the dynamics of the platform can still be studied with the developed model, maintaining validity in the very first moments of the transient.

A further consideration concerns the three structural configurations investigated in the comparison work. In *Dynamic Analysis of a 10 MW Floating Offshore Wind Turbine Considering the Tower and Platform Flexibility* , the simulation is conducted in three different scenarios: [16]

- fully rigid structure (platform, tower, blades)
- fully flexible structure
- structure with rigid platform and flexible upper part (tower and blades)

In the present work, as this is a preliminary analysis based on a simplified model, only the case of the fully rigid structure was considered. This choice is motivated by the fact that no deformable elements were included in the implemented model, and no degree of flexibility was provided for the tower and blades.

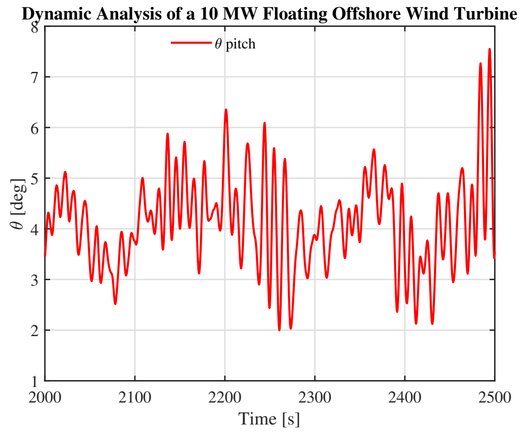

(a) Pitch response of the model under LC1 conditions

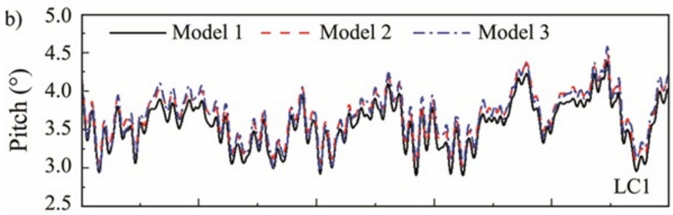

(b) Response under LC1 conditions [2]

Figure 5.2: Model validation in a realistic environment

Analysing the results from the comparison between the two graphs, it can be seen that my model shows greater variability and a wider range of oscillations, with peaks exceeding 8 degrees, compared to a maximum value of 4.6 degrees in the reference model.

As further highlighted, the oscillations shown in the paper's graph are more contained and develop in a range between 2.9° and 4.6°, while in my case, they extend from 1.9° up to around 8°. This results in a more pronounced and locally more unstable dynamic behaviour, sometimes described as "nervous". Furthermore, when looking at the frequency of oscillations, one notices that my model exhibits slightly more frequent oscillations, a sign of a possibly more reactive dynamic response or less effective damping.

Despite these quantitative differences, from a qualitative point of view, the two graphs show similar trends. This allows us to state that, taking into account the simplifications

[2]Source:[16]

adopted in the construction of my model, the overall dynamic behaviour is consistent with that observed in the reference model. Consequently, it can be considered that my model, despite its simplicity, is sufficiently validated in qualitative terms. This validation allows us to assume that the results obtained through the post-processing of my model - in particular those relating to the use of different control strategies - are consistent, coherent, and reliable. In fact, despite being based on a simplified model, these results derive from a dynamic structure that shows good qualitative correspondence to far more complex and established models in the academic literature [16]

Chapter 6

Control Tuning and Results Discussion

In the next chapter, we are going to describe in detail the choices that have been made to tune the model, and we are going to present all the results obtained. As already explained in detail in chapter 2, we chose for tuning the model three different sets of poles, each of which occupies a specific position in the **??**, as also shown in the graph below. The reason why we chose these three different sets of poles is to replicate three different types of tuning, which aim to provide the reader with a complete overview of the effects that the implemented control system has on the platform. (Please refer to the specific section in chapter two for further details.) Below, we present the sets of poles chosen to tune the control system.

1. Light control

The first set of poles chosen, denoted as

$$p_{\text{light}} = \begin{bmatrix} -0.0236 + 0.233\text{i} & -0.0236 - 0.233\text{i} & -0.0669 + 0.666\text{i} & -0.0669 - 0.666\text{i} \end{bmatrix}$$

It is characterised by a real part very close to zero (respectively -0.0236 and -0.0669) and a relatively high imaginary part (respectively $\omega_d = 0.233$ and $\omega_d = 0.666$). These values indicate weakly damped dynamics with persistent oscillations and slow time decay. The controller gains are modest, and the dynamic stability of the system is precarious.

2. Frequency-aggressive control

In the second scenario, identified with

$$p_{\text{freq}} = \begin{bmatrix} -0.330 + 0.331\text{i} & -0.330 - 0.331\text{i} & -0.937 + 0.942\text{i} & -0.937 - 0.942\text{i} \end{bmatrix}$$

The poles were placed with a significantly more negative real part (respectively -0.330 and -0.937) and imaginary frequencies deliberately deviated from the natural frequencies of the open-loop system, calculated to be $f_1 = 0.0356$ Hz and $f_2 = 0.1061$ Hz. This choice allows for a fast dynamic response, increasing the rate of oscillation attenuation and reducing the risk of resonance with prevailing wave spectral components. The cost of this strategy is the potential risks of numerical instability if the poles are positioned too far from the imaginary axis.

3. Damping-aggressive control

The third set of poles,

$$p_{\text{damp}} = \begin{bmatrix} -0.212 + 0.073\text{i} & -0.212 - 0.073\text{i} & -0.603 + 0.207\text{i} & -0.603 - 0.207\text{i} \end{bmatrix}$$

has a sufficiently negative real part (respectively -0.212 and -0.603), associated with significantly reduced imaginary frequencies ($\omega_d = 0.073$ and $\omega_d = 0.207$). This configuration is aimed at minimising oscillating amplitudes, with a more pronounced effect on damping than on response speed. This strategy is particularly effective for reducing acceleration at the top of the tower or cyclic loads on the structure.

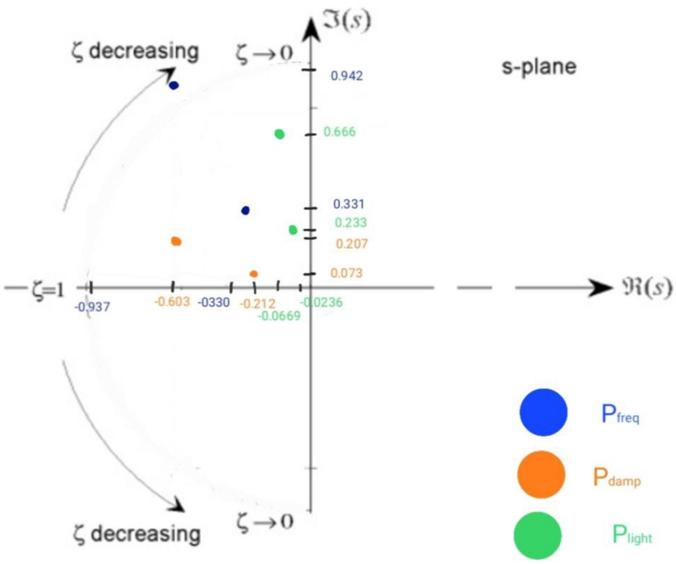

Figure 6.1: Position of the Poles

For clarity, the figure above shows only the poles with positive imaginary parts, although we are aware that these are complex conjugate poles and that each of them therefore has its own symmetrical counterpart with respect to the real axis.

6.1 Results Discussion

6.1.1 Quantitative Analysis of Key Dynamic Parameters

In this second section of the chapter, we will proceed with the quantitative analysis of four key parameters related to the dynamic response of the system studied. In particular, the following will be evaluated:

- the acceleration at the top of the tower (tower-top acceleration),
- the maximum pitch value reached by the platform following a sudden gust of wind (gust),
- the amount of fatigue damage suffered by the mooring cables,
- the energy absorbed by the active control system during operation.

For the evaluation of tower-top acceleration, cable fatigue, and energy consumption, the concept of expected time-averaged load is adopted, in accordance with what is detailed in the apposite section in Chapter Two and in Appendix A. This value is determined by calculating the weighted average of the parameter of interest (acceleration, energy, or fatigue) over a discretisation of the environmental space into bins, each characterised by its own probability of occurrence. The expected value is obtained by multiplying the value of the parameter in the centre of each bin by its respective probability of occurrence, and summing the resulting contributions. This methodology makes it possible to estimate a synthetic indicator representative of the average operating conditions of the system. As for the analysis of the maximum pitch induced by a wind gust, this is a transient event of an extreme type, which cannot be associated with long-term statistics. Consequently, we proceeded with the simulation of a single representative event, applying the Extreme Operating Gust (EOG) theory to a central bin of the environmental domain, in order to estimate the plausible maximum response of the platform. For further details regarding the implementation of the EOG model, please refer to the specific section in Chapter Two and in Appendix A. These quantities will be analysed for all the configurations modelled, i.e., the open-loop system and the three active control scenarios defined above: light control, frequency-aggressive, and damping-aggressive.

It is important to understand that, in light of the simplifying hypotheses adopted in the development of the dynamic model, the results will only be expressed in relative terms, i.e., as percentage variations with respect to the uncontrolled reference case (open-loop). This methodological choice is necessary in order to free the interpretation of the results from the specific complexity of the model adopted: both open-loop and closed-loop configurations share the same structural and environmental assumptions, so the relative comparison allows us to extrapolate general considerations that are also valid in more sophisticated modelling contexts. In other words, the percentage analysis makes it possible to assume that the effectiveness of the designed control system, measured as a relative change with respect to the open-loop, remains of the same order of magnitude even if the system is implemented in high-fidelity models, where the absolute values of the quantities under analysis may be substantially different. The use of normalised indices, therefore, makes it possible to focus attention on the incremental (or decremental) effect introduced by the control, isolating it from the structural specificities of the model adopted here.

In the following section, the results obtained for each configuration will therefore be presented and discussed, analysing the behaviour of the four selected parameters in terms of percentage variation concerning the uncontrolled system.

Tower Top acceleration

The first parameter examined is the tower-top acceleration, analysed in relation to the different control scenarios implemented, and evaluated in relative terms concerning the open-loop reference configuration.

For the determination of the tower-top acceleration, it was assumed that the system operates in a regime of *small oscillations*, assuming that the angular velocity (rotation rate) of the rigid body is sufficiently contained. This assumption allows us to linearise the kinematics and treat the motion of the tower top as a combination of the vertical translation z and the rotation around the transverse axis θ.

The instantaneous position of the point at the top of the tower is then modelled as the vector:

$$\vec{p}_{\text{top}}(t) = \begin{bmatrix} h_{\text{t}} \cdot \theta(t) \\ z(t) \end{bmatrix} \tag{6.1}$$

By deriving twice with respect to time, the expression of the acceleration is obtained:

$$\vec{a}(t) = \begin{bmatrix} h_{\text{t}} \cdot \ddot{\theta}(t) \\ \ddot{z}(t) \end{bmatrix} \tag{6.2}$$

Based on this formulation, it was possible to simulate the time behaviour of the acceleration for the various control strategies implemented. The following figure shows the time course of tower-top acceleration for the four scenarios: *open-loop*, *light control*, *frequency-aggressive control*, and *damping-aggressive control*.

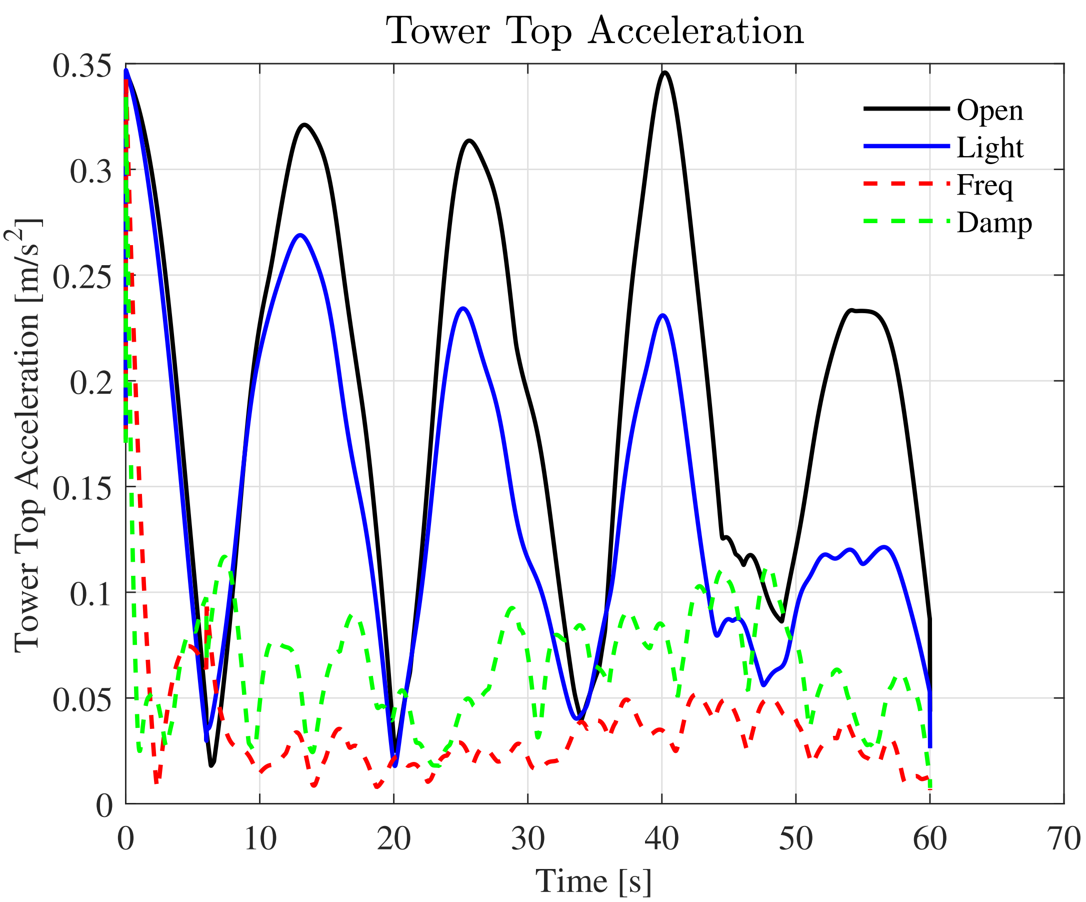

Figure 6.2: Tower Top acceleration

Subsequently, the results were processed in tabular form, expressing the relative reductions compared to the open-loop in terms of max, mean, standard deviation, and range of acceleration.

Table 6.1: Percentage reduction in tower-top acceleration metrics for each control strategy (relative to open-loop configuration).

Control Strategy	**Max** [%]	**Mean** [%]	**Range** [%]	**Std** [%]
Light Control	−22.244	−29.499	−21.738	−22.784
Freq Control	−85.058	−85.555	−85.899	−87.325
Damp Control	−67.422	−67.209	−67.213	−72.728

As the results show, all implemented active controllers contribute significantly to acceleration reduction, although with varying effectiveness. In particular:

- **Light control** achieves an average reduction of around 20%.
- **Damping-aggressive control** achieves an average reduction in the order of 65–67%, proving effective while being close to the critical damping condition ($\zeta \approx 0.95$).
- **Frequency-aggressive control** provides the best performance, with an average reduction of 85–90%, thanks to an optimal damping ratio ($\zeta \approx 0.7$).

The observed reductions in mean, standard deviation, and range of acceleration are consistent and comparable, indicating that the control system not only limits the intensity of the motion but also effectively dampens variations around the mean value, confirming good control robustness.

From an engineering point of view, the reduction of tower-top acceleration has direct repercussions on numerous design and performance aspects of the floating turbine:

- it allows structural optimisation of the tower, reducing its masses and design bending moments;
- improves the stability of the mooring cables, reducing transmitted dynamic loads;
- mitigates structural fatigue effects;
- contributes to improving the quality of the electrical power generated;
- reduces the dynamic load on the drivetrain, increasing its service life and reducing the probability of mechanical failure.

Overall, the results obtained are fully in line with the theoretical predictions made during the controller design phase, and demonstrate the effectiveness of the active control strategy in improving the dynamic behaviour of the system with respect to a key parameter such as acceleration at the top of the tower.

Numerous technical studies in the literature have highlighted how high values of tower-top acceleration can have significant structural implications for the design of floating platforms, directly influencing both the overall stability of the system and the size and structural mass of the tower.

In particular, the *Design of Platform 2020* report emphasises that, in order to contain the bending moment at the base of the tower and to avoid the risk of resonant coupling with the 3P frequency of the rotor, it was necessary to increase the mass of the flexible tower by 47% compared to a rigid monopile configuration. This increase was adopted precisely to move the natural frequency of the system away from resonant zones, which are amplified in the presence of strong dynamic accelerations.

The same report also shows that under highly turbulent wind conditions, there is a direct correlation between the increase in tower-top acceleration and the increase in bending moment at the base of the tower, thus aggravating the fatigue stresses and structural requirements of the tower itself.

This evidence is further confirmed by the work of Gao et al. [16], *Dynamic Analysis of a 10 MW Floating Offshore Wind Turbine Considering the Tower and Platform Flexibility*, where it is shown how the increase in model flexibility leads to increasing values of the accelerations and moments transmitted to the base of the tower.

In particular, with respect to the reference model, the increase in bending moment is +7% for Model 2 and +13% for Model 3, testifying to the fact that structurally more flexible models subject to greater accelerations can lead to more severe operating conditions for the structural elements of the tower.

Furthermore, the paper 'design of platform 2024' also explicitly states that the rotor's momentum, and thus its acceleration, is one of the most important aspects for a wind turbine, since it can directly affect the durability and survival of the turbine, as well as the fact that high accelerations lead to a significant decrease in the quality of the energy produced, a thesis that is further confirmed by the report 'The impact of platform motion on the aerodynamic characteristics of floating offshore wind turbine arrays' in so far as it argues that a key element for the aerodynamic performance of the structure is precisely the fluctuation of the nancell, saying that the less this movement, the higher the quality of the power produced. All these results show that the control system implemented in this thesis could contribute significantly to the performance of the turbine, making it possible to increase the quality of the energy produced and increase its fatigue life, while at the same time reducing the bending moment acting on the tower. [19]

Maximum pitch from a wind Gust

Similarly to what has been carried out for the analysis of the acceleration at the top of the tower, we now proceed with the study of the dynamic response of the system to an occasional extreme event, specifically a gust event characterised by a low probability of occurrence and significant intensity. According to the normative guidelines (IEC 61400-1), events of this type are associated by design with a return time of 40 years, and their correct simulation constitutes a fundamental aspect for the structural validation of floating platforms.

For this type of event, the most important dynamic parameter is the maximum pitch angle reached by the platform. In fact, if the pitch value is too high, this can lead to serious stability problems and compromise the structural integrity of the turbine-platform system and, at the same time, can violate the limits imposed by international safety regulations. Because of the fact that the gust is by nature an impulsive, localised, and non-stationary event, it was not simulated over all environmental bins as in the case of weighted time averages. Instead, a representative bin of the operational domain was selected to reproduce a typical condition. For further details regarding the gust profile generation procedure and EOG implementation, please refer to the specific section and the dedicated Appendix A. [1] We have extracted the maximum pitch from the simulation in all the cases considered in the previous section. Below is the time course of the pitch response to the gust for each control configuration:

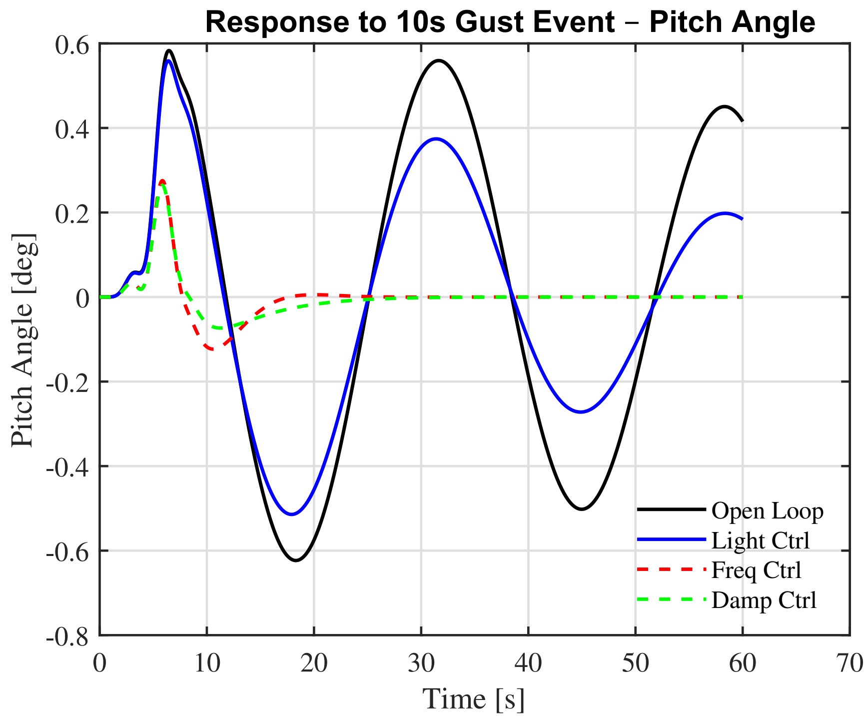

Figure 6.3: Pitch angle response to 10-second gust event for all control configurations

Similarly to what has already been done for acceleration, the relative percentage reduction values compared to the open-loop case are presented below:

Table 6.2: Maximum pitch angle reduction under gust event (relative to open-loop)

Control Strategy	**Max Pitch Reduction** [%]
Light Control	−10.2
Freq Control	−56.1
Damp Control	−58.0

The analysis of the results clearly shows how, even in the presence of a high impulse disturbance, the active control system can produce a significant attenuation of the pitch peak. The *light control* results in a limited reduction of the maximum pitch of about 10%, consistent with the unaggressive dynamics of the controller.

The *frequency-aggressive* and *damping-aggressive* controls, on the other hand, show significantly greater reductions of around 56% and 58% respectively compared to the open-loop.

This behaviour can be interpreted in light of the impulsive characteristics of the EOG and the dominance of the degree of freedom in pitch. In such rapid and time-concentrated events, both controllers, although acting through different mechanisms, induce similar changes in the system's dynamic matrices, in fact the frequency-aggressive controller increases the effective stiffness of the system that induce an increasing of the speed of response and thus containing the peak, on the other hand, the damping-aggressive controller, reacts by enhancing damping, accelerating the decay of the oscillation. However, given the brevity of the pulse and the single-mode nature of the response, the two strategies are equivalent in terms of effectiveness, both being able to counteract the gust with sufficient force to balance the transmitted aerodynamic moment.

Numerous academic publications and technical reports emphasise that reducing the maximum pitch angle reached by the platform under extreme environmental conditions is a key objective in the design of floating offshore wind turbines, with direct implications on structural costs, system stability, and operational adaptability.

In particular, the *Definition of the UMaine VolturnUS-S Reference Platform Developed for the IEA Wind 15 Megawatt Offshore Reference Wind Turbine* and *The IEA Wind Task 49 Reference Floating Wind Array Design Basis* reports clearly specify that one of the most stringent constraints for platform sizing is to keep the pitch angle below 7.5°. This limit is directly related to hydrostatic stability requirements, turbine cut-out margins, and operational safety criteria. The same document also adds that the maximum allowable pitch angle is a limiting factor for the application of turbines in marine environments characterised by severe weather-oceanographic conditions, and this directly affects the geo-operational feasibility of the technology. [5, 19]

Further confirmation of the importance of this parameter can be found in the report *Design of Floating Offshore Wind Turbine IEA 15 MW*, where it is explicitly stated that in order to keep the pitch angle below 3.5° under extreme load conditions, it was necessary to introduce a concrete ballast to lower the platform's centre of gravity. However, this solution both significantly increased the overall mass and also the accelerations transmitted to the tower, further aggravating the dynamic stresses and requiring more robust and expensive towers (see previous section for implications associated with tower-top acceleration). [15]

Similarly, the paper *A New Methodology for Upscaling Semi-Submersible Platforms* points out that the maximum pitch limits under severe load conditions are a necessary condition for *upscaling* turbines, i.e., for increasing the power rating and thus the productivity of plants. The ability to effectively contain the pitch angle below critical values, therefore, allows the size of the turbine to be extended without incurring structural instabilities or disproportionate increases in mass. [27]

In light of these considerations, it is evident that the active control system on the mooring cables implemented in this thesis can be an advantageous technological solution used to reduce the maximum pitch angle

Fatigue Analysis of Mooring Cables: DeqL

To assess the long-term effects of the dynamic action on mooring cables, a simplified fatigue analysis was conducted, aimed at estimating the cumulative Damage Equivalent Load (DeqL) on a single cable, over a time horizon of 20 years of operation.[14].

The approach followed is based on the combination of static and dynamic stresses acting on the cables, in order to estimate the cumulative impact of time-varying cyclic loads, consistent with the environmental conditions simulated for each bin. In particular, the rainflow counting method was used, a standardised technique for the identification of equivalent load cycles, which allows the cumulative damage to be calculated in relation to the amplitude of the cycles recorded along the time series of stresses.

It should be noted, however, that the analysis conducted is approximate in nature, as it does not take into account relevant secondary effects, including:

- the non-linear dynamics peculiar to cables, which may present relative motion even in the absence of platform movement;
- the dependence of fatigue damage not only on the cycle amplitude, but also on the absolute level of mean stress, information not fully captured by the rainflow procedure;
- the non-modelling of the axial response of the strands or materials constituting the cable.

These simplifications imply that the DeqL values obtained are probably underestimates, as the rainflow method, by its nature, filters out absolute frequency and stress content, focusing on the amplitude of cycles rather than their energy content or average stress level. Starting from the tension inside each bin extracted from the simulation, we then summed up the static tension that we had calculated in the static equilibrium configuration. (Please refer to the apposite section in chapter 4 for further details). Once the total tension inside each bin is known, we proceed with the rainflow counting. In the end, Using the following equation, we were able to calculate the equivalent fatigue damage level for a set of cycles at different frequencies:

$$D_{\text{eqL},c} = \left(\frac{\sum_i N_i \cdot S_i^m}{N_{\text{eq}}} \right)^{\frac{1}{m}} \tag{6.3}$$

Where:

- $D_{\text{eqL},c}$: equivalent damage level for each cable
- S_i: amplitude of the i-th cycle (first column of the rainflow matrix)
- N_i: number of cycles with amplitude S_i (second column of the rainflow matrix)
- m: fatigue exponent (we used $m = 3$)
- N_{eq}: number of equivalent cycles (we chose 60 1Hz per 60 s) [14].

The results obtained are shown in the table below. In quantitative terms, the following indicative values are observed:

Table 6.3: Damage Equivalent Load (DeqL) for each control strategy

Control Strategy	**DeqL - Max [N]**	**DeqL - Min [N]**	**DeqL - Mean [N]**
Light Control	55.39	0.00	54.92
Freq Control	26.07	0.00	29.05
Damp Control	33.94	0.00	31.09

- Light control: higher stresses and wider oscillations, associated with significantly higher equivalent damage;
- Frequency-aggressive control: DeqL $\approx$ 29 N;
- Damping-aggressive control: DeqL $\approx$ 33 N.

It is also very interesting to notice that during the simulation conducted, the cable number two was never active, and this led to a zero DeqL on the cable. The other two cases show low and comparable DeqL values, confirming that both active control strategies can effectively attenuate stress excursions in the cables, reducing the number and intensity of fatigue load cycles. These preliminary results suggest that the control system developed may contribute, at least in part, to reducing the structural requirements on cables, enabling the use of less onerous materials or the reduction of the overall length and mass of the cables themselves, with benefits also in terms of installation costs and logistics. It is emphasised, however, that for a comprehensive fatigue life assessment, it is necessary to proceed with a more detailed analysis, integrating:

- multi-body models of cables with internal degrees of freedom;
- fluid-structure interaction and vortex-induced vibration (VIV) phenomena;
- material-specific criteria (S–N curves) for damage accumulation, according to Palmgren–Miner or more advanced probabilistic models.

Only through an analysis of this nature will it be possible to more reliably quantify the potential increase in service life and more accurately validate the estimated reductions in DeqL under different operating conditions.

Energy Analysis of the Active Control System on the Cables

The energy used by the active control system during the entire simulation was estimated using a simplified method based on a linear elastic model of the mooring cables. In particular, it was assumed that each active cable can be modelled as a rigid, non-dissipative spring, with elastic stiffness defined according to the relation:

$$K_{\mathrm{el}} = \frac{E \cdot A_{\mathrm{cable}}}{l_{\mathrm{cable}}} \tag{6.4}$$

where E is the Young's modulus of the cable material, A_{cable} its cross-sectional area, and l_{cable} the cable length.

According to the model adopted, the cable length variation induced by the control system (ΔL) was derived from the relationship:

$$\Delta L(t) = \frac{T_{\mathrm{dyn}}(t)}{K_{\mathrm{el}}} \tag{6.5}$$

Where $T_{\mathrm{dyn}}(t)$ represents the dynamic component of the tension resulting from the active control of the cable. The control velocity of the cable, i.e., the time derivative $\delta v(t) = \frac{d}{dt}\Delta L(t)$, was obtained numerically by differentiating the signal $\Delta L(t)$.

The total tension acting on the cable was reconstructed by adding the static component, previously calculated in the equilibrium phase, to the controlled dynamic component. The instantaneous mechanical power associated with the control system was obtained as a scalar product between the total tension and the actuation speed:

$$P(t) = T_{\text{tot}}(t) \cdot \delta v(t) \tag{6.6}$$

For the calculation of the net energy used, a second simplification was also adopted: it was assumed that for sections where $P(t) > 0$, i.e., when the system exerts traction on the cable, energy is consumed, while for $P(t) < 0$, partial or total energy recovery is assumed.

For this purpose, three different scenarios were analysed:

- No recovery (efficiency = 0%)
- Total recovery (efficiency = 100%)
- Partial recovery (efficiency = 80%)

The results are presented in the table below:

Table 6.4: Total energy consumed by control system in different recovery scenarios

Scenario	**Light Control [kW]**	**Freq Control [kW]**	**Damp Control [kW]**
No recovery	6.11×10^4	2.74×10^3	1.73×10^4
Perfect recovery (100%)	5.70×10^2	2.84×10^2	2.72×10^3
Partial recovery (80%)	1.27×10^4	7.75×10^2	5.63×10^3

The analysis shows that, at the current state of technology, the energy consumption associated with the control system is still too high to make its use sustainable in operational industrial contexts. However, a relevant observation to emerge from the analysis is that the power used is strongly influenced by the speed at which the cable is controlled ($\delta v(t)$), which in turn is linked to the amplitude of platform movements:

- In the case of **light control**, where the permissible movements are large and weakly damped, the value of $\delta v(t)$ is high, and consequently so is the overall energy consumption.

- In contrast, in the **frequency-aggressive** and **damping-aggressive** controls, the containment of dynamics significantly reduces $\Delta L(t)$ and the associated speed, leading to lower energy consumption.

These results suggest that the use of the active control system is only technically justified in the presence of aggressive control, which can provide significant dynamic benefits in terms of structural stability and stress reduction. Conversely, the adoption of a light control results in low dynamic benefits but high energy consumption, and is therefore sub-optimal from all points of view. Looking forward, control strategies will also need to be optimised in the light of overall energy yields, possibly by integrating active energy recovery systems or control algorithms that minimise mechanical effort without compromising platform stability.

6.1.2 Evaluating Selective Control Activation Strategies

In all scenarios analysed so far, it was assumed that the active control system operates continuously, i.e., that it is active for the entire duration of the simulation. Although this assumption allows for a clear assessment of the dynamic effectiveness of the control under different environmental conditions, it resulted in a significant increase in the energy consumed, as highlighted in the energy analysis above.

However, by reconsidering the problem from a design perspective more in keeping with engineering practice, an alternative strategy can be formulated. In the structural field, in fact, the sizing of an offshore system, from the tower to the mooring cables, is generally carried out on the basis of the worst-case scenario, i.e., considering the most severe environmental conditions that the system could reasonably be expected to face during its lifetime. This principle, if extended to the operation of the controller, suggests a possible selective and non-continuous use of the active actuation system. The proposed idea consists in limiting the activation of the control to only those instances in which one or more critical dynamic parameters (in particular tower-top acceleration) exceed a pre-set threshold. In other words, the control system would be switched on exclusively during the most relevant dynamic peaks, acting as a transient and targeted mitigation mechanism, rather than as a continuous regulation tool.

The advantages of this approach are twofold:

Reduction in energy consumed, as the system would only be activated for short time intervals;

Rescaling of the dynamic problem: by acting on the most severe peaks, the maximum value of key parameters (acceleration, pitch, tension in cables) would be reduced, allowing the platform to be designed on lower thresholds, reducing mass, cost, and structural stress. This approach, if properly implemented, could retain much of the dynamic benefits of active control while significantly mitigating its energy impact. In engineering terms, this would result in an optimal trade-off between structural and energy efficiency of the control system.

In the following work, it will therefore be interesting to explore conditional activation strategies (event-based control), based on threshold logic or prediction of dynamic behaviour, evaluating their effectiveness in terms of both performance, energy, and structural costs.

To support this hypothesis, a preliminary test was conducted in which the control system was only activated in the three bins where the maximum average acceleration at the top of the tower was found.

Table 6.5: Top 3 environmental bins with the highest average tower-top acceleration (Open Loop)

Bin ID	**Wave Height** H_s **[m]**	**Wind Speed** W_s **[m/s]**	**Mean Acceleration** $\bar{a}$ **[m/s^2]**
4	4.00	10.50	0.6334
3	2.50	7.50	0.2831
2	1.50	4.50	0.1285

The results obtained are shown in tabular form :

Table 6.6: Percentage reduction of key statistical parameters relative to the Open Loop configuration (Top 3 bins)

Control Strategy	**Max [%]**	**Mean [%]**	**Range [%]**	**Std [%]**
Light Control	-26.63	-21.92	-27.21	-26.20
Frequency Control	-27.54	-75.36	-27.14	-61.63
Damping Control	-28.33	-50.76	-27.86	-32.63

Although this is a limited activation strategy, the data show that the reductions compared to the open-loop scenario remain significant, confirming the ability of active control to mitigate dynamic stresses even when applied selectively. As expected, the reductions are lower than in the case of activation on all bins, since the system only intervenes in the most critical environmental conditions. Now we are going to present the value in terms of energy consumption.

Table 6.7: Energy consumption and relative reduction with partial-time activation

Average Power [kW]				**Relative Reduction [%]**			
Recovery	Light	Freq	Damp	Recovery	Light	Freq	Damp
No	20927.85	756.00	5672.19	No	-65.75	-72.41	-67.21
Perfect	84.37	76.75	950.81	Perfect	-85.20	-72.98	-65.04
Efficient	4253.06	212.60	1895.09	Efficient	-66.51	-72.57	-66.34

Which shows a reduction of more than 65% compared to the continuously controlled scenario. This result is because the system was only active for 42.1% of the total simulation time, corresponding to the cumulative duration of the three selected bins. These first experimental results demonstrate how a conditional activation logic, despite its simplicity, can be an effective solution to maintain much of the dynamic benefits of active control, with a drastic reduction in energy costs. These evidences support the concrete possibility of an industrial application of this technology, provided it is integrated with intelligent activation algorithms capable of recognising and anticipating the most severe operating conditions.

6.1.3 Final Considerations on the Results Obtained

The analysis conducted clearly demonstrated how the implementation of an active control system on the mooring cables can significantly improve the dynamic response of a floating wind platform in deep water, under realistic environmental conditions. The results obtained, expressed in relative terms compared to the uncontrolled case, highlighted the effectiveness of the control strategies in reducing critical parameters such as acceleration at the top of the tower, pitch angle during extreme wind gusts, fatigue damage on the cables, and energy consumption of the system itself.

In detail, the frequency-aggressive control proved to be the most effective in terms of damping oscillations, with average reductions in acceleration of over 85% and a significant decrease in maximum pitch angle at gust. This configuration, with an optimal damping ratio ($\zeta \approx 0.7$), also showed the best compromise between dynamic stability and speed of response. The damping-aggressive control, while slightly less effective in containing spikes, provided comparable performance, with the advantage of a more damped response and a consistent reduction in cumulative fatigue damage. The light control confirmed the validity of the control logic, but showed that it is not a good choice for both the benefits in terms of the dynamic implementation and the energy consumption.

From an energy point of view, the implementation of continuous control revealed consumption that was still too high for a direct industrial application. However, the introduction of a selective conditional activation strategy, limited to the most critical environmental bins, achieved a consumption reduction of more than 65% compared to the continuous control case, while maintaining good efficiency levels. This result suggests that the adoption of active but not permanent control logics may represent a realistic and promising solution to combine structural benefits and energy sustainability.

Overall, the results obtained validate the methodological approach adopted and indicate that the proposed system can contribute, if suitably optimised, to the improvement of structural stability, the extension of component lifetimes and the quality of power delivered by floating wind turbines, providing a potential tool for structural cost containment and operational extension to more severe weather and sea environments.

6.2 Next Steps and Future Developments

As widely discussed in the previous chapters, the work carried out in this thesis is essentially preliminary in nature, to explore and experimentally evaluate the effects of introducing active control in the mooring cables of offshore wind platforms, a technology that is still at a very early stage.

Based on the results obtained, numerous aspects only partially addressed here may be the subject of future in-depth studies and developments. First, it is suggested that the numerical model of the platform used be completed, extending it to the six degrees of freedom of the system, in order to conduct a complete dynamic analysis of the structural response. At the same time, it is recommended that a specific study be carried out on the dynamics of mooring cables, going beyond the “rigid beam” approximation and adopting models capable of more accurately representing the non-linear and deformable behaviour of cables under variable loads. Secondly, it is necessary to conduct simulations in virtual environments that more closely resemble real-life operating conditions. The environmental model used in this thesis has been deliberately simplified for reasons of feasibility and speed of implementation; however, to obtain reliable results that are representative of the actual behaviour of the system, it will be essential to use advanced software capable of faithfully reproducing environmental conditions, including wave transformation in the vicinity of the platform, additional hydrodynamic loads, and fluid-structure interactions.

Once these additions are done, it'll be possible to do a critical and in-depth analysis of the results, getting a realistic estimate of how well the active control system works. This will allow not only a quantitative comparison with systems without control, but also an absolute assessment of how effective the proposed technology is. Further developments will also need to address the methodology used to obtain the results presented. In particular, an in-depth analysis of fatigue in mooring cables is required, to be carried out using more detailed models than the simplified approach adopted at this stage. Similarly, the energy analysis will need to be significantly enhanced, examining in detail the influence of each degree of freedom on overall energy consumption and identifying solutions to increase the energy efficiency of the system, to make the proposed technology sustainable and applicable at an industrial level.

In conclusion, the results obtained represent a promising starting point for demonstrating the potential of active control, even if only partial, in mitigating the movements of offshore platforms. However, in order for this technology to be effectively implemented on an industrial scale, it is necessary to fill numerous gaps that still exist, with particular attention to the optimisation of energy consumption, which is one of the main critical factors for its practical application.

Appendix A

Simulation of a real environment

The MATLAB codes developed to generate a simulation of a realistic environment are presented below.

Considering that the definition of the real environment has been dealt with in depth in Chapter 2, in particular in Section 2.3.1, only the implemented codes will be reported here, in order to avoid redundancy and keep the discussion concise.

The codes are divided into sections, following the same sub-section structure adopted in Chapter 2, in order to facilitate consultation and improve the reader's understanding.

For a detailed analysis of the methodology adopted and the reasons behind the structure of the MATLAB code, please refer to Chapter 2.

A.1 Environmental Binning and Load Estimation

Listing A.1: Calculation of joint probability matrix from wind and wave data

```
function [centers_H,centers_W,P]=loads();

%% WIND AND CURRENT LOADS

% Parameters
lambda = 6;       % weibull scale
k = 2;            % shape factor
sigma = 0.788;    % sigma factor for H_s

```

```
% Vector for the CDF graphs
H = linspace(0,5,1000);   % wave height [m]
W = linspace(0,12,1000);  % wind speed [m/s]

% CDF simulation
cdf_W = wblcdf(W, lambda, k);     % CDF of wind
cdf_H = raylcdf(H, sigma);        % CDF of wave

% Meshgrid for the surface
[WW, HH] = meshgrid(W, H);

% Independent distributions
P_H = raylcdf(HH, sigma);         % CDF of wave height
P_W = wblcdf(WW, lambda, k);      % CDF of wind speed

% Independent joint PDF and exceedance probability
PDF_joint = raylpdf(HH, sigma) .* wblpdf(WW, lambda, k);
P_joint = (1 - P_H) .* (1 - P_W); % surface of exceedance

% Creation of the bins
edges_H = [0, 1, 2, 3, 5];     % limits for the wave bins
edges_w = [0, 3, 6, 9, 12];    % limits for the wind bins

% Centers of each bin
centers_H = 0.5 * (edges_H(1:end-1) + edges_H(2:end));
centers_W = 0.5 * (edges_w(1:end-1) + edges_w(2:end));

% Probability for waves and wind
prob_H = diff(raylcdf(edges_H, sigma));
prob_W = diff(wblcdf(edges_w, lambda, k));

% Joint probability matrix (N_H x N_W)
P = prob_H' * prob_W;
```

```
end
```

A.2 Generation of Environmental Time Series

Listing A.2: Function to generate wind and wave time histories

```
function [wind_ts_all, wave_ts_all] = generate_time_history();
    [centers_H, centers_W, ~] = loads();

    global time_final dt df t0 freq_vector times
    global I l Tp sigma_1
    global r_blades g

    %% time domain setup
    time_final = 60; % simulation duration [s]
    dt = 0.01;       % time step [s]
    freq_limit = 0.5;
    t0 = 0;

    %% seeds
    wind_seed = 42;
    wave_seed = 99;

    %% time and frequency vector setup
    times = time_function(t0, time_final, dt);
    nT = numel(times);
    df = 1 / time_final;
    freq_vector = df:df:freq_limit;

    %% bins
    nH = length(centers_H);
    nW = length(centers_W);

    wind_ts_all = cell(nH, nW);
```

```
wave_ts_all = cell(nH, nW);

%% loop over bins
for i = 1:nH
    for j = 1:nW
        Hs = centers_H(i);
        v_mean_wind = centers_W(j);

        rng(1000 + i*10 + j);
        phase_wind = rand(1, numel(freq_vector)) * 2*pi;

        rng(2000 + i*10 + j);
        phase_wave = rand(1, numel(freq_vector)) * 2*pi;

        %% wind calculation
        I_ref = 0.16;
        b = 5.6;
        sigma_1 = I_ref * (0.75*v_mean_wind + b);
        I = sigma_1 / v_mean_wind;
        l = 340.2;

        S_wind = (4 * I^2 * v_mean_wind * l) ./ (1 + (6 *
           freq_vector * l / v_mean_wind).^2).^(5/3);
        amp_wind = sqrt(2 * S_wind * df);
        wind_vs_time = compute_time_series(amp_wind,
           phase_wind, nT, v_mean_wind);

        %% wave calculation
        gamma = 1.0;
        Tp = 11;
        fp = 1 / Tp;

        sigma = 0.09 * ones(size(freq_vector));
        sigma(freq_vector <= fp) = 0.07;
```

```
            exp1 = -1.25 * (freq_vector / fp).^(-4);
            exp2 = -0.5 * (((freq_vector / fp) - 1) ./ sigma).^2;

            S_JS = 0.3125 * Hs^2 * Tp * (freq_vector / fp).^(-5)
               ...
                   .* exp(exp1) .* (1 - 0.287 * log(gamma)) .*
                      gamma.^exp(exp2);

            a_JS = sqrt(2 * S_JS * df);

            % ensure Hs match
            Hs_calc = 4 * sqrt(trapz(freq_vector, S_JS));
            while max(abs(S_JS - S_JS .* (Hs / Hs_calc))) >
               0.0001
                S_JS = S_JS .* (Hs / Hs_calc);
                Hs_calc = 4 * sqrt(trapz(freq_vector, S_JS));
            end

            h_amp = a_JS .* (Hs / Hs_calc);
            wave_height_vs_time = compute_time_series(h_amp,
               phase_wave, nT, 0.0);

            wind_ts_all{i,j} = wind_vs_time;
            wave_ts_all{i,j} = wave_height_vs_time;
        end
    end
end
```

A.3 Conversion of Time Series into External Loads

Listing A.3: Function to compute forces and moments on the floating platform

```
function [floating_platform_force_in_time] = compute_forces()
```

```
[wind_ts_all, wave_ts_all] = generate_time_history();

% Global variables
global A_column pho_sea pho_air l_plat g A_rot h_t C_T_wind
global Tp dt times

% Preallocation
[nH, nW] = size(wind_ts_all);
floating_platform_force_in_time = cell(nH, nW);

for i = 1:nH
    for j = 1:nW
        wind_vs_time = wind_ts_all{i,j};
        wave_height_vs_time = wave_ts_all{i,j};

        % Wave phase speed and time delay (discrete)
        C_P = (g / (2*pi)) * Tp;
        tau = round((2 * l_plat) / C_P / dt);

        %% Wind forces and moment
        wind_force = 0.5 * pho_air * A_rot * C_T_wind * (
           wind_vs_time.^2);
        wind_moment = wind_force * h_t;

        %% Wave forces
        wave_force = pho_sea * g * wave_height_vs_time *
           A_column;

        % Delayed signals for moment calculation
        H1 = wave_height_vs_time(1:end - tau);
        H2 = wave_height_vs_time(tau + 1:end);
        wave_moment_raw = pho_sea * g * A_column * l_plat .*
           (H1 - H2);
        wave_moment = [zeros(1, tau), wave_moment_raw];
```

```
            % Total force and moment
            total_forces = wind_force + wave_force;
            total_moment = wind_moment + wave_moment;

            % Store result
            floating_platform_force_in_time{i,j} = [total_forces
               (:), total_moment(:)];
        end
    end
end
```

A.4 Extreme Operating Gust (EOG) Modelling

Listing A.4: Function to compute the gust force according to IEC 61400-1

```
function [gust_force] = generating_gust()
global sigma_1 v_mean_wind A_column pho_sea pho_air l_plat g
   A_rot h_t Tp C_T_wind dt r_blades times

%% Gust calculation based on IEC 61400-1
% Define all the parameters
v_mean_wind = 11;          % [m/s] nominal velocity
delta = 42;                % [m] longitudinal turbulence scale
   parameter
d_rotor = 2 * r_blades;    % [m] rotor diameter
v_e1 = 42.5;               % [m/s] reference extreme wind speed
T_gust = 10.5;             % [s] gust duration

% Compute gust magnitude
term1 = 1.35 * (v_e1 - v_mean_wind);
term2 = 3.3 * (sigma_1 / (1 + 0.1 * (d_rotor / delta)));
v_gust = min(term1, term2);  % [m/s] maximum gust perturbation

```

```
% Initialize gust profile
gust_profile = zeros(size(times));

% Compute gust profile as per IEC model
for i = 1:length(times)
    t = times(i);
    if t <= T_gust
        gust_profile(i) = -0.37 * v_gust * sin(3 * pi * t /
           T_gust) * ...
                          (1 - cos(2 * pi * t / T_gust));
    end
end

% Compute aerodynamic gust force
gust_force = 0.5 * pho_air * A_rot * C_T_wind .* (gust_profile .^
    2);
```

Appendix B

Static Equilibrium Configuration

The MATLAB code developed allows the static configuration of the floating wind platform to be calculated for a generic environmental condition (bin), with particular reference to the stress distribution in the mooring cables and the corresponding pitch angle at equilibrium. The aerodynamic force is assessed on the basis of the average wind speed, assuming $C_T = \frac{8}{9}$ for winds below 11 m/s and using the nominal turbine power for higher wind speeds. The current force is estimated using a drag force, adopting a coefficient $C_D = 1.5$ consistent with the Reynolds regime under consideration.

The resulting forces are decomposed along the directions of the mooring cables, each characterised by a fixed orientation. The set of active cables (i.e., capable of transmitting force in the direction of the ambient force) is then determined and, depending on the number of active cables (one or two), the plane equilibrium system is solved to estimate the static tensions.

For each cable, it is verified whether the configuration is taut or slack by comparing the minimum geometric angle with the angle resulting from the balance between weight and the horizontal component of tension. Depending on the state of the cable, the vertical component of the force transmitted is calculated, and from it, the torque generated.

Finally, by imposing the equilibrium of moments between the wind action and the mooring system, the static equilibrium angle of the platform is calculated. The results obtained for each environmental bin are saved in vector form for later use in the dynamic simulation of the system. All the steps followed in order to write the code below are carefully explained in the appropriate section in Chapter 4, so for a detailed analysis of the methodology adopted and the reasons behind the structure of the MATLAB code, please refer to Chapter 4.

Listing B.1: Static configuration and equilibrium angle calculation under environmental loads

```
%% Definition of the input variable
v_curr=1; % [m/s]
alfa_wind=321; % [deg]
alfa_current=12; % [deg]

% Preallocation
T_final_all = zeros(3, length(centers_W));
theta_eq_all = zeros(1, length(centers_W));

%% Loop for each bin center
for j = 1:length(centers_W)
    ws = centers_W(j);
    v_mean_wind = ws;

    % Check angle ranges
    while alfa_wind > 360 || alfa_wind < -360
        fprintf('Error:␣the␣angle␣must␣not␣exceed␣-360␣to␣+360␣
           deg');
        alfa_wind = input('Insert␣alfa␣between␣x␣axis␣and␣F_wind␣
           [  ]:␣');
    end
    while alfa_current > 360 || alfa_current < -360
        fprintf('Error:␣the␣angle␣must␣not␣exceed␣-360␣to␣+360␣
           deg');
        alfa_current = input('Insert␣alfa␣between␣x␣axis␣and␣
           F_current␣[  ]:␣');
    end

    % Direction setup
    alfa_wind_rad = deg2rad(alfa_wind);
    alfa_current_rad = deg2rad(alfa_current);
```

```
%% Wind force
P_wind = 15e6; % [W]
pho_air = 1.225; % [kg/m^3]
if v_mean_wind < 11
    C_T_wind = 8/9;
    F_wind = 0.5 * C_T_wind * A_rot * pho_air * v_mean_wind
       ^2;
else
    F_wind = P_wind / v_mean_wind;
    C_T_wind = F_wind / (0.5 * v_mean_wind^2 * pi * r_blades
       ^2);
end

%% Current force
C_D = 1.5;
pho_sea = 1025; % [kg/m^3]
F_current = 0.5 * pho_sea * A_lat_column * C_D * v_curr^2;

%% Resultant force vector
F_wind_vector = F_wind * [cos(alfa_wind_rad), sin(
   alfa_wind_rad)];
F_current_vector = F_current * [cos(alfa_current_rad), sin(
   alfa_current_rad)];
F_tot_vector = F_wind_vector + F_current_vector;
F_tot = norm(F_tot_vector);
F_hat_tot = F_tot_vector / F_tot;

%% Cable versors
angles_cable_deg = [150, 30, 270];
t_hat = [cosd(angles_cable_deg); sind(angles_cable_deg)]';

%% Angles between cables and resultant force
theta_deg = acosd(t_hat * F_hat_tot');
```

```
%% Determine active cables
active_idx = find(theta_deg >= 0 & theta_deg <= 90);
count = length(active_idx);
theta_rad = deg2rad(theta_deg(active_idx));
F_tot_vector3D = [F_tot; 0];

%% Tension solving
T_final = zeros(3,1);
switch count
    case 1
        i = active_idx;
        t = [cosd(theta_deg(i)); sind(theta_deg(i))];
        T_final(i) = dot(F_tot_vector3D, t);
    case 2
        idx = active_idx;
        A = [cosd(theta_deg(idx(1))), cosd(theta_deg(idx(2)))
           ;
             sind(theta_deg(idx(1))), -sind(theta_deg(idx(2))
               )];
        T_vals = A \ F_tot_vector';
        T_final(idx) = T_vals;
    otherwise
        error('No␣solvable␣configuration');
end

%% Taut/slack check
theta_taut = asin(see_depth / l_cable);
F_g = pho_steel * A_cable * l_cable;
F_down = zeros(1,3);
for i = 1:3
    T = T_final(i);
    theta_s = atan(F_g / max(T, 1e-6));
    if theta_s > theta_taut
```

```
            F_down(i) = F_g;
        else
            F_down(i) = (T * see_depth) / sqrt(l_cable^2 -
               see_depth^2);
        end
    end

    %% Moment balance and static angle
    gamma = 12; % [deg]
    M_cable = +F_down(1)*(l_plat*cosd(30)) - F_down(2)*(l_plat*
       cosd(30)) + F_down(3)*cosd(gamma);
    M_wind = F_wind * h_rna;
    M_res = M_wind - M_cable;
    C_V = 0.8;

    res = M_res / (2 * l_plat^2 * A_column * g * pho_sea * C_V);
    if abs(res) > 1
        theta_eq_all(j) = NaN;
    else
        theta_eq_all(j) = asin(res);
        T_final_all(:, j) = T_final;
    end
end
```

Nomenclature

This section provides a comprehensive list of all the symbols, parameters, and variables used throughout this thesis, together with their definitions and physical meaning.

p3.5cm p11cm

Symbol	**Description**
k	Shape parameter of the Weibull distribution (controls wind speed dispersion)
λ	Scale parameter of the Weibull distribution (related to mean wind intensity)
σ	Scale parameter of the Rayleigh distribution (wave height dispersion)
$f_W(w_s)$	Probability density function of the Weibull distribution
$F_W(w_s)$	Cumulative distribution function of the Weibull distribution
$F_H(h_s)$	Cumulative distribution function of the Rayleigh distribution
w_s	Representative wind speed (m/s)
h_s	Representative significant wave height (m)
$F_{\text{wind}}(t)$	Instantaneous aerodynamic thrust force on the rotor (N)
$F_{\text{wave}}(t)$	Instantaneous hydrostatic force from wave-induced elevation (N)
$M_{\text{wind}}(t)$	Aerodynamic torque induced by wind on the platform (Nm)
$M_{\text{wave}}(t)$	Moment induced by wave elevation difference on columns (Nm)
A_{rot}	Rotor frontal area (m^2)
C_T	Aerodynamic thrust coefficient of the rotor
ρ_{air}	Air density (kg/m^3)
ρ_{sea}	Seawater density (kg/m^3)
A_{col}	Plan area of a platform column (m^2)
l_{plat}	Distance from the peripheral column to the central one (m)
g	Acceleration due to gravity (≈ 9.81 m/s^2)
Δt	Simulation time step (s)
T	Tension in the mooring cable (N)

d Horizontal distance between platform and anchor point (m)

θ_t Angle defined by the geometric layout of a taut mooring cable (rad)

θ_s Static slope angle defined by the equilibrium of vertical force in a slack cable (rad)

F_{down} Vertical component of cable force (N)

M_{cable} Total moment generated by cable forces (Nm)

h_{RNA} Height of rotor-nacelle assembly from platform pivot point (m)

M_{res} Resultant moment after subtracting cable moment from wind-induced moment (Nm)

A_{circle} Cross-sectional area of a floating column or volume element (m^2)

C_V Volume coefficient used in equilibrium computations

θ_{eq} Static equilibrium pitch angle of the platform (rad)

I_{ref} Reference turbulence intensity (dimensionless)

Λ Longitudinal turbulence scale length (m)

$v_{ts}(t)$ Time series value of wind speed at time t (m/s)

$h_{ts}(t)$ Time series value of wave elevation at time t (m)

H_s Significant wave height (m)

T_p Peak wave period (s)

τ Time delay between wave action on columns (s)

η Wave surface elevation (m)

$S(f)$ Spectral energy density function (m^2/Hz)

γ JONSWAP peak enhancement factor

EOG Extreme Operating Gust

μ Mean value of a distribution

DOFs Degrees of Freedom (e.g., heave and pitch)

Δf Spectral resolution

h_{t} Height of the Tower (m)

$h_1^{\text{ts}}(t)$, $h_2^{\text{ts}}(t+\tau)$ Wave elevation of the two columns

$F_{\text{gust}}(t)$ Thrust force over time applied to the turbine

$v_{\text{gust}}(t)$ Time profile of the wind speed during the gust

ω_n Natural pulsation

ω_d Angular frequency of the damped oscillation

ζ Damping ratio

m_{tower} Total mass of the tower (kg)

r_1 Inner radius of the tower (m)

r_2 Outer radius of the tower (m)

$z_{\mathrm{CG,tot}}$ Vertical position of the global centre of mass (m)

α_{wind} Angular direction of the wind force (rad)

$\alpha_{\mathrm{current}}$ Angular direction of the current force (rad)

$\theta_1, \theta_2, \theta_3$ Angular distance from each cable to the total force (rad)

l_{cable} Length of the cable (m)

I_{xx} Pitch moment of inertia (kg·m^2)

m_{blades} Effective radial position of the blade center of mass (m)

$F_{\mathrm{curr}}(t)$ Instantaneous current force (N)

$F_{\mathrm{tot}}(t)$ Vector sum between $F_{\mathrm{wind}}(t)$ and $F_{\mathrm{curr}}(t)$ (N)

T_1, T_2, T_3 Static tension inside each cable (N)

$\delta\theta$ Infinitesimal angular distance (rad)

k^b_{zz} Buoyancy stiffness related to Heave (N/m)

k^g_{zz} Geometric stiffness related to Heave (N/m)

$k^g_{\theta\theta}$ Geometric stiffness related to pitch (N/rad)

$k^b_{\theta\theta}$ Buoyancy stiffness related to pitch (N/rad)

m_{cable} Mass of the cable (kg)

$\mathrm{matrix}_{\mathrm{plat}}$ Mass matrix of the platform

M_{tot} Total mass matrix of the system

$v_\infty(t)$ Undisturbed wind speed (m/s)

$a(t)$ Tower top acceleration (m/s^2)

$DeqL$ Damage equivalent load

T_{dyn} Dynamic tension inside each cable (N)

$gain$ gain matrix

Bibliography

[1] Wind energy generation systems – part 1: Design requirements, 2019. Fourth Edition, Geneva: IEC.

[2] Pole-placement method and lqr analysis. Unpublished manuscript, 2019. Internal coursework document on classical control theory and optimal pole assignment.

[3] International Energy Agency. Wind energy in 2024: Key trends and policy implications. Technical report, International Energy Agency, May 2024. URL `https://www.iea.org/reports/wind-energy-in-2024-key-trends-and-policy-implications`. Published as part of the IEA Renewables Series.

[4] International Energy Agency. Renewables 2024: Analysis and forecast to 2029. Technical report, International Energy Agency, June 2024. Available at: `https://www.iea.org/reports/renewables-2024`.

[5] Christopher Allen, Anthony Viselli, Habib Dagher, Andrew Goupee, Evan Gaertner, Nikhar Abbas, Matthew Hall, and Garrett Barter. Definition of the umaine volturnus-s reference platform developed for the iea wind 15-megawatt offshore reference wind turbine. Technical Report NREL/TP-5000-76773, National Renewable Energy Laboratory, 2020. URL `https://www.nrel.gov/docs/fy20osti/76773.pdf`.

[6] Srikanth Bashetty and Selahattin Ozcelik. Review on dynamics of offshore floating wind turbine platforms. *Energies*, 14(19):6026, 2021. doi: 10.3390/en14196026.

[7] Tony Burton, Nick Jenkins, Ervin Bossanyi, David Sharpe, and Michael Graham. *Wind Energy Handbook*, chapter 12, pages 771–785. John Wiley & Sons Ltd, 3rd edition, 2021. doi: 10.1002/9781119451143.ch12. Accessed via Wiley Online Library.

[8] Centrale Nantes, BW Ideol. Floatgen demonstrator – centrale nantes offshore test site, 2021. URL https://www.ideol-offshore.com/en/floatgen. Accessed 2025-07-21.

[9] Giuseppe Cicchitelli, Pierpaolo D'Urso, and Marco Minozzo. *Statistica: principi e metodi. Ediz. Mylab. Con aggiornamento online.* Pearson, Milano, 4 edition, 2022. ISBN 9788891915382. Con accesso alla piattaforma MyLab.

[10] Cobra Group. Kincardine offshore wind farm, 2021. URL https://www.offshorewind.biz/projects/kincardine-floating-wind-farm-uk/. Accessed 2025-07-21.

[11] Giuseppe Costanzo, Guy Brindley, and Pierre Tardieu. Wind energy in europe: 2024 statistics and the outlook for 2025–2030. Technical report, WindEurope, February 2025. Published by WindEurope, Brussels.

[12] Howard Dachslager. *Fundamentals of Statistics and Probability Theory: A Tutorial Approach. Vol. 1: Probability Theory.* Learning Step by Step, United States, 2014. ISBN 9781499777110. A step-by-step tutorial guide.

[13] Maria del Cisne Feijóo, Yovana Zambrano, Yolanda Vidal, and Christian Tutivén. Unsupervised damage detection for offshore jacket wind turbine foundations based on an autoencoder neural network. *Sensors*, 21(10):3333, 2021. doi: 10.3390/s21103333. URL https://doi.org/10.3390/s21103333.

[14] Gregg Freebury and Walter Musial. Determining equivalent damage loading for full-scale wind turbine blade fatigue tests. In *19th ASME Wind Energy Symposium*, Reno, Nevada, January 2000. URL http://www.nrel.gov/docs/fy00osti/27510.pdf. NREL/CP-500-27510, National Renewable Energy Laboratory.

[15] Evan Gaertner, Jennifer Rinker, Latha Sethuraman, Frederik Zahle, Bernadette Anderson, Garrett Barter, Nikhar Abbas, Fanchao Meng, Pietro Bortolotti, Witold Skrzypinski, George Scott, Robert Feil, Henrik Bredmose, Katherine Dykes, Matt Shields, Christopher Allen, and Anthony Viselli. Iea wind tcp task 37: Definition of the iea wind 15-megawatt offshore reference wind turbine. Technical Report NREL/TP-5000-75698, National Renewable Energy Laboratory, 2020. URL https://www.nrel.gov/docs/fy20osti/75698.pdf.

[16] Shan Gao, Yi Guo, Xin Tao, Zhaoqing Yang, Xuejiao Zhuang, and Rui Zhang. Dynamic analysis of floating wind turbines considering aerodynamic damping and tower flexibility. *Renewable Energy*, 220:1–17, 2024. doi: 10.1016/j.renene.2024.01.028.

[17] Johannes Gerstmayr and Ahmed A. Shabana. Analysis of thin beams and cables using the absolute nodal coordinate formulation. *Nonlinear Dynamics*, 45:21–34, 2006. doi: 10.1007/s11071-006-9009-0.

[18] Global Wind Energy Council (GWEC) and The Crown Estate. Floating offshore wind – a global opportunity. Technical report, Global Wind Energy Council, 2023. URL `https://gwec.net/wp-content/uploads/2023/10/gwec-report-floating-offshore-wind-a-g`

[19] Matthew Hall, Ericka Lozon, Fiona Devoy McAuliffe, Matteo Baudino Bessone, Ilmas Bayati, Malcolm Bowie, Pauline Bozonnet, Michel Castagné, Ju Feng, Stein Housner, Marek Jan Janocha, Zhiyu Jiang, Yong Yook Kim, Donghee Ko, Konstanze Kölle, Chern Fong Lee, Malakonda Reddy Lekkala, Guodong Liang, Mohammad Youssef Mahfouz, Madhan Mohan, Daniel O'Connell, Muk Chen Ong, Julien Prieur, Vishnu R. N. Rajasree, Anja Schnepf, Thor Snedker, Jean Thurston-Keller, and Chris Wright. The iea wind task 49 reference floating wind array design basis. Technical report, IEA Wind Technology Collaboration Programme, June 2024. NREL/TP-5000-89709.

[20] Ahmad Hassan and Zulqarnain Ali. Design of a semi-submersible floating platform for floating offshore wind turbine (fowt) iea 15-megawatt. Technical report, University of Rostock, 2025. URL `https://www.researchgate.net/publication/389356479`. Course Project, Erasmus Mundus Master EMSHIP+.

[21] International Energy Agency. Global energy review 2025: Renewables. Technical report, IEA, 2025. URL `https://www.iea.org/reports/global-energy-review-2025`.

[22] Nick Jenkins, Ervin Bossanyi, and Tony Burton. *Wind Energy Handbook: Chapter 4 – The Wind Resource*. John Wiley & Sons, 3rd edition, 2021. doi: 10.1002/9781119451143.ch4.

[23] Shengbo Jiang, Changhao Guo, Yulong Liu, Xiaoyu Jin, and Xudong Wang. Dynamic analysis of a barge-type floating wind turbine subjected to mooring failures. *Journal*

of Marine Science and Engineering, 12(4):617, 2024. doi: 10.3390/jmse12040617. URL `https://doi.org/10.3390/jmse12040617`.

[24] Fengmei Jing, Li Xu, Zhiqun Guo, and Hengxu Liu. A theoretical study on the hydrodynamics of a zero-pressurized air-cushion-assisted barge platform. *Journal of Marine Science and Engineering*, 8(9):664, 2020. doi: 10.3390/jmse8090664. URL `https://doi.org/10.3390/jmse8090664`.

[25] Matthew Lackner, Jason Jonkman, Amy Robertson, Andrew Goupee, Henrik Bredmose, and Daniel Zalkind. Isodc final report: Wind turbine optimization and control, 2023. Internal report, International Simulation and Optimization of Dynamic Control project.

[26] V. Leble, B. Luhmann, F. Sandner, and P.W. Cheng. The impact of platform motion on the aerodynamic control of floating offshore wind turbines. *Journal of Physics: Conference Series*, 2265(3):032056, 2022. doi: 10.1088/1742-6596/2265/3/032056.

[27] Zhe Luo, Erin Elizabeth Bachynski, and Torgeir Moan. A new methodology for upscaling semi-submersible platforms for floating offshore wind turbines. Technical report, Norwegian University of Science and Technology (NTNU), 2020. URL `https://hdl.handle.net/11250/2735192`. NTNU Engineering Report, Dept. of Marine Technology, Trondheim.

[28] Mohammad Youssef Mahfouz, Haiyan Hu, and Qiang Tian. A passively self-adjusting floating wind farm layout to increase the annual energy production. *Wind Energy*, 25(11):2344–2363, 2022. doi: 10.1002/we.2786.

[29] I. Mazza, E. Ponzoni, D. Bertalot, O. Zanoli, S. Sadowski, and R. Zaccone. Relazione descrittiva delle soluzioni di ancoraggio e ormeggio. Technical Report Doc. No. P0025305-2-LCC-H15 - Rev. 00, RINA Consulting S.p.A., Lecce, Italy, 2021. Progetto preliminare per la realizzazione di un parco eolico offshore - Odra Energia.

[30] Michael K. McWilliam. Variable length mooring lines for enhancing the performance of floating offshore wind farms. Master's thesis, Technical University of Denmark, December 2024. URL `https://topfarm.pages.windenergy.dtu.dk/PyWake/`.

[31] Fares M'zoughi, Izaskun Garrido, Aitor J. Garrido, and Manuel De La Sen. Fuzzy airflow-based active structural control of integrated oscillating water columns for the enhancement of floating offshore wind turbine stabilization. *International Journal of Energy Research*, pages 1–23, 2023. doi: 10.1155/2023/4938451. URL `https://doi.org/10.1155/2023/4938451`.

[32] Katsuhiko Ogata. *Modern Control Engineering*. Prentice Hall International Editions, Upper Saddle River, New Jersey, 3rd edition, 1997. ISBN 9780132613897. International Edition.

[33] Jakob Olesen, Thomas Nielsen, and Lars Vabbersgaard Andersen. Numerical investigation of active control in mooring lines for floating wind turbines. *DTU Wind Energy Report*, (E-0289), 2022. URL `https://orbit.dtu.dk/en/publications/numerical-investigation-of-active-control-in-`

[34] Yujun Qin, Qiang Tian, Haiyan Hu, Mohammad Youssef Mahfouz, and Niels L. Pedersen. Airflow-based active structural control of floating wind turbines. *Applied Composite Structures*, 15(1):45–61, 2020. doi: 10.1016/j.compstruct.2020.111174.

[35] L. Smith and H. Thompson. Ballast and gravity-based stabilization for offshore platforms. *Journal of Offshore Engineering*, 45:122–134, 2021. doi: 10.1016/j.offeng.2021.04.012.

[36] StackExchange contributors. Describing step response in terms of poles and zeros of transfer function, 2013. URL `https://electronics.stackexchange.com/questions/87088/describing-step-response-in-` Accessed: 2025-07-22.

[37] Jialiang Sun, Qiang Tian, Haiyan Hu, and Niels L. Pedersen. Axially variable-length solid element of absolute nodal coordinate formulation. *Acta Mechanica Sinica*, 35: 653–663, 2019. doi: 10.1007/s10409-018-0823-7.

[38] Qiang Tian, Mohammad Youssef Mahfouz, and Haiyan Hu. Axially variable-length mooring system control for floating wind turbines: Manuscript of ams. Technical report, School of Mechanical Engineering, Shanghai Jiao Tong University, 2023. Unpublished manuscript.

[39] Lorenzo Tognarelli. Static equilibrium configurations of mooring systems in floating wind turbines. Technical report, Politecnico di Torino, 2023. Unpublished technical note, internal simulation support document.

[40] Lorenzo Tognarelli. Control notes on mooring-based stabilization for floating platforms, 2024. Student technical notes, DTU and Politecnico di Torino.

[41] Lorenzo Tognarelli. Equilibrium angles and static configuration assessment for slack-/taut mooring conditions, 2024. Internal Working Document, Politecnico di Torino.

[42] Henrik Villadsen. *Control of Floating Wind Turbine Platforms Using Mooring Line Actuation*. Msc thesis, Technical University of Denmark (DTU), 2022. URL `https://orbit.dtu.dk/en/publications/control-of-floating-wind-turbine-platforms-us`

[43] Jonas Westre, Amy Robertson, Yi-Hsiang Yu, Javier Martinez, and Henrik Bredmose. A design-driven approach to system-level validation of floating offshore wind turbine simulation models. *Wind Energy Science*, 9(1595):1–29, 2024. doi: 10.5194/wes-9-1595-2024.

[44] Wikipedia contributors. Damping — wikipedia, the free encyclopedia, 2024. URL `https://en.wikipedia.org/wiki/Damping`. Accessed: 2025-07-22.

[45] WindEurope. 2030 vision for european offshore wind ports. Technical report, WindEurope, June 2023. URL `https://windeurope.org/intelligence-platform/product/2030-vision-for-european-offs` Accessed 2025-06-27.

[46] Yingqi Wu, Chao Li, Wen Zhong Shen, Zhen Gao, and Torgeir Moan. Review on dynamics of offshore floating wind turbines. *Renewable and Sustainable Energy Reviews*, 175:113184, 2023. doi: 10.1016/j.rser.2023.113184.

[47] Kun Xu, Kjell Larsen, Yanlin Shao, Min Zhang, Zhen Gao, and Torgeir Moan. Design and comparative analysis of alternative mooring systems for floating wind turbines in shallow water with emphasis on ultimate limit state design. *Ocean Engineering*, 219:108377, 2021. doi: 10.1016/j.oceaneng.2020.108377.

[48] Takeshi Yamamoto, Naoki Sato, Kei Hattori, Daisuke Satoh, and Yoshio Inoue. Study on design conditions of floating wind turbines considering the characteristics of wind and waves at deployment site. *Marine Structures*, 90:103417, 2024. doi: 10.1016/j.marstruc.2022.103417.

[49] Rui Zhang, Shuang Li, Shan Gao, Zhaoqing Yang, and Zhen Liu. Stabilization of the wind turbine floating platform using mooring actuation. *Applied Ocean Research*, 135:103709, 2023. doi: 10.1016/j.apor.2023.103709.